Dissertation

an der Fakultät für Biologie
der Ludwig-Maximilians-Universität München

The function of individual GABAergic synapses on pyramidal cell dendrites

vorgelegt von

Fiona Elisabeth Müllner

München, 2016

Tag der Abgabe:	23.5.2016
Tag der mündlichen Prüfung:	18.7.2016
Erstprüfer:	Prof. Dr. Tobias Bonhoeffer
Zweitprüfer:	Prof. Dr. Christian Leibold

Fiona Elisabeth Müllner: *The function of individual GABAergic synapses on pyramidal cell dendrites,* Dissertation, München, 2016.

E-MAIL:
fiona.muellner@gmail.com

For my mum

"We always have to start with structure. All the books start with structure. You can't know how an organ works unless you know the structure of what is working. Yes, yes! But pages of anatomy are utterly indigestible unless one can appreciate what part the structure plays in the working of the organ. And to describe in detail what is there is so much easier than to discover what part it plays that the great chapters on minute anatomy — those deserts of detail without a living functional watercourse, only a mirage from unverified speculation — are nearly unreadable."

William Rushton

From: *The pursuit of Nature*, Informal essays on the History of Physiology, Cambridge University Press, 1977

"The brain is the most overrated organ."

Woody Allen in *Manhattan*, 1979

SUMMARY

Synaptic inhibition is a major control mechanism in the nervous system which serves to counterbalance, to spatially restrict and to temporally sharpen neuronal excitation. While the function of somatic inhibitory synapses in modulating firing-patterns and network oscillations is well-studied, the limited accessibility of small dendritic compartments has hampered experimental approaches to study dendritic inhibition. The question how individual GABAergic synapses inhibit dendrites has motivated numerous theoretical studies, which predicted that dendritic inhibition can interfere with synaptic inputs and dendritic Ca^{2+} levels, thereby potentially being able to veto plasticity. In addition, the dense and regular, yet plastic anatomical distribution of inhibitory synapses on dendrites suggests a locally restricted function of individual contacts. Parts of the theoretical predictions have been confirmed by one-photon uncaging or iontophoresis of GABA. However, no experimental data with synaptic resolution had been presented so far. To overcome this limitation, a paradigm was established here which allowed the synapse-specific stimulation of individual GABAergic synapse, while monitoring functional changes in the dendrite in parallel. This goal was achieved by combining paired patch-clamp recordings and two-photon imaging.

In organotypic hippocampal slice cultures, a GABAergic interneuron and a nearby pyramidal cell were patch-clamped. Electrical stimulation of the interneuron allowed precise synaptic stimulation, while the mapping of inhibitory contacts and subsequent Ca^{2+} imaging or, respectively, morphological monitoring was achieved by two-photon imaging. To identify GABAergic interneurons, GAD65-GFP mice were used, in which a subset of mostly dendrite-targeting inhibitory interneurons is labeled. In preparatory experiments, the GABAergic interneurons labeled in GAD65-GFP mice were functionally characterized. Stable long-term paired patch-clamp recordings were established, which allowed synaptic stimulation and monitoring of synaptic strength over several hours.

In order to test whether activation of individual GABAergic synapses can veto synaptic plasticity or modify plasticity rules, a first experimental approach aimed at establishing a plasticity induction protocol which fully preserves GABAergic inhibition. Previously established protocols for induction of spine plasticity were not applicable, since the caged glutamate blocked synaptic inhibition as a side-effect. Miniature IPSC recordings were performed to quantify the level of GABA-blockade induced by different caged-glutamate compounds. Moreover, a spectral analysis was established to control for free-glutamate contaminations in the caged-glutamate solution. Finally, a paradigm for spike-timing dependent plasticity with preserved inhibition was successfully established. However, experimental outcomes of spine plasticity induction were more variable than expected, and spine growth was successfully induced with only $\sim$40% probability. Therefore, the paradigm was not efficient enough to study potentially subtle effects of inhibition exerted by individual synaptic contacts with yet unknown spike-timing requirements.

In a second approach, the more fundamental question was addressed whether individual GABAergic synapses can inhibit dendritic Ca^{2+} levels, which are a prerequisite for Ca^{2+}-dependent processes like synaptic plasticity. Dendritic Ca^{2+} transients were evoked by back-propagating action-potentials, which are a necessary component of spike-timing dependent plasticity. In the vicinity of morphologically identified inhibitory contacts, two-photon Ca^{2+} imaging was performed on pyramidal cell dendrites. By simultaneously activating the inhibitory input in every second trial, inhibition of Ca^{2+} transients could be quantified. The level of Ca^{2+} inhibition varied largely between contacts, but surprisingly could reach up to

70%. Local Ca^{2+} transient amplitude and inhibitory contact area were identified as the two major determinants of dendritic Ca^{2+} inhibition. The relationship between Ca^{2+} inhibition and Ca^{2+} amplitude was highly nonlinear and fully consistent with a basic biophysical model describing the non-linear voltage-dependence of Ca^{2+} inhibition resulting from voltage-gated Ca^{2+} channel thresholds.

Finally, the spatio-temporal precision of inhibition was quantified. Ca^{2+} inhibition acted bi-directionally and sharply declined along the dendrites with $\sim$25 μm length constants, with the exception of small, barely supra-threshold Ca^{2+} transients, for which propagation was blocked at the synapse. However, inhibition was diminished in neighboring branches — even within the radius of the average length-constant — indicating that Ca^{2+} inhibition is additionally branch-specific. To mechanistically interpret the results, a detailed morphologically-realistic CA1 pyramidal cell model was built. The model suggested that length-constants of Ca^{2+} inhibition shorten towards branch-points, providing a mechanism for branch-specificity. Most notably, calcium in dendritic spines was inhibited to the same degree as in the neighboring shafts, and the model suggested that in the presence of additional excitatory synaptic input, shaft inhibition can cause even stronger Ca^{2+} inhibition in spines. Furthermore, Ca^{2+} inhibition was strongly spike-timing dependent with $\sim$2 ms decay time constant. The model suggested that this temporal profile of Ca^{2+} inhibition is a mirror image of inhibitory synaptic current, providing an estimate for synapse kinetics of individual dendritic inhibitory synapses. Together with the known anatomical distribution of inhibitory contacts, the data presented here indicate that the collective inhibitory input to a pyramidal cell dendrite is sufficient to control calcium levels across the entire dendritic arbor with micrometer and millisecond precision.

REFERENCE

The chapters 3.2 and 4.2 on "Inhibition of dendritic calcium transients by individual GABAergic synapses" of the Results and Discussion were adapted with modifications from:

> Müllner et al., 2015:
> Müllner FE, Wierenga CJ, Bonhoeffer T (2015) *Precision of inhibition: Dendritic inhibition by individual GABAergic synapses on hippocampal pyramidal cells is confined in space and time*, Neuron 87:576–89.

For this publication, I designed and conducted the experiments, data analysis and modeling, and I wrote the manuscript with the help of all authors.

The data reported in the section 3.1.3 "Characterization of GABAergic interneurons" of the Results was published in:

> Wierenga et al., 2010:
> Wierenga, C.J., Müllner, F.E., Rinke, I., Keck, T., Stein, V., and Bonhoeffer, T. (2010). *Molecular and electrophysiological characterization of GFP-expressing CA1 interneurons in GAD65-GFP mice*, PLoS One 5, e15915.

For this publication, I performed (together with Dr. Ilka Rinke) patch-clamp recordings from GAD65-GFP positive interneurons, and I designed and conducted the electrophysiological charaterization of these cells.

ACKNOWLEDGEMENTS

First and foremost, I would like to thank my PhD supervisor Tobias Bonhoeffer for his constant support, mentoring, intellectual input and for the freedom and encouragement to develop and follow my own direction of research.

I thank Corette Wierenga (now Utrecht University, Netherlands) for supervision during the first half of my PhD.

I am deeply grateful to Max Sperling for his support with LabView to implement custom-made solutions for image acquisition and uncaging, without which many of my experiments would not have been possible. I would like to cordially thank Frank Voss for making and maintaining my slice cultures, and Volker Staiger for help with countless technical details. A very special thank goes to Claudia Huber, not only for help with solutions and immunohistochemistry, but also for being the friendliest desk-neighbor and most generous lunch-companion I could imagine. Many thanks go to Ursula Weber and Marianne Braun for sample preparation and data acquisition of electron micrographic images.

I would like to thank Axel Borst, Idan Segev, Moritz Helmstaedter and Mark Hübener for fruitful discussions.

I am very grateful to:

Yuchio Yanagawa, Gunma University, Maebashi, Gunma, Japan, for sharing the pmGAD67-lacZ and pmGAD65-lacZ plasmids;

Balázs Rózsa, Institute of Experimental Medicine of the Hungarian Academy of Sciences, Budapest, Hungary, and Femtonics, Budapest, Hungary, for providing DNI-glutamate;

Roberto Etchenique, Universidad de Buenos Aires, Argentina, for providing RuBi-glutamate and extensive support for troubleshooting.

I would like to thank the whole Bonhoeffer department, especially Volker Scheuss and Tobias Rose, for sharing knowledge, for productive discussions and for a great atmosphere. Special thanks go to Markus Knopp for many instructive conversations about optical physics, and to Cvetalina Coneva for sharing scientific problems and ideas. I cordially thank Claudia Marget-Hahn for administrative efforts and for taking care.

I am grateful to all friends and colleagues who made the Max Planck Institute of Neurobiology such a welcoming and inspiring working place.

I am deeply grateful to the Max Planck society and the German National Academic Foundation for financial support, and to the International Max Planck Research School for Molecular and Cellular Life Sciences for travel money.

Last but not least, I thank with all my heart my mum Elisabeth Müllner-Hoffner and my partner Oliver Gorka for emotional and intellectual support during all these years, and for tolerating my overly busy work schedule.

CONTENTS

1 INTRODUCTION

1.1 THE POWER OF INHIBITION — GABAERGIC INHIBITION SUBSERVES VERSATILE FUNCTIONS

One supporting pillar of brain architecture is inhibition, which is mediated by mostly short-, but also long-ranging projections, and for which GABA is the predominant neurotransmitter in the central nervous system. A vast variety of processes in the central nervous system depend on GABAergic inhibition, ranging from the balancing of activity levels, over the initiation of network oscillations, to more specific functional traits like the sharp tuning of individual cells. The malfunction of GABAergic inhibition, resulting in an imbalance between excitation and inhibition, is thought to be the common principle underlying a wide spectrum of social and cognitive disorders (Yizhar et al., 2011; Baroncelli et al., 2011), such as autism (Coghlan et al., 2012) or schizophrenia (Lewis et al., 2005). By controlling the precise spike-timing of principal cells, GABAergic interneurons are a prerequisite of cortical network oscillations (Mann and Paulsen, 2007) and thus play a critical role in preventing or limiting the spread of epileptic discharges (Dichter and Ayala, 1987). Furthermore, inhibition is crucial for the processing of different sensory modalities and even dominates over excitation in response to sensory input (Haider et al., 2013). For example, in the visual cortex, inhibition mediates surround suppression (Adesnik et al., 2012), provides gain control (Atallah et al., 2012; Wilson et al., 2012) and sharpens response selectivity (Lee et al., 2012; Wilson et al., 2012, for review: Isaacson and Scanziani, 2011; Niell, 2015). Also earlier in the visual system at the level of the retina, motion-sensitivity of retinal ganglion cells is generated by the asymmetric organization of inhibition (Yonehara et al., 2011). Similarly, in the auditory system, inhibition contributes to sound-localization (Burger et al., 2011) and to intensity selectivity in the dorsal cochlear nucleus (Zhou et al., 2012), while in the olfactory bulb, inhibition accelerates odor discrimination (Abraham et al., 2010). In addition to its role in sensory processing, inhibition has also been implicated to play a fundamental role in learning and memory. In the hippocampus, GABAergic interneurons have been shown to control spatial learning and memory retrieval (Andrews-Zwilling et al., 2012). Also the extinction of memories or reward-related behavior has been related to alterations in inhibition, both in the amygdala (Trouche et al., 2013) and the medial prefrontal cortex (Sparta et al., 2014). This variety of influences on how we perceive and memorize the world is mediated by inhibition as a common denominator — yet the exact mechanisms of inhibition do vary.

1.2 THE MODES OF INHIBITION — GABAERGIC INHIBITION COMES IN DIFFERENT FLAVORS

While the major source of inhibition in the central nervous system are GABAergic interneurons, the term "GABAergic interneurons" actually refers to a variety of different cells or cell-types with diverse properties and functions. Since the criteria by which groups of GABAergic interneurons have been selected and named have not always been consistent, an interdisciplinary group of scientists (the 'Petilla group') set out to provide a nomenclature for classifying GABAergic interneurons (Ascoli et al., 2008; DeFelipe et al., 2013). Following the Petilla nomenclature, GABAergic interneurons can be described in anatomical, physiological and molecular terms. The vast range of molecular markers used to dissect inhibitory

interneurons covers neuropeptides like Somatostatin (SOM), VIP (vasointestinal peptide), neuropeptide Y (NPY) or Cholecystokinin (CCK), Ca^{2+}-binding proteins like Parvalbumin (PV) or Calretinin (CR), transcription factors, vesicular proteins, membrane-bound proteins and others. Likewise, the anatomical and physiological charateristics are manifold. Given the large diversity of GABAergic interneurons, spanning a continuum of parameter values in many different dimensions, one can actually question the usefulness of a rigid classification attempt (Battaglia et al., 2013). Yet, there is little doubt that different interneurons with different properties also serve different functions. Different anatomically and molecularly defined interneuron types fire at different oscillation phases (Somogyi and Klausberger, 2005), indicating a division of labor between groups of interneurons. Moreover, the use of optogenetics to selectively activate or inactivate molecularly defined groups of interneurons has strongly advanced our understanding what is the differential functional and behavioral role of molecularly defined subgroups of interneurons (see below). However, no agreement has been reached so far on the number and definition of certain interneuron classes. Furthermore, considerable interspecies differences have been found (Freund and Buzsáki, 1996). Therefore, despite their immense effort in providing exact definitions for interneuron categorization, the Petilla-authors "look forward to a dynamic evolution" of the nomenclature (Ascoli et al., 2008).

In addition to morphological, molecular and physiological properties which are thought to correlate with local circuit function, GABAergic interneurons can be also distinguished by their developmental ontogeny (Butt et al., 2005; Wonders and Anderson, 2006). GABAergic interneurons are of clonal origin (Ciceri et al., 2013), and the medial and caudial ganglionic eminence (MGE and CGE) are primary sources of cortical interneurons (Butt et al., 2005; Tricoire et al., 2011). Fate mapping of CGE-derived cortical interneurons revealed that CGE-derived interneurons are mostly VIP-positive or Reelin-positive/SOM-negative and make up 30% of cortical interneurons (Miyoshi et al., 2010). In addition to the place of birth, also the birthdate can be an important predictor of systematic variability in interneuron function, even within a previously well-accepted 'cell-type' like the PV-positive basket cells (Donato et al., 2015).

Beyond cellular properties of the interneurons themselves, inhibition also critically depends on the properties of the GABA-receptors expressed on the postsynaptic membrane (reviewed by Ben-Ari et al., 2007). While $GABA_A$-receptors are ionotropic and conduct chloride and bicarbonate, $GABA_B$-receptors are metabotropic and activate e.g. potassium channels. The subunit composition of the pentameric $GABA_A$-channels further contributes to the functional diversity of inhibition (reviewed by Olsen and Sieghart, 2009).

While the phasic activation of postsynaptic GABA-receptors resulting from synaptic GABA-release mediates inhibitory effects which depend on exact spike-timing, also tonic activation of (mostly extrasynaptic) GABA-receptors by ambient GABA-levels has been shown to have a significant network function (for review see Brickley and Mody, 2012). While both modes of inhibition can co-exist and fulfill different functions (reviewed by Farrant and Nusser, 2005), homeostatic competition between tonic and phasic inhibition guarantees that overall levels of inhibition are balanced (Wu et al., 2013).

Figure 1: The Tug of War (Edgar Hunt, 1876-1955) The tug-of-war metaphor can illustrate the two forces — excitation and inhibition — pulling brain activity into opposite directions, thereby keeping the delicate balance necessary for proper brain function.

Image by Plum leaves via Flickr, August 13, 2013: Edgar Hunt "The Tug of War" 19th Century. Creative Commons license: https://creativecommons.org/licenses/by/2.0/.

1.3 CONTROLLING AND CONTROLLED — INHIBITION KEEPS THE BALANCE

While inhibition acts usually by counteracting excessive excitation (often illustrated by a tug-of-war metaphor, Fig. 1), also an exuberance of inhibition can interfere with physiological function. Commonly, the level of inhibition necessary for proper cortical function is not defined by an absolute value, but relative to the excitation level. During active behavior for example, L1 interneurons in auditory cortex downscale both excitation from pyramidal cells and inhibition from PV-interneurons in L2/3 in a balanced manner (Zhou et al., 2014). Inhibitory circuits are controlled by several neuromodulatory transmitter systems like endocannabinoids (Katona et al., 1999), NPY (Ledri et al., 2011), serotonin (Freund et al., 1990) or acetylcholine (Frazier et al., 1998). In addition, inhibitory interneurons are often regulated in turn by other inhibitory circuits, the activation of which results in a relief from inhibition. This phenomenon called 'disinhibition' is a commonly found regulatory mechanism (Pfeffer et al., 2013, reviewed in Chamberland and Topolnik, 2012) which demonstrates the bidirectional action mode of inhibitory circuits. In particular, disinhibition has been shown to be necessary for fear learning, both in the amygdala (Wolff et al., 2014) and the auditory cortex (Letzkus et al., 2011). In the visual cortex, a disinhibitory microcircuit initiates critical-period plasticity (Kuhlman et al., 2013). In the hippocampus, firing rate and timing of OLM inhibitory interneurons (named after the strata oriens and lacunosum-moleculare in which they occur), a major source of feedback inhibition to CA1 pyramidal cells, are differentially controlled by two inhibitory input streams, local interneuron-specific VIP-positive interneurons and septohippocampal GABAergic projections (Tyan et al., 2014). Furthermore, a disinhibitory microcircuit between VIP-positive and PV-positive interneurons bidirectionally modulates and reversibly shifts levels of structural plasticity, memory consolidation and retrieval in the

hippocampus (Donato et al., 2013). But within this complex network of inhibitory layers, even the most basic layer of complexity — the synaptic inhibition onto principal cells — is not yet fully understood in functional terms.

1.4 PERISOMATIC VERSUS DENDRITIC INHIBITION

From the perspective of a postsynaptic principal cell, it is common to make the morphological distinction between perisomatic and dendritic inhibition, depending on where the synapses are located on the postsynaptic cell (Fig. 2). Some particularly powerful interneurons preferentially target the soma and proximal dendrites (basket-cells, Freund and Katona, 2007) or the axon initial segment (axo-axonic cells, Howard et al., 2005). However, CA1 pyramidal cells receive 92% of their GABAergic inputs at the dendrites (Megías et al., 2001). The distinction between perisomatic and dendritic inhibitory synapses is not only justified by mere anatomical abundance, but highly relevant in terms of physiology, since perisomatic and dendritic inhibitory synapses subserve different functions. While perisomatic inhibition suppresses repetitive somatic spikes, dendritic inhibition suppresses dendritic Ca^{2+} spikes (Miles et al., 1996). Also the timing of postsynaptic spikes is differentially affected by perisomatic or dendrite-targeting interneurons (Tamás et al., 2004), suggesting different roles in the gating of spike-propagation within a network.

The main role of perisomatically targeting inhibitory interneurons has been described to control postsynaptic spike-timing and network oscillations (Cobb et al., 1995; Pouille and Scanziani, 2001). For example, basket cells and axo-axonic cells can synchronize pyramidal cell firing (Cobb et al., 1995). The comparably much stronger (since less filtered) somatic than dendritic compound of feed-forward inhibition reduces the temporal integration window to <2 ms and thereby enforces temporal fidelity in coincidence detection (Pouille and Scanziani, 2001).

Dendritic inhibition, on the other hand, has been described as the primary regulator of input-output-transformations, which is itself regulated by perisomatic inhibition (Lovett-Barron et al., 2012, referring to SOM-positive interneurons in the hippocampus). By suppressing pyramidal cell firing, dendritic SOM-positive interneurons also mediate surround-suppression in the visual cortex (Adesnik et al., 2012). Notably, the complex interplay between different layers of inhibition and disinhibition can cause counterintuitive effects if inhibition is lost: for example, loss of dendrite-targeting neurons (in contrast to an acute inhibition blockade) reduces instead of increases receptive field size in the auditory cortex (Seybold et al., 2012).

Recently, the dissection of inhibitory circuits by optogenetics has further elucidated the functional role of different molecularly defined interneuron-groups in cortical networks (Cardin, 2012; Taniguchi, 2014). In the hippocampus, the silencing of SOM-positive (mostly dendritic) interneurons increases CA1 burst firing, while silencing of PV-positive (perisomatic) interneurons shifts spikes with respect to the theta-rhythm (Royer et al., 2012). In somatosensory cortex, SOM-positive interneurons reduce dendritic excitability during quiet wakefulness (Gentet et al., 2012), while PV-positive interneurons temporally sharpen sensory evoked responses (Cardin et al., 2009). Also for higher-level functions, there is a division of labor between PV- and SOM-interneuron. Fast-spiking and SOM-positive interneurons are differentially active during UP and DOWN states in somatosensory cortex (Fanselow and Connors, 2010). In visual cortex, stimulation of PV-interneurons and SOM-interneurons has complementary effects on sharpening feature selectivity in V1, the details of which seem to depend on stimulus strength and duration (Wilson et al., 2012; Lee et al., 2012; Atallah et al., 2012 and comments in Atallah et al., 2012), emphasizing the interconnectivity

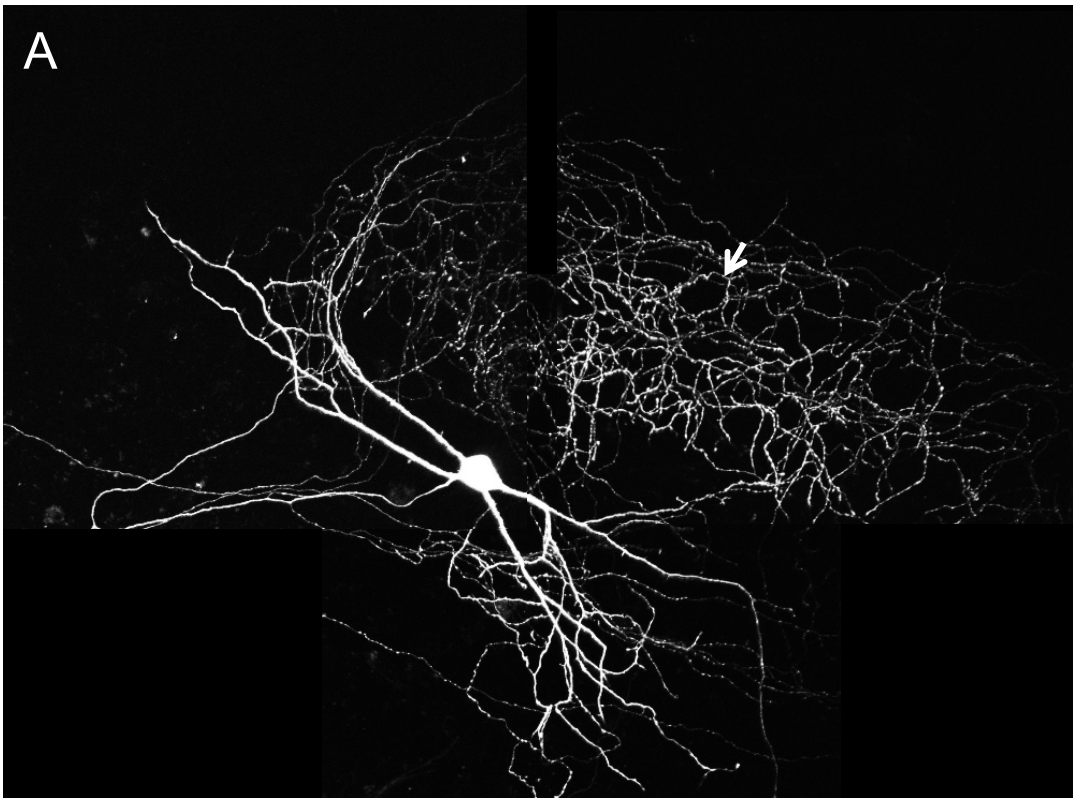

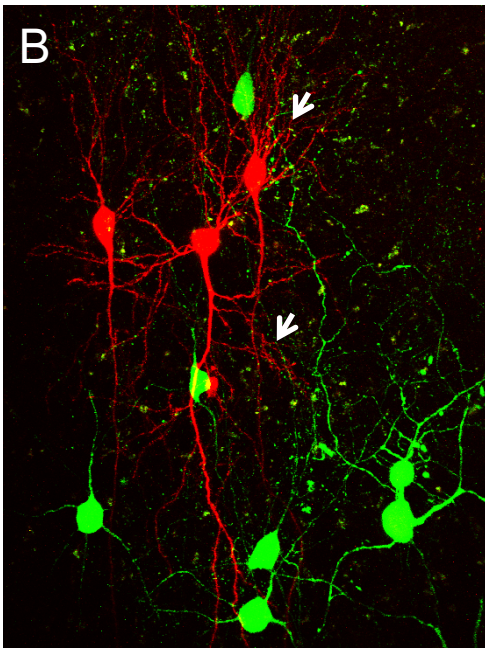

Figure 2: Perisomatic versus dendritic inhibition. (A) The axons of a typical hippocampal basket cell (targeted by GAD67-EGFP) have extensive arborizations in the pyramidal layer, forming little "baskets" of synapses around the somata of pyramidal cells (black holes, arrow). (B) In contrast, axons of dendritically targeting GABAergic interneurons (green, GAD65-GFP positive) mostly spare the somata of pyramidal cells (red, Alexa594-filled) and contact their apical or basal dendrites (arrows).

between the two groups. During behavior, there is a gradual shift of recurrent inhibition from the soma to the dendrites (Pouille and Scanziani, 2004). Similar, but in the opposite direction, early-onset feedforward dendritic inhibition is followed by late onset recurrent somatic inhibition during bursts of sensory input in olfactory cortex (Stokes and Isaacson, 2010). The necessity of dendritic inhibition is additionally highlighted by the fact that the age-dependent loss of inhibition, which is potentially responsible for cognitive impairments,

is in fact a loss of dendritic inhibition by SOM-positive OLM interneurons, while somatic inhibition by PV-positive interneurons is unaltered (Stanley et al., 2012).

1.5 INHIBITORY SYNAPSES IN NUMBERS

For CA1 pyramidal cells, the distribution of inhibitory synapses along the somatodendritic axis has been mapped by electron-microscopy (Megías et al., 2001, in rats). Although inhibitory synapse density varies between cellular compartments, a broad scheme can be derived. The most abundant type of inhibitory synapse is the inhibitory shaft synapse. About 1700 inhibitory synapses are found on CA1 pyramidal cell dendrites, of which 98% are located on dendritic shafts. Given that dendritically targeting interneurons establish about 5-17 terminals (usually on different dendrites, Miles et al., 1996 for CA3 pyramidal cells in guinea pigs), this suggests that pyramidal cell dendrites are contacted by more than 100 inhibitory interneurons. In contrast, 99% of all excitatory synapses are located on dendritic spines, of which the soma and the most proximal apical dendrites are basically devoid (Megías et al., 2001). The rare inhibitory spine synapses and excitatory shaft synapses are found only on stratum lacunosum-moleculare dendrites, where they contribute up to 12% of all inhibitory, respectively 23% of all excitatory synapses in some compartments. The overall density of inhibitory synapses increases from $0.1/\mu$m at the most distal dendrites to $1.7/\mu$m at proximal apical dendrites, with densities of $0.5/\mu$m at intermediate apical/basal dendrites. This latter compartment is of particular relevance in the current study, since it is the compartment in which backpropagating action-potentials readily propagate and which is most sensitive to Hebbian spike-timing dependent plasticity (see review of Feldman, 2012).

1.6 MODELS OF DENDRITIC INHIBITION

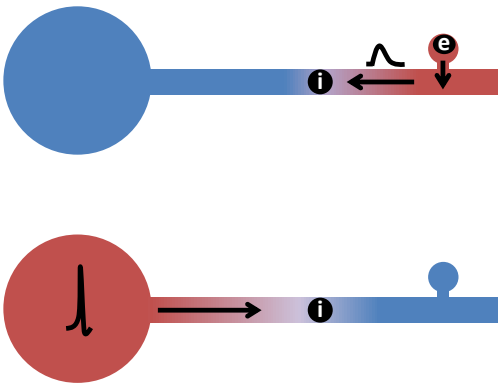

Figure 3: Aspects of dendritic inhibition. Conceivable functions of inhibitory synapses on dendrites (symbolized here by a black spot labeled "i") are: to (1) inhibit the propagation or local amplitude of incoming signals (like EPSPs, upper panel), (2) inhibit the propagation or local amplitude of outgoing signals (like backpropagating action-potentials, lower panel), and (3) locally inhibit synaptic plasticity by a combination of both (1) and (2) and/or by inhibition of Ca^{2+} spikes resulting from massive excitation. The black spot labeled "e" symbolizes an excitatory spine-synapse. Please note that the color gradients are purely illustrative. See Fig. 4 for previous data/simulations on actual Ca^{2+} inhibition profiles.

A large number of theoretical and experimental studies have been inspired by the idea that individual dendritic inhibitory synapses could execute spatially restricted functions (schematized in Fig. 3), as suggested by their mere location. Due to the inaccessibility of small dendritic compartments, many studies relied on compartmental modeling to study the function of dendritic inhibition. Especially the dendritic integration of individual inhibitory and excitatory postsynaptic potentials (IPSPs and EPSPs) is of fundamental interest for understanding neuronal physiology and has therefore been simulated from several different perspectives. Since the 1970s, computational studies have explored how inhibitory synapses should be optimally placed to inhibit EPSPs (Jack et al., 1975; Koch et al., 1983;

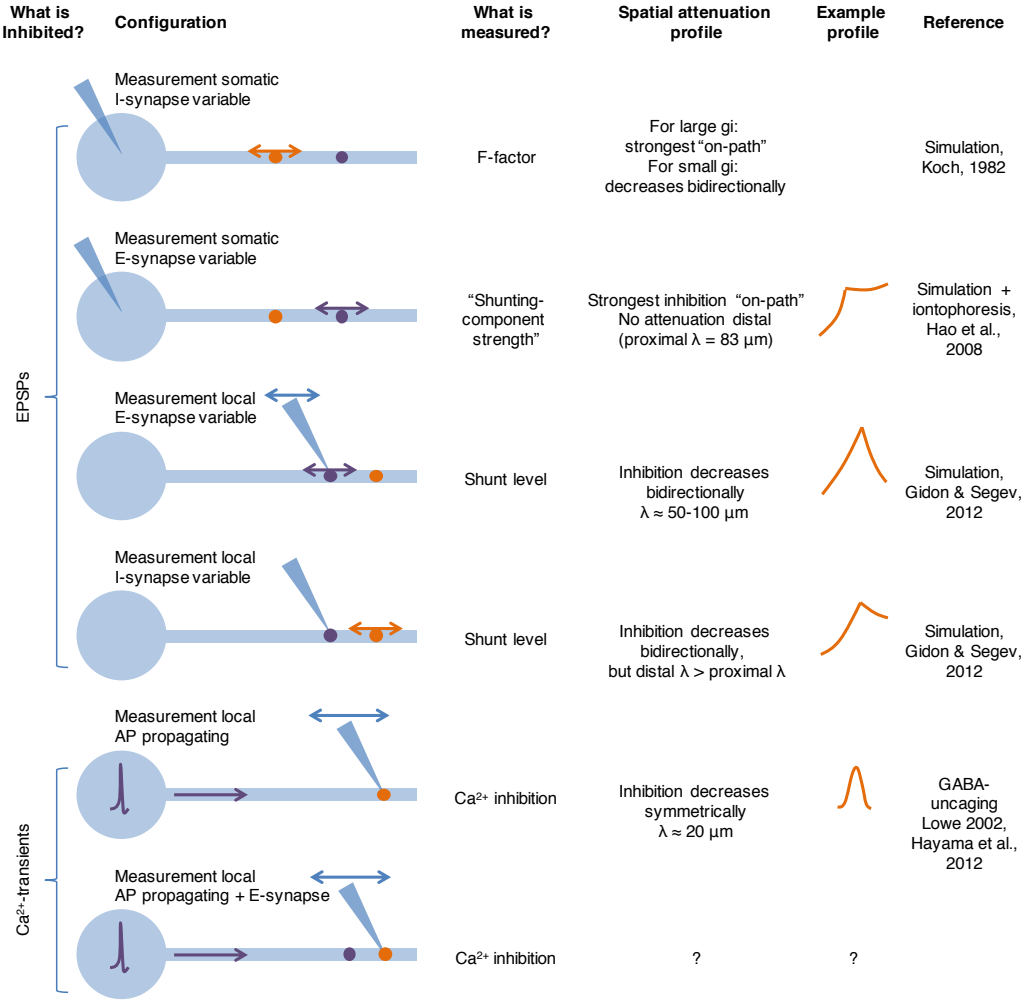

Figure 4: Measurement paradigms to quantify dendritic inhibition by individual GABAergic synapses. The spatial profiles of Ca^{2+} inhibition strongly depend on the experimental configuration. Both hyperpolarization (see Rall and Rinzel, 1973) and inhibitory shunt decrease more shallowly towards the distally sealed end (upper four panels). For inhibition of EPSPs, length constants of 50 μm or more have been measured and predicted. Inhibition of actively propagating signals which evoke Ca^{2+} transients (lower 2 panels) have been studied less intensely. Studies employing GABA-uncaging provided first estimates of 20 μm length-constants in both directions, however, limited spatial and temporal resolution of the stimulation method complicate the interpretation. Furthermore, no mechanistic explanation for such short radius of inhibitory action had been provided so far. For even more complicated configurations in the non-linear regime, like backpropagating action-potentials (APs) paired with EPSPs, no Ca^{2+} inhibition data or simulation quantifying the action radius of an individual inhibitory synapse had so far been published (symbolized by "?"). Not shown are the inhibition of dendritic spikes or synaptic plasticity, see recent data on the inhibtion by multiple (Gidon and Segev, 2012; Bar-Ilan et al., 2012) or single inhibitory synapses in simulation (Jadi et al., 2012) or by GABA-iontophoresis (Müller et al., 2012). Orange circles: inhibitory synapses; purple circles: excitatory synapses. Example profiles are redrawn from the annotated references.

Segev and Parnas, 1983). From studies in passive dendrite models, the 'on-path condition' has been postulated (Koch et al., 1982), which states that inhibition is most effective in dampening a somatically measured EPSP if the inhibitory synapses is placed 'on-path' between the excitatory synapse and the soma. But even in passive dendrites, the interference between EPSPs and IPSPs is considerably more complex than suggested by this catchphrase,

since it depends on inhibitory conductance and exhibits interactions between the space and the time domain (Koch, 1998, chapter 5). While most studies focused on the canonical inhibitory actions of IPSPs which cause a reduction of EPSP amplitude, a few notes can be found that, for specific time-delays, an otherwise inhibitory input could even increase amplitude of an EPSP (Segev and Parnas, 1983). Also counterintuitively, due to the interaction with hyperpolarization-activated cyclic nucleotide-gated channels, inhibition is predicted to bidirectionally regulate pyramidal cell firing, causing a delay or an advancement of pyramidal cell firing depending on the inhibitory spike-timing (Park and Kwag, 2012). If one considers inhibition of supra-threshold events in active dendrites, complexity increases further, and previously derived rules are turned upside down. For example, if one considers supra-threshold dendritic activation by several close-by simultaneously activated excitatory synapses — so-called 'hotspot' excitation — simulations suggest that 'off-path' inhibition by inhibitory synapses placed distally on the same branch as the hotspot would be more effective than 'on-path' inhibition (Gidon and Segev, 2012). In addition, the answer to the question 'where is inhibition most effective' depends critically on what one defines as 'effective', and from which perspective one looks at it (Fig. 4). For example, while off-path inhibition is predicted to be more effective in increasing the local threshold for dendritic spikes, 'on-path' inhibition should be most effective in reducing the spike-height measured at the soma (Jadi et al., 2012).

The intriguing idea that inhibitory synapses on dendrites can interfere with synaptic plasticity of nearby excitatory synapses has also inspired several theoretical studies. Since pharmacological $GABA_A$-receptor blockade had suggested that inhibition can cause a switch from asymmetric to symmetric spike-timing dependent plasticity (STDP) rules (Tsukada et al., 2005; Aihara et al., 2007), modeling studies investigated in detail how $GABA_A$-receptor mediated inhibition can shape dendritic STDP profiles (Cutsuridis, 2011; Cutsuridis and Hasselmo, 2012). With detailed compartmental modeling, predictions have been derived how spatially distributed dendritic inhibition can shape the plasticity of excitatory synapses (Bar-Ilan et al., 2012). This model predicts for example that 'strategically' placed inhibitory synapses could subdivide the dendritic tree in functional compartments with different plasticity regimes, for which the same plasticity induction protocol results in one of three different outcomes: potentiation, depression, or no change for 'protected' compartments (Bar-Ilan et al., 2012).

1.7 SPINE SYNAPSES VERSUS SHAFT SYNAPSES

While 2-30% of all inhibitory synapses can be found on dendritic spines (Megías et al., 2001; Kubota et al., 2007; Beaulieu et al., 1992; Dehay et al., 1991), only 0-15% of spines actually receive inhibitory synapses in addition to excitatory synapses (Megías et al., 2001; Knott et al., 2009; Kubota et al., 2007; Dehay et al., 1991; Jones and Powell, 1969). The exact number of double-innervated spines depends on cortical region, layer, cell-type and preceding experience.

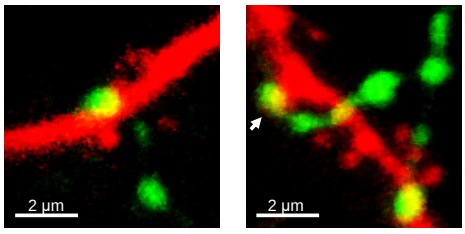

Figure 5: Shaft versus spine contacts. While most inhibitory synapses are located on dendritic shafts (left panel), a minority of synapses is found on dendritic spines (right panel, arrow indicates a putative spine synapse).

Since spines are thought of as separate biochemical and electrical compartments, the uneven distribution of inhibitory synapses has caused some perplexity in the field. It is conceptually hard to imagine why 90% of all excitatory synapses should be fully protected from inhibition, given the modulating and balancing actions of synaptic inhibition on excitatory plasticity. The electrical and biochemical compartmentalization of spines by their neck raises two important questions:

1. Can $GABA_A$-mediated inhibition on spines (Fig. 5) be at all effective, taking into account that chloride accumulates in small compartments? By detailed compartmental modelling applying the Nernst-Planck electrodiffusion model to realistic spine geometries, it has been shown that chloride would accumulate massively in spines upon activation of $GABA_A$-receptors, thereby shifting the $GABA_A$-reversal potential and effectively resulting in synaptic excitation/depolarization instead of inhibition (Qian and Sejnowski, 1989; Qian and Sejnowski, 1990). In conclusion, $GABA_A$-receptor mediated inhibition on spines is predicted to be ineffective, while $GABA_B$-receptor mediated inhibition could be equally effective on spines as on shafts. Nevertheless, a recent study claimed to have measured highly compartmentalized $GABA_A$-receptor mediated inhibition from spine synapses (Chiu et al., 2013), however their compartmental model disregards chloride concentrations and the analysis of their experimental data is biased (see Discussion 4.2.7), casting doubts on their conclusions.

2. Can, on the other hand, shaft synapses effectively inhibit dendritic spines, even if they are electrically separated by the spine neck? The electrical compartmentalization of dendritic spines depends critically on the neck resistance as well as the input resistances of spine head and neighboring shaft. As illustrated in Fig. 6 for passive steady-state signals, attenuation along the spine neck depends additionally on the propagation direction (outward/inward) and the nature of the signal (voltage/current/shunt). For example, voltage signals spreading outwards from the shaft to the spine are not expected to be significantly attenuated, as long as the input resistance of the spine head is much larger than the spine neck resistance. Considerable effort has been made to estimate the distribution of spine neck resistances of pyramidal neurons, yet estimates of average spine neck resistance vary largely between 50 $M\Omega$ (Tønnesen et al., 2014) and 500 $M\Omega$ (Harnett et al., 2012). While the level of inward attenuation will depend strongly upon the exact value, only negligible outward attenuation can be expected within this parameter range. This theoretical prediction has also been confirmed by voltage-sensitive dye measurements (Palmer and Stuart, 2009; Popovic et al., 2014, but see first estimates by Araya et al., 2006), showing that subthreshold depolarizations are not substantially attenuated from the shaft to the spine. However, no direct proof has been available that individual inhibitory shaft synapses can inhibit voltage or Ca^{2+} transients in spines. In this thesis and the associated publication (Müllner et al., 2015), experimental evidence is presented that Ca^{2+} transients from backpropagating action-potentials are inhibited by shaft synapses to the same degree in spines and neighboring shafts, showing that, at least for backpropagating action-potentials, shaft synapses can indeed inhibit Ca^{2+} transients in spines. Moreover, a detailed multi-compartmental model is presented which indicates that spine-inhibition by shaft-synapses can be even stronger if an EPSP follows the action-potential.

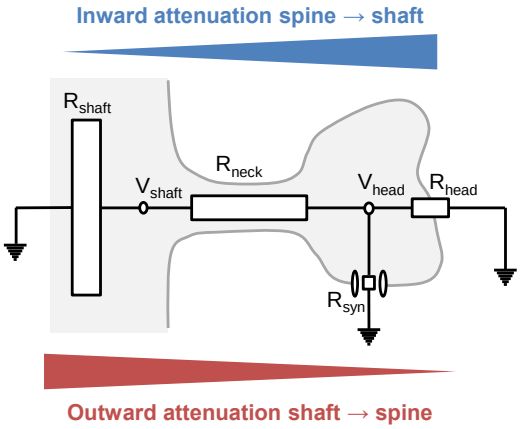

Figure 6: Passive model of spine-neck attenuation. Scheme illustrating the attenuation of signals across the spine neck, assuming a three-compartmental model circuit with spine head resistance R_{head}, neck resistance R_{neck} and shaft resistance R_{shaft}. The table shows the attenuation values of inward or outward propagating signals (voltage/current/shunt-level). Attenuation is defined by the attenuated signal, divided by the original signal, e.g. V_{shaft}/V_{head} for outward voltage attenuation. For passive steady state, assuming capacitive currents across the neck membrane are negligible, the attenuation can be derived from Kirchhoff's circuit laws. The shunt-level is defined as the relative drop in input resistance caused by the opening of an additional conductance. Current attenuation is here the ratio of currents defined as local voltage divided by local input resistance. For a rigorous argument why capacitive currents can be neglected, see e.g. Harnett et al., 2012, their Supplemental Material.

Outward attenuation of:	Formula	Inward attenuation of:
Voltage	$R_{head} / (R_{neck} + R_{head})$	Current
Current	$R_{shaft} / (R_{neck} + R_{shaft})$	Voltage
Shunt-level	$R_{head} / (R_{neck} + R_{head}) \cdot R_{shaft} / (R_{neck} + R_{shaft})$	Shunt-level

Realistic marginal cases:

$R_{head} / (R_{neck} + R_{head}) \approx 1$ if $R_{head} \gg R_{neck}$ (for most realistic neck geometries)

$R_{shaft} / (R_{neck} + R_{shaft}) \ll 1$ if $R_{neck} \gg R_{shaft}$ (for thin/long necks at proximal dendrites)

1.8 THE UPS AND DOWNS OF SYNAPTIC TRANSMISSION — EPSP-IPSP INTERACTIONS

While the interaction of EPSPs and IPSPs in a passive, spherical model cell can be simply described by linear subtraction (and division for larger conductances), the mathematical description of EPSP-IPSP interactions in a three-dimensional, branched dendritic tree is more complex, especially if additional voltage-dependent conductances are opened or closed. An early attempt to understand EPSP-IPSP interactions in vivo was undertaken in cat visual cortex (Ferster and Jagadeesh, 1992). Under the assumption that hyperpolarizing IPSPs interact linearly, while shunting has a non-linear effect, Ferster et al. concluded that the predominant mechanism of IPSPs is based on hyperpolarization, lacking evidence for a shunting component. However, their conclusion was indirect and depended on several strong assumptions. With the advance of fast and spatially selective application techniques, studying interactions between EPSPs and IPSPs became more feasible. By combined glutamate- and GABA-iontophoresis, the spatial summation of dendritic EPSP- and IPSP-like potentials

could be measured, and it confirmed the famous 'on-path' hypothesis for the (indeed significant) shunting component of inhibition (Hao et al., 2009). It should be noted, however, that where the synapse is optimally placed 'on-path' and how symmetric the spatial profile of inhibition is, strongly depends on the conductance strength (Koch, 1998, chapter 5) and the measurement perspective, whether one optimizes the inhibitory synapse location with respect to a fixed excitatory synapse, or vice versa (see Fig. 4).

For small inhibitory conductances, inhibition is maximal if inhibitory and excitatory synapses are co-located, and if one varies the location of the inhibitory synapse with respect to the excitatory synapse, the spatial profile of inhibition decreases bidirectionally (Fig. 4, first panel, Koch et al., 1982; Hao et al., 2009; also see Liu, 2004, but ambiguous axis labeling and missing N limit interpretability here). For fixed inhibition and varying excitatory synapse locations, however, the spatiotemporal profile becomes highly asymmetric (Fig. 4, second panel, Hao et al., 2009). The same is true if one looks at the passive shunt-level introduced by an inhibitory conductance, which decreases fairly symmetrically for inhibition with fixed location (inhibitory-synapse-centric view, Fig. 4, third panel), but very asymmetrically if the location of inhibition is varying (excitatory-synapse-centric view, Fig. 4, fourth panel, Gidon and Segev, 2012). This example illustrates nicely how important it is to exactly define the point-of-view as well as the measurement paradigm when comparing the spatial extent of inhibition along the dendritic axis.

1.9 TUNING THE BACKFLOW OF INFORMATION — INHIBITION OF BACKPROPAGATING APS

In addition to EPSPs, inhibition can in principle interfere with any membrane-potential dependent dendritic event, like for example backpropagating action-potentials. Backpropagating action-potentials are a prerequisite for STDP by delivering information about output activity to the sites of synaptic input (for review: Waters et al., 2005). They can themselves provide a transient increase in dendritic Ca^{2+} concentration by activation of local voltage-gated Ca^{2+} channels (VGCCs, Markram et al., 2004; Christie et al., 1995) or lower the threshold for dendritic spike generation upon coordinated excitatory input (Larkum et al., 1999). Studies on the interaction between dendritic IPSPs and backpropagating action-potentials have focused on dendritic Ca^{2+} level as a readout, which is only an indirect indicator for changes in local membrane potential, but supposed to be the common effector for different forms of synaptic plasticity (reviewed by Sjöström and Nelson, 2002).

Dendritic Ca^{2+} transients induced by backpropagating action-potentials are modulated by coincident IPSPs, as shown by multisynaptic interneuron stimulation (Tsubokawa and Ross, 1996). Local GABA application (Xiong and Chen, 2002) and one-photon uncaging (Lowe, 2002; Kanemoto et al., 2011; Chalifoux and Carter, 2011) suggested that backpropagating action-potentials can be blocked or modulated in amplitude by GABAergic inhibition, and that, in the latter case, inhibition is confined within about ± 15 μm at half-maximum (Lowe, 2002; Kanemoto et al., 2011; Hayama et al., 2013, see fifth panel in Fig. 4). While providing presumably an upper bound for the strength of GABAergic inhibition of backpropagating action-potentials, these studies lacked synaptic specificity and potentially misestimated the length constant due to their limited spatial and temporal resolution of the GABA application techniques. While the limited spatial resolution could lead to an overestimation of length-constants, the limited temporal resolution could cause additional unexpected artifacts due to interactions between the space and time domain. Furthermore, physiological transmitter concentrations at individual synapses are not known and can hence not be mimicked.

1.10 INHIBITION OF DENDRITIC CALCIUM TRANSIENTS AT DIFFERENT SCALES

Dendritic inhibition is thought to act as an arithmetic (subtractive/divisive) operator for linear dendritic computations, or as a boolean (AND-NOT) operator in case of non-linear all-or-none dendritic processes (Ferster and Jagadeesh, 1992; London and Häusser, 2005). The blockade of non-linear dendritic Ca^{2+} spikes can indeed execute elementary computational functions. In retinal ganglion cells for example, the inhibition of dendritic spikes underlies the computation of direction selectivity by blocking the null-direction responses (Sivyer and Williams, 2013). Also more graded changes in dendritic Ca^{2+} levels can be expected to have profound implications for dendritic processes. In the case of synaptic plasticity, a small change in calcium is predicted to determine the occurrence of plasticity (Nevian and Sakmann, 2006) and might even alter the sign of plasticity (Shouval et al., 2002).

Interference of GABAergic inhibition with dendritic activity and dendritic Ca^{2+} levels has been described elaborately on the cellular and microcircuit level, and to a smaller degree also on the subcellular level (for review see Palmer and Stuart, 2009). Both tonic inhibition mediated by $GABA_B$-receptors and phasic inhibiton mediated by $GABA_A$-receptors have been shown to control dendritic Ca^{2+} signaling. Activation of $GABA_B$-receptors abolishes dendritic Ca^{2+} electrogenesis and blocks burst firing (Pérez-Garci et al., 2006; Breton and Stuart, 2012) by modulating L-type currents through Cav1 channels (Pérez-Garci et al., 2013), or directly interferes with NMDA-receptor mediated Ca^{2+} signals (Chalifoux and Carter, 2010), the major determinant of STDP. These actions of $GABA_B$-receptor activation are transient and also spatially selective (on comparably broad scales of hundreds of milliseconds and micrometers). For example, activation of $GABA_B$-receptors reduces the opening probability of VGCCs in apical spines, but not in basal spines or shafts (Sabatini and Svoboda, 2000).

For phasic $GABA_A$-receptor mediated transmission on the other hand — the supposedly more important postsynaptic component in terms of STDP regulation (Nishiyama et al., 2010) — inhibition of dendritic Ca^{2+} spikes has been described upon activation of single (Larkum et al., 1999) or multiple (Miles et al., 1996; Kim et al., 1995) dendrite-targeting inhibitory interneurons in brain slices, as well as in vivo (Murayama et al., 2009). Yet, the corresponding number and distribution of synaptic contacts were unknown in these cases. On the subcellular scale, GABA-iontophoresis has been employed to study the interference of dendritic inhibition with dendritic spikes (Jadi et al., 2012; Müller et al., 2012). Notably, the strength of inhibition can depend on the spike amplitude: recurrent inhibition blocks weak dendritic spikes, while leaving strong dendritic spikes intact (Müller et al., 2012). In their case, dendritic spikes were evoked by strong excitatory inputs, and several different mechanisms, like branch-specific GABAergic efficacy or expression of A-type potassium-channels, potentially contribute to the phenomenon (Müller et al., 2012). Here, I will describe that inhibition of backpropagating action-potential evoked Ca^{2+} transients also depends non-linearly on the local Ca^{2+} amplitude, and that this can be fully explained by a simple biophysical mechanism which is based on the voltage-threshold of VGCC activation.

1.11 CALCIUM MATTERS — SPIKE TIMING DEPENDENT PLASTICITY AT THE SPINE

Synaptic plasticity often follows the much-quoted rule postulated by Donald Hebb that the synaptic connection between two neurons is strengthened if the presynaptic cell "repeatedly or persistently takes part in firing" of the postsynaptic cell (Hebb, 1949), i.e. if the presynaptic cell fires an action-potential shortly preceding an action-potential in the postsynaptic cell.

Many of these synapses also follow the more generalized framework of STDP (for review see Caporale and Dan, 2008; Feldman, 2012), in which synaptic strength is weakened if the temporal correlation between pre- and postsynaptic spikes is reversed, and which can therefore be considered a form of 'asymmetric Hebbian' plasticity. STDP has been described for numerous types of synapses in many different systems, although the exact timing rules for potentiation or depression can vary. The common mechanism of (both positive and negative) STDP is Ca^{2+} influx through synaptic NMDA-receptors or VGCCs. Depending on the amplitude and kinetics of the Ca^{2+} transient, synaptic potentiation, respectively synaptic depression is induced (Cummings et al., 1996; Shouval et al., 2002). For classical Hebbian STDP, the postsynaptic spike is considered to relieve the magnesium block from NMDA-receptors, thereby allowing Ca^{2+} influx through NMDA-receptors, which are in turn activated by presynaptic glutamate release.

Traditionally, functional and structural STDP can be induced by presynaptic theta-burst stimulation, combined with postsynaptic spikes at a well-defined delay (Yang et al., 2008). In order to study STDP at the level of individual synapses, glutamate-uncaging paradigms have been established, in which presynaptic glutamate release is locally mimicked by photolysis of a shielding compound ("cage") bound to the glutamate, and either combined with postsynaptic spiking (Tanaka et al., 2008), or, more simplisticly, conducted under zero-magnesium conditions to unblock NMDA-receptors (Matsuzaki et al., 2004). In a purely optical induction paradigm for plasticity, glutamate-uncaging is combined with optogenetic activation of the channelrhodopsin-expressing postsynaptic cell (Zhang and Oertner, 2007).

A common experimental readout for successful plasticity induction is the specific growth of the activated spike (Matsuzaki et al., 2004, for review: Colgan and Yasuda, 2014). In addition to the enlargement of pre-existing spines, glutamate-uncaging can also induce de-novo spine growth (Kwon and Sabatini, 2011) which is coupled to formation and maturation of glutamatergic synapses on the new spine (Zito et al., 2009). Plasticity induction rules are thought to depend mainly on postsynaptic Ca^{2+} levels. However, it is still a matter of debate whether synaptic plasticity is bidirectional, with the Ca^{2+} level determining whether potentiation or depression is induced, or whether potentiation and depression can be induced independent of each other (Nevian and Sakmann, 2006). Localized Ca^{2+} modulations at the level of dendritic branches are thought to be the basis for branch-specific plasticity, and support the notion of the dendritic branch as a fundamental information processing unit (Harvey and Svoboda, 2007). Along these lines it is interesting to note that dendritic feed-forward inhibition restricts depolarization to selected branches (Willadt et al., 2013), and that dendritic inhibition by individual interneurons is itself branch-specific (Stokes et al., 2014). Moreover, requirements for synaptic plasticity are cell-specific (Blackman et al., 2013) and, even along the somatodendritic axis of a single neuron, dependent on the exact location (Froemke et al., 2005). Since traditional STDP requires postsynaptic spikes, it is only expected to occur in relatively proximal dendritic regions which are fully reached by backpropagating action-potentials. Indeed, distal dendritic synapses require additional dendritic depolarization to exhibit Hebbian STDP (see review of Feldman, 2012).

1.12 DENDRITIC INHIBITION — A FINE-TUNER OF SYNAPTIC PLASTICITY?

Interactions between brain plasticity and inhibitory networks have been described on many different levels. The enhanced plasticity found during critical periods is mediated by changes in PV-interneuron network (for review see Hensch, 2005; Levelt and Hübener, 2012). Also during adult plasticity, a reduction in inhibitory drive creates a permissive environment

for structural plasticity as shown by visual deprivation paradigms (Chen et al., 2011; van Versendaal et al., 2012). On the structural level, inhibitory synapse formation and elimination are locally coordinated with excitatory synaptic changes (Chen et al., 2012), potentially providing permissive 'hotspots' for excitatory synaptic plasticity. The loss of inhibition is itself regulated by another inhibitory control stage, consisting of a disinhibitory microcircuit which can initiate critical-period plasticity (Kuhlman et al., 2013). Also for hippocampus-dependent learning, GABAergic control of synaptic plasticity has been described. Similarly as in visual cortex, inhibitory control in the hippocampus is itself regulated by inhibition: a VIP-interneuron microcircuit inhibiting PV-interneurons bidirectionally modulates and reversibly shifts levels of structural plasticity, memory consolidation and retrieval (Donato et al., 2013). This suggests that disinhibition acts as a common underlying principle for the regulation of plasticity events.

Even before in vivo evidence for the inhibitory regulation of synaptic plasticity had accumulated, such inhibitory regulation had been predicted (Buzsáki et al., 1996; Paulsen and Moser, 1998) and measured in vitro. Suppression of inhibition, e.g. by pharmacological $GABA_A$-receptor blockade, facilitates LTP induction (Wigström and Gustafsson, 1983; Meredith et al., 2003) and diminishes spike-timing dependent LTD (Tsukada et al., 2005; Nishiyama et al., 2010). These studies showed that $GABA_A$-receptor mediated (and also to some extent $GABA_B$-receptor mediated) dendritic inhibition can modulate spike-timing dependent plasticity rules — and can sometimes even reverse the polarity of STDP (Paille et al., 2013).

The control of synaptic plasticity is not limited to excitatory synapses, since postsynaptic $GABA_B$ activation also mediates frequency-dependent potentiation of GABAergic synapses (Xu et al., 2008). The interaction between GABAergic inhibition and synaptic plasticity underlies itself nicotinic modulatory control. By activating $GABA_A$-receptor mediated inhibition, nicotine can increase the threshold for STDP (Couey et al., 2007). This control can be bidirectional: nicotinic activity at pyramidal neurons boosts LTP induction, whereas at interneurons, nicotinic activity diminished LTP induction via inhibition. Therefore, the action of nicotine depends on location and timing (Ji et al., 2001), emphasizing that the same principle mechanism can, as we have seen for GABAergic inhibition, be applied for bidirectional control.

On the synaptic level, a recent study employing combined GABA- and glutamate-uncaging showed that GABA-signaling is necessary and sufficient for an LTD paradigm of spine plasticity and promotes the competitive selection of spines (Hayama et al., 2013). This fortifies the hypothesis that dendritic inhibitory synapses can locally control, and potentially even veto, plasticity at nearby excitatory synapses. The relatively sparse distribution of inhibitory synapses found on spines (only 0-15% of spines have been found to be coinnervated by inhibitory synapses), together with the prediction that $GABA_A$-receptor mediated inhibition on spines will be ineffective due to chloride accumulation (Qian and Sejnowski, 1989; Qian and Sejnowski, 1990), suggest that such a local inhibitory control of synaptic plasticity should be mediated by the more abundant inhibitory shaft synapses. In this PhD thesis and the associated publication (Müllner et al., 2015), I present first experimental evidence that individual dendritic shaft synapses can indeed locally control dendritic Ca^{2+} levels, providing a potential mechanism for the local control of calcium-dependent processes like synaptic plasticity.

1.13 THE MECHANISMS OF INHIBITION — SHUNT OR HYPERPOLARIZATION?

Opening chloride-conducting $GABA_A$-receptors has two interdependent biophysical effects on the cell-membrane: (1) the $GABA_A$-receptor conductance is added to the resting conductance of the membrane (resulting in a shunt of membrane currents), and (2) the membrane is hyperpolarized towards a new equilibrium potential, defined by the reversal potential of $GABA_A$-receptors and their relative conductance. The two components of synaptic inhibition — shunt and hyperpolarization — can be easily exemplified by the steady-state, passive membrane potential response to an inhibitory conductance: $\Delta V = g_i \cdot E_i / (g_i + g_{leak})$. The change in membrane potential ΔV equals the inhibitory current, i.e. the inhibitory conductance g_i times the inhibitory driving force E_i, divided by the summed inhibitory and leak conductances $(g_i + g_{leak})$. If the reversal potential is below rest ($E_i < 0$), ΔV will be negative, resulting in a hyperpolarization. If the reversal potential is at rest ($E_i = 0$), no change in membrane potential is induced and the synapse is called "silent". But even then, the inhibitory conductance g_i acts as a shunt on the membrane, and any additional excitatory conductance g_e with positive driving force $E_e > 0$ will result in a relatively smaller depolarization $\Delta V = g_e \cdot E_e / (g_i + g_e + g_{leak})$ than $\Delta V = g_e \cdot E_e / (g_e + g_{leak})$ if g_i is zero.

The shunt is often quantified as the shunt level $g_i / (g_i + g_{leak})$, which is the relative drop in input resistance caused by the inhibitory conductance g_i. These two components of inhibition — shunt level and hyperpolarization — are not independent of each other, since both the amount of hyperpolarization ΔV and the shunt level depend on the inhibitory conductance.

In a passive model, the hyperpolarization has a subtractive effect, and the shunting component has a divisive effect on any concurrent depolarization. However, the terms subtractive/divisive inhibition are traditionally used in terms of input-output relations (i.e. the relationship between injected current and resulting depolarization or firing rate). By definition, subtractive inhibition shifts the input-output relationship of neurons, while divisive inhibition changes its slope. In terms of firing rates, shunting does not necessarily act divisively and hyperpolarizing not necessarily subtractively. For example, it has been shown that shunting inhibition can have a divisive effect on sub-threshold depolarizations, but a subtractive effect on firing rates (Holt and Koch, 1997).

The underlying biophysical mechanisms how inhibition interferes with non-linear processes are not well-studied. In particular, it was previously not known which biophysical mechanisms would describe or predict inhibition and its spatial profile in highly non-linear regimes. Here, I present first experimental data to address this question, and I show that (graded) dendritic Ca^{2+} inhibition works in a regime in which hyperpolarization and shunt-level are no longer sufficient to fully describe the mechanism and spatial profile of inhibition.

1.14 OPEN QUESTIONS

The intriguing possibility that individual GABAergic synapses could modify or even veto synaptic plasticity at nearby spines had, when this study was initiated, not been addressed experimentally. And equally importantly, inhibition of dendritic Ca^{2+} transients, which are a prerequisite for synaptic plasticity, had not been studied with synaptic resolution. Neither the amplitude nor the spatiotemporal profile of inhibition exerted by individual GABAergic synapses in such non-linear regimes had been simulated or measured before. Studies employing GABA-iontophoresis or one-photon GABA-uncaging could not reach synaptic resolution: due to the high abundance of extrasynaptic GABA-receptors, these methods

do not only co-activate nearby inhibitory synapses, but also stimulate extrasynaptic receptors. In consequence, it was not known how strongly individual GABAergic synapses inhibit local dendritic Ca^{2+} transients and how spatially and temporal precise the effect would be. While branch-specificity of Ca^{2+} inhibition has been recently demonstrated on a rough subcellular scale by multicellular and single-cell stimulation (Marlin and Carter, 2014; Stokes et al., 2014), it remained an open question whether branch-specificity is a mere side-effect of spatial selectivity — simply reflecting the limited action radius of individual inhibitory synapses which are, per se, branch-specifically located — or whether the spread of inhibition, on top of its finite length-constant, is additionally limited by branch-points. Furthermore, the question whether, and to which extent, signals in dendritic spines can be inhibited by individual shaft-synapses had not been experimentally addressed previously. And finally, mechanistic explanations and a realistic model for studying dendritic Ca^{2+} inhibition at the level of individual synapses had been missing.

In this thesis, I now used paired patch-clamp recordings and Ca^{2+} imaging to show that individual inhibitory synaptic inputs moderately but significantly reduce dendritic Ca^{2+} transients, that this inhibitory action is spatially and temporally precise in the micrometer and millisecond range, with an additional branch-specificity which is not a simple side-effect of the overall length-constant, and that Ca^{2+} inhibition is equally strong in dendritic shafts and spines. Finally, I present a realistic model for dendritic Ca^{2+} inhibition which provides mechanistic explanations for these experimental findings.

1.15 AIM OF THE STUDY

Given the large gap of experimental knowledge about the action of individual inhibitory inputs on dendrites, this study aimed at unraveling the function of individual GABAergic synaptic contacts on pyramidal cell dendrites in the hippocampus. The first aim was to establish a paradigm for quantifying the function of individual GABAergic synaptic contacts. This required (1) the synapse-specific stimulation of dendritic GABAergic inputs, (2) the identification of individual inhibitory contacts, and (3) the quantification of inhibitory function.

A first approach aimed at using spine plasticity as a functional readout, and to test whether dendritic inhibition can veto or modify synaptic plasticity. This approach required establishing a protocol for spine plasticity induction under near-physiological conditions with intact GABAergic inhibition. Plasticity induction under these conditions was limited by chemical stability, uncaging efficiency, and pharmacological blockade of GABAergic inhibition by the cage. Moreover, the successfully established plasticity induction protocol showed that — under these near-physiological conditions — plasticity outcomes were more variable than expected, indicating the necessity of a multidimensional readout and limiting the usability of this paradigm for the current study.

In a second approach, dendritic calcium was used as a functional readout to answer the plasticity-related, yet more fundamental question, how individual GABAergic inputs influence dendritic Ca^{2+} levels. This required (1) establishing a protocol to obtain reliable and unbiased measurements of dendritic Ca^{2+} inhibition, and (2) determining the parameters which dictate the strength of Ca^{2+} inhibition. The final aim of this study was to quantify the spatio-temporal precision of dendritic inhibition by individual GABAergic contacts, and to address the question whether inhibition also reaches dendritic spines, the sites where excitatory synapses reside and synaptic plasticity takes place.

Finally, this study aimed at a better mechanistic understanding of dendritic inhibition. To this end, a realistic biophysical model was developed, which also allowed the derivation of relevant predictions concerning plasticity-related questions which go beyond the scope of the present experimental paradigm.

2 MATERIAL & METHODS

2.1 ABBREVIATIONS

3D	Three-dimensional
AB	Antibody
ACSF	Artificial cerebrospinal fluid
AMPA	α-amino-3-hydroxy-5-methyl-4-isoxazolepropionic acid
AP	Action-potential
ATP	Adenosine triphosphate
BDNF	Brain-derived neurotrophic factor
BME	Basal medium eagle
CA1, CA2, CA3	Cornu ammonis, region 1, 2, or 3
CGE	Caudal ganglionic eminence
CV	Coefficient of variation
DIV	Days in vitro after preparation (day of preparation = DIV 0)
EM	Electron microscopy
EPSC	Excitatory postsynaptic current
EPSP	Excitatory postsynaptic potential
GABA	Gamma aminobutyric acid
$GABA_A$-receptor	GABA-receptor, type A
$GABA_B$-receptor	GABA-receptor, type B
GAD65/67	Glutamate decarboxylase, 65 kDa/ 67 kDa isoform
GFP	Green fluorescent protein
GTP	Guanosine triphosphate
HBSS	Hank's balanced salt solution
HEPES	4-(2-Hydroxyethyl)-1-piperazineethanesulfonic acid
IN	Inhibitory interneuron
IPSC	Inhibitory postsynaptic current
IPSP	Inhibitory postsynaptic potential
LTD	Long-term depression
LTP	Long-term potentiation
MGE	Medial ganglionic eminence
mIPSC	Miniature inhibitory postsynaptic currents
NA	Numerical aperture
NMDA	N-Methyl-D-aspartic acid
n.s.	Not significant
OGB1	Oregon Green BAPTA-1
p4	postnatal day 4 (day of of birth = p1)
PBS	Phosphate buffered saline
PCR	Polymerase chain reaction
PV	Parvalbumin
SD	Standard deviation
SEM	Standard error of the mean
SNR	Signal-to-noise ratio
SOM	Somatostatin
STDP	Spike-timing dependent plasticity

Trolox	6-hydroxy-2,5,7,8-tetramethylchroman-2-carboxylic acid
TTX	Tetrodotoxin
2PLSM	2-Photon laser scanning microscopy
v/v	Volume per volume
VIP	Vasoactive intestinal peptide
w/v	Weight per volume

2.2 MATERIAL

2.2.1 Chemicals

Chemicals were obtained from the following distributors:
Acsent Scientific, Cambridge, UK
Alomone labs, Jerusalem, Israel
Bethyl Laboratories Inc., Montgomery, TX, USA
Cytoskeleton, Denver, CO, USA
Invitrogen, Carlsbad, CA, USA
Merck Chemicals, Darmstadt, Germany
Pfaltz & Bauer, Waterbury, CT, USA
Roth Sochiel, Lauterbourg, France
Sigma-Aldrich, St. Louis, MO, USA
Tocris Bioscience, Bristol, UK
VWR ProLaBo, Radnor, PA, USA
Westfalen, Münster, Germany

Chemical	*Distributor*
Actin, human platelet	Cytoskeleton
Adenosine 5'-triphosphate magnesium salt	Sigma-Aldrich
Alexa Fluor 568 hydrazide, sodium salt	Molecular Probes
Alexa Fluor 594 hydrazide, sodium salt	Molecular Probes
Alexa Fluor 488 hydrazide, sodium salt	Molecular Probes
Basal medium eagle (BME)	Invitrogen
Calcein, high purity	Invitrogen
Calcium chloride ($CaCl_2$ * $2H_2O$)	Merck
Cesium methane sulfonate (CH_3CsO_3S)	Sigma-Aldrich
Compressed helium gas	Westfalen
D-AP5	Tocris or Acsent Scientific
DAPI	Sigma-Aldrich
D-(+)-Glucose monohydrate ($C_6H_12O_6$ * H_2O)	Sigma-Aldrich
Disodium phosphate (Na_2HPO_4)	Merck
DNQX disodium salt	Tocris or Ascent Scientific
Ethanol, 100 %	Sigma-Aldrich
EGTA	Sigma-Aldrich
Fluo-5F, Fluo-4, Fluo-4FF, Pentapotassium Salt	Molecular Probes, Invitrogen
Goat serum	Bethyl Laboratories Inc.
Guanosine 5'-triphosphate magnesium salt	Sigma-Aldrich
Guanosine 5'-triphosphate sodium salt hydrate	Sigma-Aldrich
Hank's balanced salt solution (HBSS)	Invitrogen
HEPES	Roth Sochiel or Sigma
Horse Serum, inaktivated	Invitrogen
Hydrochloric acid (HCl, 1 M)	Merck
Kynurenic acid	Sigma-Aldrich

L-glutamine (200 mM)	Invitrogen
L-glutamic acid monosodium salt hydrate	Sigma-Aldrich
Magnesium chloride hexahydrate ($MgCl_2$ * $6H_2O$)	Merck
Magnesium sulfate heptahydrate ($MgSO_4$ * $7H_2O$)	Merck
MEM 1x -Medium	Invitrogen
Methyl potassium sulfate	Pfaltz & Bauer
MNI glutamate	Tocris
Monopotassium phosphate (KH_2PO_4)	Merck
Monosodium phosphate (NaH_2PO_4 * H_2O)	Merck
Paraformaldehyde (PFA; $OH(CH_2O)nH$)	Merck
Phosphocreatine disodium salt hydrate	Sigma-Aldrich
Polyvinylpyrollidone (PVP)	Sigma-Aldrich
Potassium chloride (KCl)	Merck
Potassium D-gluconate	Sigma-Aldrich
Potassium dihydrogen phosphate (KH_2PO_4)	Merck
QX-314 (bromide salt)	Alomone labs
RuBi-Glutamate	Tocris or Ascent Scientific
Sodium chloride (NaCl)	Merck or VWR ProLaBo
Sodium hydrogen carbonate ($NaHCO_3$)	Merck
Sodium hydroxide (NaOH, 1N)	Merck
Sodium Pyruvate ($C_3H_4O_3Na$)	Sigma-Aldrich
Spermidine	Sigma-Aldrich
SR95531	Tocris or Ascent Scientific
Sucrose	Merck
Tetrodotoxin (TTX)	Sigma-Aldrich
Triton X-100	Sigma-Aldrich
Trolox	Sigma-Aldrich
Uridine	Sigma-Aldrich

2.2.2 Consumables

Gold particles: 1.6 μm diameter, Bio-Rad Laboratories, Hercules, CA, USA
Nylon mesh: 90 μm, Small Parts, Miami Lakes, FL, USA
Qiagen Mini and Maxi Prep Kits: Qiagen, Hilden, Germany
Borosilicate glass capillaries: GC 150 F-10 and GC 150-10 (1.5 mm O.D. x 0.86 mm I.D.), Harvard Instruments, Holliston, MA, USA
Durapore PVDF 0.22 μm centrifugal filter units: Millipore, Billerica, MA, USA

2.2.3 Equipment

CCD Camera: KP-M2RP, Hitachi Kokusai Electric Inc., Japan
Digitizer for Electrophysiology: Digidata 1440A, Molecular Devices, Sunnyvale, CA, USA
Headstages: CV-7B, Molecular Devices, Sunnyvale, CA, USA
Hg-Lamp: X-Cite 120PC Q, Excelitas Technologies, Waltham, MA, USA
High-voltage supply for PMTs: custom made, electronics workshop Max Planck Institute for Neurobiology, Martinsried, Germany
Imaging Boards: National Instruments, BNC-2090 and BNC-2090A, Austin, TX, USA
Lasers: MaiTai and Tsunami + Millenia, Spectra-Physics, Santa Clara, CA, USA
Low-noise current preamplifiers: Model SR570, Stanford Research Instruments, Sunnyvale, CA, USA
Manipulators: Junior XL + 2x mini25, SMI, SM-6 + SM-5 (Handwheel), Luigs & Neumann,

Ratingen, Germany
Microscope: Axiovert 35, Zeiss, Oberkochen, Germany
Patch-Clamp amplifier: Multiclamp 700B, Molecular Devices, Sunnyvale, CA, USA
Objective: Olympus UApo/340, 40x/1.15W, Olympus, Tokio, Japan
Oscilloscope: Tektronix TDS 2014, Beaverton, OR, USA
Photodiode: Thorlabs PDA100A-EC, Newton, NJ, USA
Photomultipliers: R6357, Hamamatsu Photonics, Hamamatsu, Japan
Picospritzer: Picospritzer III, Parker, Hollis, NH, USA
Piezo Amplifier: PI E-665.LR, Physik Instrumente, Karlsruhe, Germany
Pipette holders: DB-S-1.5g, G23 instruments, UCL, London, UK
Pipette puller: Micropipette puller P-97, Sutter Instrument Co., Novato, CA, USA
Pockels cells: 302A + 302RM & 350-80 Controller, Conoptics, Danbury, CT, USA
Pump for bath perfusion: Gilson Minipuls 3, Villier, France
Pump for H_2O substitution: Perfusor Secura FT, B. Braun, Melsungen, Deutschland
Scanhead: Yanus-1, TillPhotonics, München, Germany
Shutter controllers: Uniblitz, VCM-D1, Vincent Associated, Rochester, NY, USA
Shutters: Uniblitz VS25S2ZMOR3-NL, Vincent Associates, Rochester, NY, USA
Temperature controller: DB 1000, Chino Works Ltd., Tokio, Japan

2.2.4 DNA

Vectors

pmGAD65-lacZ (Kobayashi et al., 2003) and pmGAD67-lacZ (Makinae et al., 2000) were provided by courtesy of Dr. Yuchio Yanagawa, Japan.
pEGFP-N1 was obtained from Clontech, Mountain View, CA, USA.

Primers

PCR primers were obtained from Metabion (Martinsried, Germany).
pmGAD65-lacZ forward: CAATGAGCCAATCGATGCACACG
pmGAD65-lacZ reverse: GCAAGGCGCTCGAGTTAATTAACGCCAGGGAC GTCCCAGTC (introduces PacI, AatII and PspXI)
pmGAD67-lacZ forward: CTACTGTGCTTGCGCCCCAGTCCCAGAG
pmGAD67-lacZ reverse: CGACGTTGTAAGTCGACGGGATGCATGCGCTCC (substitutes BamHI with SalI and SphI restriction sites)
pEGFP-N1 forward: GGATCCACCGCATGCCACCATG (introduces SphI restriction site)
pEGFP-N1 reverse: CGCTTACAGTCGACGCCTTAAGATACATTG (introduces SalI restriction site)
pEGFP-N1 forward 2: GCTTCGAATTCTGCAGTCGACGTCACC (introduces AatII restriction site)
pEGFP-N1 reverse 2: CGATTTCGGCCTATTGGTTAATTAATGAGC (introduces PacI restriction site)

2.2.5 Enzymes

NheI, SalI, SphI, ClaI, PspXI, AatII, PacI and T4 Ligase were obtained from New England Biolabs (Ipswich, MA, USA), Taq Polymerase was obtained from Fermentas/Thermo Scientific (Waltham, MA, USA).

2.2.6 Antibodies

Antibodies were obtained from:

Dianova, Hamburg, Germany
Invitrogen, Carlsbad, CA, USA
Jackson ImmunoResearch, West Grove, PA, USA
Millipore, Billerica, MA, USA
Research Diagnostics, Flanders, NJ, USA
Synaptic Systems, Göttingen, Germany

Primary Antibodies	*Dilution*	S*upplier*
anti-GABA (rabbit, polyclonal)	1:1000	Sigma (A2052)
anti-GAD67 (mouse, monoclonal)	1:3000	Millipore (MAB5406)
anti-GAD65 (rabbit, polyclonal)	1:500-2000	Millipore (AB5082)
anti-GFP (chicken, polyclonal)	1:1000	Millipore
anti-GFP (rabbit)	1:1000	Research Diagnostics

Secondary antibodies	*Dilution*	*Supplier*
anti-chicken-Alexa 488	1:200	Invitrogen
anti-mouse-cy3	1:200	Dianova
anti-rabbit-Alexa 633	1:200	Invitrogen
anti-rabbit Biotin-SP-conjugated (goat)	1:300	Jackson

2.2.7 Extracellular solutions

Artificial cerebrospinal fluid (ACSF)

NaCl	126 mM
KCl	2.5 mM
$CaCl_2$	2.5 mM
$MgCl_2$	1.3 mM
NaH_2PO_4	1.25 mM
$NaHCO_3$	26 mM
Glucose	20 mM
Trolox	0.2-1 mM
Pyruvate ($C_3H_4O_3$)	0-1 mM

ACSF was saturated with 95% O_2 and 5% CO_2 for experiments. Tenfold stock solutions of phosphate buffer (NaH_2PO_4 + $NaHCO_3$) and ringer solution (NaCl+KCl+$CaCl_2$+$MgCl_2$) were stored at 4 °C, and 1 M stock solution of glucose and 1 M stock solutions of pyruvate were stored at -20 °C until usage.

In early experiments, 1 mM Trolox was used, but the concentration was reduced to 200 μM, adapting to protocols of Tanaka et al., 2008 and Matsuzaki et al., 2004.

In early experiments, 1 mM pyruvate was supplied to the ACSF following standard protocols (Wierenga et al., 2010). Pyruvate is the end product of glycolysis which can either serve to build ATP in the citrate cycle or to build glucose by gluconeogenesis. If there is a deficit in glucose, pyruvate can directly go into the citrate cycle and provide energy. Therefore, pyruvate has a protective effect in case of hypoglycemia or certain forms of ischemia (Klonoff, 2005). However, if enough glucose is provided for glycolysis, excess pyruvate will be metabolized into lactate in an anaerobic process, resulting in a lactic acidosis. If excessive (20 mM) glucose is provided to the slice, addition of 1 mM pyruvate can produce a lactic acidosis,

as suggested by intracellular pH measurements (Yehezkel Ben-Ari, personal communication). Therefore, pyruvate was first reduced to 250 μM, and finally omitted from the ACSF (for all Ca^{2+} imaging data shown in chapter 3. Results).

In a small subset of uncaging experiments, 1 μg/ml BSA was added to prevent potential loss of caged-glutamate by sticking to the perfusion tubing (Tanaka et al., 2008), but no effect was observed.

In uncaging experiments in which small volumes (10-20 ml) of ASCF had to be recycled, spontaneous activity levels increased over time, to a certain degree also if no caged-glutamate was added to the ACSF. Despite immense trouble-shooting effort, no fully conclusive explanation for this phenomenon was found, but several factors, including pH, perfusion speed and pyruvate content, seemed to play a role. A subset of these experiment was therefore performed in ACSF with reduced $NaHCO_3$ (21 instead of 25 mM, NaCl increased to 135 mM), which compensates for the increase in $\sim$0.1 pH by heating the ACSF from 24°C to 34°C (which is due to the lower solubility of CO_2 at higher temperature). Osmolarity was kept constant by H_2O substitution via a pump, the speed of which was calibrated for the respective temperature and perfusion velocity. In the final set of experiments (section 3.2), no pyruvate was supplied and ACSF was not recycled.

HEPES-ACSF

NaCl	135 mM
KCl	2.5 mM
$CaCl_2$	2.5 mM
$MgCl_2$	1.3 mM
NaH_2PO_4	1.25 mM
$NaHCO_3$	2 mM
HEPES	20 mM
Glucose	17-20 mM

Adjusted to pH 7.4 by NaOH. HEPES based ACSF was used for puff-application of caged-glutamate to prevent plugging of the pipette by precipitates due to drifting pH.

Medium for organotypic slice cultures

Gähwiler medium
GBSS (1.5 mM $CaCl_2$, 4.96 mM KCl, 0.22 mM KH_2PO_4, 1.03 mM $MgCl_2$, 0.07 mM $MgSO_4$, 136.89 mM NaCl, 2.7 mM $NaHCO_3$, 0.85 mM Na_2HPO_4, 5.55 mM D-glucose), 1 mM kynurenic acid, 50 mM D-glucose; pH adjusted to 7.2 with 1 M HCl, sterile filtrated.

Müller medium
95,5 ml MEM 1x, 50 ml HBSS, 50 ml Horse serum, 2 ml 5M Glucose, 2,5 ml 1M Hepes; pH adjusted to 7.2 with 1M HCl, sterile filtrated.

In Gähwiler cultures and early preparations of Müller cultures, the antimitotic agents uridine, 5-fluorodeoxyuridine and cytosine P-D-arabinofuranoside were added at equal concentrations (4.3 μM) starting on day 3 or 4 of culture and were removed after 16-24 hours (Caeser et al., 1989).

Phosphate-buffered saline (PBS)

2.7 mM KCl, 1.47 mM KH_2PO_4, 138 mM NaCl, 7.24 mM Na_2HPO_4; pH was adjusted to 7.4 with 10 M NaOH.

2.2.8 Internal solutions

For all internal solutions, the pH was adjusted to 7.2-7.3 by 1M KOH, and osmolarity was adjusted by sucrose to 300-305 mOsm.

K-Gluconate

K-Gluconate	142.5 mM
KCl	7.5 mM
HEPES	10 mM
Na_2-Phosphocreatine	10 mM
NaGTP	0.3 mM
MgATP	4 mM

Part of the glutamate uncaging paradigm were performed with slightly modified K-Gluconate internal: K-Gluconate 145 or 140 mM, KCl 5 mM + NaCl 5 mM or KCl 10 mM, EGTA 0.1 mM, Na_2-Phosphocreatine 0 or 5 mM, NaGTP 0 or 0.3 mM, MgATP 2 mM.

K-Methylsulfate

For interneuron classification in acute slices (section 3.1.3):

$KMeSO_4$	150 mM
KCl	4 mM
NaCl	4 mM
HEPES	10 mM
MgGTP	0.4 mM
MgATP	4 mM

otherwise:

$KMeSO_4$	142.5 mM
KCl	7.5 mM
HEPES	10 mM
Na_2-Phosphocreatine	5 mM
Na_2GTP	0.3 mM
MgATP	4 mM

K-Methylsulfate substituted K-Gluconate in a subset of paired recording experiments, but appeared to make the cell membrane more rigid over time and, in particular, to impede repatching the cells.

Cs-Chloride

CsCl	140 mM
NaCl	4 mM
HEPES	10 mM
EGTA	1 mM
MgATP	2 mM

Cs-Chloride was used for miniature recordings. The tip fill for miniature recordings contained 140 mM KCl instead of CsCl.

2.2.9 Fixative

To fix organotypic slice cultures for post-hoc immunohistochemistry, a solution of 4 % PFA (w/v) in PBS was used, which was freshly prepared from a 16 % (w/v) PFA stock solution stored at -20 °C.

2.3 EXPERIMENTAL PROCEDURES

2.3.1 Organotypic slice culture preparation

All experimental procedures were carried out in compliance with the institutional guidelines of the Max Planck Society and the local government (Regierung von Oberbayern). Hippocampal slices (350 μm thick) were prepared from postnatal day 4-6 GAD65-GFP (Wierenga et al., 2010; López-Bendito et al., 2004) or C57/Bl6 mice and maintained in culture up to 6 weeks following standard protocols (Stoppini et al., 1991, medium glucose reduced to 5.7 mg/ml). In a subset of early experiments (biolistic transfections and miniature analysis), roller-tube cultures were used (Gähwiler, 1981). The entire preparation procedure was carried out under a laminar flow. Briefly, mice pups were decapitated, the brain was removed from the skull and stored in fresh, ice-cold Müller medium (or Gähwiler medium in an early protocol). Hippocampi were removed and cut in 350 μm transversal slices using a tissue chopper. Slices were then stored in preparation medium and separated using fine forceps. To allow for removal of debris and regeneration, slices were stored in preparation medium at 4° C for 30-60 min. Subsequently, slices were transferred to fresh medium, sorted for tissue integrity and oriented to their final position on the membrane. Slices were maintained at 35° C. Medium was changed twice per week. In hippocampal slice cultures, the distribution, development and synaptic properties of GABAergic synapses closely resemble the in vivo situation (De Simoni et al., 2003; Streit et al., 1989).

2.3.2 Cloning of GAD65/67-EGFP vectors

pmGAD65-lacZ (Kobayashi et al., 2003) and pmGAD67-lacZ (Makinae et al., 2000) were provided by courtesy of Dr. Yuchio Yanagawa, Japan. From the pmGAD67-lacZ plasmid, a 318 bp fragment at the 3' end of the GAD67 promoter region was PCR-amplified, which spanned the NheI and BamHI sites and substituted the BamHI by a SphI and SalI restriction site. The PCR product and GAD67-lacZ vector were digested by NheI and SalI, purified and ligated, resulting in a 13122 bp plasmid designated pmGAD67-empty, which lacked the lacZ and SV40 poly(A) sequence. The EGFP and SV40 poly(A) sequences were PCR amplified from pEGFP-N1, creating SphI and SalI restriction sites at the 5' respectively 3' end. The PCR product and pmGAD67-empty were digested by SalI and SphI and ligated, resulting in a 14089 bp plasmid designated pmGAD67-EGFP. From the pmGAD65-lacZ plasmid, a 730 bp fragment at the 3' end of the GAD65 promoter region was PCR-amplified, which spanned the ClaI and BamHI sites and added AatII, PacI and PspXI restriction sites at the 3' end (from 5' to 3'). The PCR product and GAD65-lacZ vector were digested by ClaI and PspXI, purified and ligated, resulting in a 12244 bp plasmid designated pmGAD65-empty, which lacked the lacZ and SV40 poly(A) sequence. The EGFP and SV40 poly(A) sequences were PCR amplified from pEGFP-N1, creating AatII and PacI restriction sites at the 5' respectively 3' end. The PCR product and pmGAD65-empty were digested by AatII and PacI and ligated, resulting in a 13297 bp plasmid designated pmGAD65-EGFP. Kozak consensus sequences were preserved. Cloned plasmids were partial sequenced.

2.3.3 Biolistic transfection

Hippocampal slices cultures were biolistically transfected following the protocol of McAllister, 2000 using the Helios Gene Gun System. 12.5 mg of 1.6 μm gold were mixed with 100 μl spermidine (50 mM in H_2O), vortexed and sonicated. DNA was added (25-50 μg pmGAD65-EGFP or pmGAD67-EGFP) and, after vortexing and sonication, DNA was precipitated to the gold particles by dropwise adding 100 μL of 1 M $CaCl_2$. The solution was incubated for 10 minutes under repeated mixing. The gold particles were centrifuged and washed 3 times with dry 100% ethanol, followed by resuspension in 3 ml PVP solution (0.05 mg/mL PVP in dry 100% ethanol). Afterwards, the gold suspension was filled into a 75 cm long tubing (dried beforehand with nitrogen for 30 minutes) and incubated for 5 minutes. The solution was removed, followed by another 5 minutes of incubation while rotating and drying the tubing with nitrogen at a pressure 0.35 LPM. Lastly, the tubing was cut into 1-2 cm long cartridges which were stored dry at 4°C. Hippocampal slice cultures were transfected at p3-30 div with DNA coated gold particles at a pressure of 120-240 psi (Helium gas) and at a distance of approximately 1-2 cm. A nylon mesh with 100 μm pore size in front of the barrel liner was used to diffuse the gold particles. Transfected slices were then kept in culture for 4-14 days until used for experiments. Transfection efficiency (for pmGAD67-EGFP) decreased from 5 to 2 cells on average for cultures older than p10.

2.3.4 Immunohistochemistry

Slice cultures (Müller-type) were fixed in prewarmed (37°C) 4 % PFA for 30 minutes at room temperature, washed with PBS and kept at 4°C in the dark. For permeabilization of the tissue and blocking of unspecific epitopes, they were incubated with 0.5% v/v Triton X-100 and 10 % v/v goat serum in PBS at 4°C for 2 days. Primary antibodies were applied for 2 hours at room temperature in 0.4 % v/v Triton X-100, 5 % v/v goat serum and PBS. After extensive washing, secondary antibodies were applied for 1 hour at room temperature in 5 % v/v goat serum and PBS. After washing, DAPI was added with 1 ng/ml final concentration and incubated for 10 minutes at room temperature. Subsequently, slices were washed in PBS and embedded. Finally, high-resolution confocal image stacks were taken and analyzed.

2.3.5 A setup for combined 2-photon imaging and 2-photon uncaging

The light beams of two Titanium-Sapphire lasers (MaiTai and Millennia/Tsunami, Spectra-Physics, Santa Clara, CA, USA) — the MaiTai for structural or Ca^{2+} imaging and the Tsunami for glutamate uncaging or structural imaging — were combined by a polarizing beam splitting cube before entering the tube lens and scanner (Yanus I, TillPhotonics, Munich, Germany). The light intensity of each laser was independently controlled by electro-optical modulators (Pockels cells, Conoptics 350-80, Danbury, CT, USA). The laser beam was routed through the scan lens and a dichroic mirror (passing excitation light and reflecting emitted light from the probe) before reaching the probe through a 40x water immersion objective. The optical paths were aligned such that the offset between the two lasers was minimized (remaining offset in z: 0.24 μm with Olympus Uapo 340, 40x/1.15W; 1.4 μm for early experiments with Zeiss C-Apochromat 40x/1.2W, which required manual z-correction between imaging and uncaging). Emitted photons were separated with appropriate dichroics and filters and collected by photomultiplier tubes (R6357, Hamamatsu Photonics, Hamamatsu, Japan). Image acquisition and uncaging were controlled by custom software (Colibri, by Max Sperling, MPI of Neurobiology, Martinsried, Germany) implemented in Labview version 8.6 (National Instruments, Austin, USA).

2.3.6 Glutamate uncaging

Glutamate-uncaging was performed using the following caged glutamates:

MNI-glutamate: 4-methoxy-7-nitroindolinyl-glutamate from Tocris Bioscience, Ellisville, USA
RuBi-glutamate: [Ru(bpy)2(PMe3)($GluH_2$)](PF6)2-glutamate from Tocris Bioscience, Ellisville, USA, or Acsent Scientific, Cambridge, UK, or kindly provided by Prof. Roberto Etchenique, Universidad de Buenos Aires, Argentina
DNI-glutamate: 4-methoxy-5,7-dinitroindolinyl-L-glutamate trifluoroacetate, kindly provided by Balázs Rózsa, Institute of Experimental Medicine of the Hungarian Academy of Sciences, Budapest, Hungary.

Stock solutions of 20-25 mM caged glutamate were prepared in HEPES-ACSF (to prevent precipitation and uncaging at low pH) and kept dark at 4°C. For experiments, stock solutions were diluted in ACSF or (for high concentrations) caged glutamate was directly dissolved in ACSF. Caged glutamate solutions were bath-applied to the slice cultures, since uncaging efficiency during puff-application was too variable in preliminary experiments. Substances were handled in the dark as far as possible, and all remaining sources of stray light were covered with Rosco supergel #27 red filters (Rosco, London, UK), both during preparation of solutions as well as during experiments. Since MNI-glutamate blocked inhibitory synaptic transmission even at concentrations 10-30x lower than concentrations needed for efficient 2-photon uncaging (Fig. 19), plasticity induction experiments were performed with RuBi-glutamate (350-600 μM) or DNI-glutamate (350-2500 μM). RuBi-glutamate regularly contained variable amounts of free glutamate which hampered experiments (see 3.1.9), therefore the last third of experiments was performed with DNI-glutamate. Since the results of plasticity induction were not detectably different between RuBI-glutamate and DNI-glutamate, pooled data is shown in section 3.1.10. A peristaltic pump was used for bath perfusion to minimize total bath volume (10 ml) and re-circulate oxygenated ACSF. An additional pump added H_2O to the resevoir and was calibrated such that osmolarity was kept constant (∼315 mOsm). Uncaging was induced by high-intensity laser pulses (up to 100 mW on sample) of 800 nm (RuBi-glutamate) or 750 nm (DNI-glutamate). The scanning mirrors and Pockels cell were synchronized to increase laser power only at a predefined uncaging spot that was manually selected next to a dendritic spine or shaft. Images of the dendritic shaft and spines were acquired using minimal power at 740 nm (RuBi-glutamate) or 750-780 nm (DNI-glutamate) to prevent uncaging.

2.3.7 Spine plasticity induction

Spine plasticity was induced in pyramidal cells of hippocampal slice cultures (p6-28) by pairing 30-60 pulses of glutamate uncaging on a selected spine with backpropagating action-potentials at 0.5-1 Hz. Backpropagating action-potentials were elicited within 5.1 ± 4.4 ms after uncaging (mean ± SD, 0-16 ms range). Laser intensity (20-120 mW on sample) and pulse duration (0.5-5 ms) were adjusted to evoke EPSCs within a reasonable amplitude range (18.3 ± 13.7 pA, mean ± SD). Pyramidal cells were first held in voltage-clamp at -70 mV to record uncaging evoked EPSCs and to adjust their amplitude (series resistance 12.8 ± 5.5, range 6-35 MΩ). For plasticity induction, action-potentials were elicited in current-clamp by 1 ms current pulses injected at the soma. After induction, evoked EPSCs were again recorded in voltage-clamp at -70 mV for comparison. K-Gluconate internal solution contained 20-200 μM Alexa 568 or Alexa 594 for structural imaging and 0-200 μM Fluo-5F. In a subset of experiments, 5 μM beta-Actin was included in the pipette (see 3.1.10). Z-stacks of the spine and neighboring dendrite (15x15 μm, 300x300 s, 0.5 μm z-steps) were acquired before and after plasticity induction.

2.3.8 Electrophysiology

Whole-cell patch-clamp recordings for Ca^{2+} inhibition experiments were obtained at 34°C in organotypic hippocampal slice cultures from pyramidal cells (mostly CA1) and interneurons with their somata located in stratum radiatum/oriens or adjacent to stratum pyramidale using a Multiclamp 700B amplifier (Molecular Devices), Bessel-filtered at 6kHz (voltage-clamp) or 10 kHz (current-clamp), and digitized at 20 kHz (Digidata 1440A). Borosilicate glass capillaries (1.5/0.86 mm od/id, Harvard apparatus, 3-7 MΩ) were filled with K-Gluconate internal solution including 200 μM Ca^{2+} indicator Fluo-5F and 30 μM Alexa 594 for pyramidal cells, 200 μM Alexa 488 or calcein and 20 mM GABA (Bouhours et al., 2011) for interneurons. Recordings were discarded if pyramidal cells depolarized to >-50 mV or interneurons depolarized to >-43 mV (not corrected for liquid junction-potentials). Hyperpolarizing currents <200 pA (pyramidal cells) or <160 pA (interneurons) were injected to keep the membrane potential steady. Series resistance was monitored throughout the experiment (20.3 ± 8.1 MΩ, mean ± SD, average SD = 2.3 MΩ, n = 38 contacts/dataseries in N = 25 cells) and post-hoc corrected (see 3.1.15). Bridge-balance compensation was applied in current-clamp.

Action-potentials were elicited by whole-cell current injection (1.5-3 nA, 0.5-2 ms, for improved signal-to-noise ratio (SNR) up to 4x (pyramidal cells) and 3x (interneurons) with 5 ms interstimulus interval). To avoid induction of plasticity, the interneuron was stimulated with frequency ≤ 0.1 Hz. Given the fast, $GABA_A$-receptor mediated time-course of the unitary inhibitory connections (typical uncaging evoked IPSC halfwidth 10 ms), the study was concentrated on spike-timing delays ±15 ms, based on the assumption that maximum inhibition would occur for coincidence of maximum conductances. At regular intervals between paired stimulations, the IPSC resulting from interneuron stimulation was measured in voltage-clamp at -40 mV holding potential, and series resistance was tracked with a holding command step from -70 to -75 mV.

In a subset of experiments, pipettes were retracted (with GΩ seals) after filling the cells for 15-20 minutes, to allow optimal dye diffusion and screening of the dendritic tree for axo-dendritic contacts. Cells were repatched 1-2 hours later without significant difference in membrane potential (0.3 ± 0.6 mV difference, mean ± SEM, n = 54).

2.3.9 Perforated patch-clamp

Perforated patch-clamp recordings were performed at 24 ± 2°C or 34 ± 1°C in organotypic hippocampal slice cultures with 5-50 μg/ml gramicidin + ≤0.2% DMSO dissolved by sonication in K-Gluconate internal, and IPSCs were evoked by extracellular stimulation with 10 μM DNQX + 20 μM D-AP5 in the bath. Integrity of the membrane was constantly monitored with Alexa 594 in the pipette. Holding potentials were posthoc corrected for the voltage drop across the series resistance (20-200 MΩ) by multiplying the holding current with the empirically measured series resistance. When estimating large series resistances by a 5 mV test pulse (R_s = 5 mV divided by peak current), small uncompensated drifts in pipette capacitance (C_{pip}) can produce an absolute error of several pA, which can result (if C_{pip} is undercompensated) in an underestimation of R_s or (if C_{pip} is overcompensated) in an overestimation of R_s. To overcome this, the current decay of the 5 mV test pulse was fitted exponentially, and the amplitude at current onset was extrapolated from this fit. Results using R_s estimated from peak current or extrapolated peak current were compared, and data were only included if the results were consistent between these measurements (ΔV_{rev}<1 mV). Data were discarded if the holding potential in I=0 was >-50 mV. Since a low chloride internal solution was used in whole-cell and perforated-patch recordings, liquid junction-potentials

were comparable and could therefore be neglected for the comparison. Finally, the 3D-model (2.6) predicts that even dramatic changes in reversal potential by ±10 mV increase or decrease the maximum Ca^{2+}-inhibition by ∼25%, but have a negligible effect on the spatio-temporal profile of Ca^{2+}-inhibition (simulations not shown).

2.3.10 Miniature recordings

Miniature IPSCs (miniIPSCs) were recorded at room temperature in ACSF containing 10 μM DNQX, 20 μM D-AP5 and 0.5 μM TTX from pyramidal cells in hippocampal slice cultures. Patch pipettes were backfilled with CsCl and tip filled with KCl, and cells were held at -70 mV in voltage clamp. Data were acquired with 20 kHz and 6 kHz Bessel filtered. Series resistance was online compensated 60-80% using the internal headstage circuitry with 3.6 - 4.5 kHz cutoff.

2.3.11 Interneuron firing patterns

For the characterization of GFP-positive interneurons in biolistic transfection experiments (3.1.5) or of GAD65-GFP-positive interneurons targeted during paired recordings (3.2.1), the protocol was as described in section 2.3.8 Electrophysiology. For the basic characterization of GFP-positive interneurons in the hippocampus of GAD65-GFP mice (Wierenga et al., 2010 and 3.1.3), transverse hippocampal slices were prepared from juvenile GAD65-GFP mice (P14—21) as described previously (Rinke et al., 2010). Whole-cell patch clamp recordings were in this case made at room temperature using a Multiclamp 700B amplifier (Molecular Devices). Signals were digitized at 5 kHz (Digidata 1440A and pClamp 10.2 Software; Molecular Devices) and Bessel filtered at 2 kHz. K-Methylsufate internal solution contained 30 μM Alexa Fluor 594.

For all experiments, firing patterns were recorded in current clamp by injecting 1-second current pulses of variable amplitude (Δ I = 1-5 pA around firing threshold; Δ I = 50 or 100 pA otherwise). Resting membrane potentials (<-40 mV) were measured at zero holding current soon after gaining whole cell access. Series resistances ranged from 5 to 25 MOhm. Bridge-balance compensation was applied (except for a subset of experiments reported in Wierenga et al., 2010). Recordings were not corrected for a liquid junction-potential.

2.3.12 Cell-attached stimulation

In a small subset of Ca^{2+} imaging experiments (n=5), interneurons were stimulated in cell-attached configuration. This was achieved by establishing GΩ-seal cell-attached recordings with intracellular solution, but without breaking through the membrane. For stimulation, the headstage was switched to lower resistivity circuitry to apply large voltage pulses (0.2-0.5 ms, 500 mV). If the membrane ruptured during stimulation, cell were subsequently kept and stimulated in whole-cell mode. However, since presynaptic cell-attached stimulations could not prevent run-down of IPSCs and just added an additional technical difficulty, this stimulation mode was not continued. Postsynaptic cell-attached stimulations were also possible, but did not allow control of the postsynaptic IPSC amplitude.

2.3.13 2-Photon imaging

For the imaging experiments, organotypic hippocampal slice cultures were transferred to a heated recording chamber (35 °C), where they were continuously perfused with carbogenated (95% O_2, 5% CO_2) ACSF. Two-photon imaging was accomplished with a custom-built two-photon laser-scanning microscope based on a Zeiss Axiovert 35 microscope with a 40x 1.15 NA

water-immersion objective (Olympus) and two tunable Ti-Sapphire lasers (Spectra-Physics). To excite fluorescent chromophores, the laser beams were tuned between 910 nm (excitation of GFP only) and 750 nm (excitation of Alexa 488 and calcein). To minimize phototoxicity, the imaging laser was blanked by the Pockels cell on the back-trace of each scan. To maximize SNR, the green PMT amplifier was disconnected from the power network and run on battery during Ca^{2+} imaging measurements.

The strategy was as follows: after filling the two cells (and usually retracting pipettes), the dendritic tree was exhaustively screened for axodendritic contacts along ~600μm of the somatodendritic axis, covering both basal and apical dendrites, and putative contacts were documented in high-resolution z-stacks. On average, 9.6 ± 4.8 (mean ± std, n = 26) putative contacts were mapped, of which 8.3 ± 4.4 were larger than 0 μm^2 and 5.5 ± 2.9 were larger than 1 μm^2, but very distal synapses might have been missed. In a minority of experiments, only part of the dendritic tree was screened (3 putative contacts on average) to circumvent repatching. One of the most prominent contacts was then selected and (after repatching) Ca^{2+}-imaging was performed at this contact. If possible, additional contacts were tested afterwards (up to 3 total). Furthermore, the data was carefully divided into single-contact and multiple-contact data, based on whether additional contacts were present in the vicinity (Fig. 32 D-E).

Structural imaging was performed at 750 nm (excitation of Alexa 468 and Alexa 594) and Ca^{2+} imaging was performed at 810 nm (excitation of Fluo-5F and Alexa 594). For Ca^{2+} imaging, signals were collected during 500-800 Hz line scans across the dendrite, also covering spines visible in the imaging plane. Often two spines could be covered on either side of the shaft. If more spines were present, selection was random. The data covered mostly mushroom and stubby spines. Ca^{2+} signals were quantified as increase in green fluorescence from baseline, normalized to the average red fluorescence ($\Delta Ca^{2+} = \Delta G/R$). Sweep averages contained a minimum of 5 data-points (10 on average). Ca^{2+} inhibition was calculated as average (1 - $\Delta Ca^{2+}_{inh}/\Delta Ca^{2+}_{ctrl}$) from a minimum of 5 inhibited (+) and 6 uninhibited (-) sweeps (-+-+-+-+-+-) by averaging the 2 inhibition values obtained from the (+-) and the (-+) series. The experimental design of alternating stimulations prevented potential artifacts in the level of inhibition due to drifts in basal Ca^{2+}.

2.3.14 Electron microscopy

Putative contacts between GFP-positive interneurons and pyramidal cells (filled with 60 μM Alexa 594) were mapped, and 2PLSM z-stacks were acquired for contact area quantification. Slices were fixed at 4°C for 15-40 hours (4% PFA, 0.2% glutaraldehyde, 0.1 M phosphate buffer, pH 7.4). After fixation, regions containing putative contacts were marked by near-infrared branding (Bishop et al., 2011). Slices were processed for electron microscopy as described previously (Scheuss and Bonhoeffer, 2014; Knott et al., 2009), with primary antibody: rabbit anti-GFP 1:1000 (Research Diagnostics, Flanders, NJ, USA), secondary antibody: Biotin-SP-conjugated goat anti-rabbit 1:300 (Jackson ImmunoResearch, West Grove, PA, USA), diaminobenzidine 0.04-0.08 mg/ml. Electron micrographs were acquired as described previously (Scheuss and Bonhoeffer, 2014), and analyzed with the RECONSTRUCT software (version 1.1.0.0, Synapse Web, Kristen M. Harris, PI, http://synapses.clm.utexas.edu; Fiala, 2005). Contacts were classified as synapses if the following three criteria were fulfilled: if (1) presynaptic vesicles, (2) a synaptic cleft and (3) a postsynaptic density or presynaptic mitochondria were found.

For 26 potential contacts identified in 2PLSM (with contact area 0–4.5 μm^2, distributed over 5 regions in 2 samples) the respective dendrite could be found back in EM. 7/26 axodendritic contacts were confirmed by the EM reconstructions (5/7 with DAB staining, 2/7 identified by geometry). 6/7 EM contacts had an inhibitory synapse. In the 7th EM contact,

several sections were missing which potentially contained the cleft, but it was counted as no synapse.

2.4 DATA ANALYSIS

Acquisition and online analysis of imaging data were performed using custom software written by Max Sperling in LabVIEW (National Instruments, Austin, TX, United States). Acquisition of electrophysiology data was performed using pClamp 10.3 (Molecular Devices, Sunnyvale, CA, USA). Off-line analysis of imaging and electrophysiology data was performed using custom routines written in MATLAB (The MathWorks, Natick, MA, USA).

2.4.1 Miniature analysis

For the analysis of miniature IPSCs (miniIPSCs), software was written in MATLAB and optimized using a simulated dataset based on an idealized miniIPSC waveform with realistic kinetics. Shortly, miniIPSCs were detected by a double threshold criterion. First, a template of length 1.5 ms was created by aligning and averaging several manually selected miniIPSCs from the given dataset, which covered 0.25 ms baseline, the rising phase, maximum and beginning decay of the average miniIPSC. Second, the template was correlated with the data, and miniIPSCs in the data were detected if a minimum correlation coefficient and a minimum scalefactor were exceeded. All events were checked manually, and false positives were deselected. The decay time-constant was determined by a monoexponential fit (if no additional events occurred within 20 ms). Data were lowpass filtered with a 1 kHz/0.5 kHz Gaussian filter for risetime/amplitude estimation.

2.4.2 Interneuron classification

The following 22 parameters were quantified for each firing pattern. The continuous frequency for each current step (1 s) was quantified as the total number of spikes, and (1) the saturating frequency was determined as maximum continuous frequency. (2) The maximum initial frequency was defined as the mean reciprocal of the first inter-spike intervals for the 5 longest spike trains. (3) The adaptation threshold was defined as the current amplitude at maximum continuous frequency, above which the continuous frequency decreased. (4) A binary variable quantified whether rebound spikes occurred after current-offset. (5) The rheobase was defined as the minimum current amplitude which elicited action-potentials. (6) Action-potential thresholds were defined as the voltage at which the slope trajectory reached 10 mV/ms (after subtracting residual capacitive artifacts, if necessary). (7) Action-potential amplitudes were measured from threshold. (8) Action-potential halfwidth was defined as the interpolated time-difference between half amplitude crossings. (9) Afterhyperpolarization (AHP) was defined as the difference between action-potential threshold and the minimum membrane potential attained before the next AP. Action-potential parameters (6-9) were determined as the average over the first action-potentials per train. Threshold values were averaged only for the smallest three superthreshold steps to minimize influence of uncompensated series resistance. Accomodation was quantified by the mean ratio of the 5th and first value (early accomodation), and the ratio of the last and fifth value (late accomodation) for the parameters spike amplitude (10-11), frequency (12-13) and halfwidth (14-15). Accommodation values were determined as averages of the five longest spike trains. (16) Irregular spiking was defined by the coefficient of variation (CV) of the inter spike intervals exceeding a threshold of 0.5. The delay to the first spike was determined for small current steps eliciting a single spike (17: delay 1) or the small current steps eliciting more than one spike (18: delay 2). If delay 1 exceeded 100 ms, the cell was classified as delayed onset firing. In addition,

passive cell parameters were determined. (19) Input resistances were measured by using a linear regression of voltage deflections in response to small hyper- or depolarizing current steps (between 5 pA and 50 pA). (20) Membrane time constants were determined by fitting an exponential curve to responses to the same small current steps at 0.2–500 ms from current onset. (21) The amplitude of the sag current was determined for hyperpolarizing steps as the potential difference between the minimum and steady-state voltages attained during current injection, and (22) its time constant from a monoexponential fit between minimum and sag steady-state decay. Both parameters depended linearly on the steady-state voltage upon current injection, and values were inter- or extrapolated at -100 mV to allow comparison. Burst were defined by step increases of the interspike intervals by a factor of 5. Burst frequencies refer to the mean frequency during a burst, averaged over all detected bursts.

Cells were classified following the scheme of Miyoshi et al., 2010 by the following criteria: Cells with delayed onset firing and early amplitude accomodation <1 were classified as delayed non-fast spiking (dNFS3). Cells with delayed onset firing and early amplitude accomodation >1 were classified as late spiking (LS). The cell was considered type late spiking 1 (LS1) if delay 1 and 2 exceeded 100 ms, and late spiking 2 (LS2) if only delay 1 exceeded 100 ms. Cells without delayed onset, but with onset burst and no adaptation (for current steps <9x rheobase) were classified as burst non-adapting type 2 (bNA2). No "hump" around threshold was observed as typical for bNA1. Cells which adapted already at intermediate current steps (<3x rheobase) were classified as strongly adapting (or fast adapting, fAD).

2.4.3 Quantification of spike-timing

Due to trial-to-trial variability and differences in membrane time-constants, the time between current injection start and AP start varied. For accurate quantification of spike-timing, stimulation start was defined by the characteristic kink in the $\Delta V/V$ plot (Naundorf et al., 2006). Since stimulation artifacts sometimes overlaid the start of the AP, thresholds of 10-250 V/s were defined per stimulation series, and stimulation start was defined as interpolated time of threshold-crossing. Since voltage gradients change very rapidly at the kink, the time of threshold-crossing is insensitive to the choice of threshold value (typical second derivative 50 V/s per 0.05 ms), and therefore spike-timing values are comparable between experiments. For paired stimulations, the membrane potential of the pyramidal cell at 10 ms after the last stimulation was quantified to estimate IPSP size (parts of the IPSP coinciding with the spikes could not be quantified). However, small IPSCs failed to produce detectable IPSPs due to the low driving force at resting membrane potential.

2.4.4 Control of IPSC stability

Experiments lasted up to 4 hours. Stimulation protocols were partially pseudo-randomized to exclude run-down artifacts. In addition, IPSC amplitudes were monitored, also in between Ca^{2+} imaging sessions, to detect potential run-down of synaptic strength. IPSC amplitudes were post-hoc corrected for series resistance changes (3.1.15). IPSC amplitudes often transiently increased within 10-20 minutes after gaining whole-cell access (Fig. 7 A), a phenomenon which has been described previously (Bouhours et al., 2011) and is not due to chloride diffusion (Fig. 7 B). Therefore the reference IPSC amplitude mean and standard error (SEM) were measured shortly after gaining whole-cell access or during steady-state. A running average filter of width 5 was applied to the IPSC data, and the corresponding IPSC amplitudes for each Ca^{2+} imaging time-point were predicted by interpolation. Only data with corresponding IPSC amplitude were included (with exception of the pairwise comparison in Fig. 39). When IPSC amplitudes fell below the 95% prediction interval of the reference

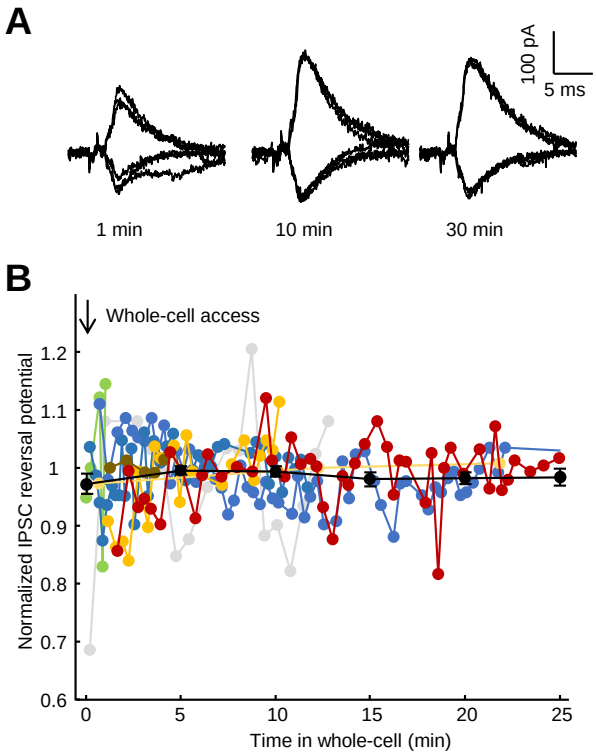

Figure 7: Stability of reversal potentials. (A) Reversal potentials were estimated from stepping between holding command -100 mV and -40 mV (representative IPSCs shown). While the absolute IPSC amplitudes showed a characteristic increase within the first minutes, reversals remained stable. (B) Reversal potentials were stable over prolonged time intervals (n=8, mean ± SEM for 5 minute bins displayed in black, colors code for different cells). Whole-cell access was gained at 0.

measurement for more than 2 minutes ('run-down'), in parallel and subsequently acquired Ca^{2+} imaging data were discarded. In the dataset used for analysis, I looked for correlations between Ca^{2+} inhibition and (interpolated) IPSC amplitudes or data acquisition time (under equivalent stimulation conditions). Correlation coefficients for all three comparisons (minimum 10 data-points, n = 113-118) were distributed symmetrical around 0, with no significant offset (signrank p = 0.24-0.96). The same was true for the subset of data collected at contacts where significant inhibition was detected (n = 70-71, p = 0.06-0.96). Finally, I repeated the analysis for Fig. 36 (distance-dependence) and Fig. 42 (spike-timing-dependence) for IPSC/IPSP amplitudes and data acquisition times instead of Ca^{2+} inhibition. In all cases, the analysis did not reproduce a similar profile of the respective parameter (Fig. 8).

2.4.5 Series resistance correction

See 3.1.15 Results, Series resistance correction for dendritic inhibitory inputs.

2.4.6 Spine plasticity quantification

Spine volume was quantified as summed intensity, which is less sensitive to shot-noise than maximum intensity and does not underestimate structures that are not fully sub-resolution (in contrast to maximum intensity). Prior to analysis, images were median-filtered with a circular mask of equivalent radius 0.13 μm. Polygonal regions of interest (ROIs) were manually defined for the background, the spines (surrounding the test spine and multiple control spines) and multiple dendrite segments. To compensate for image-drift and moderate xy-movements of the spines, for each ROI (except background) consecutive stacks were aligned in xy by normalized cross-correlation of the mean-z-projection, with reference to an image subregion with predefined size surrounding the ROI, and subsequently aligned in z based on the maximum integral over the ROI. For each time-point, mean fluorescence of each ROI (av-

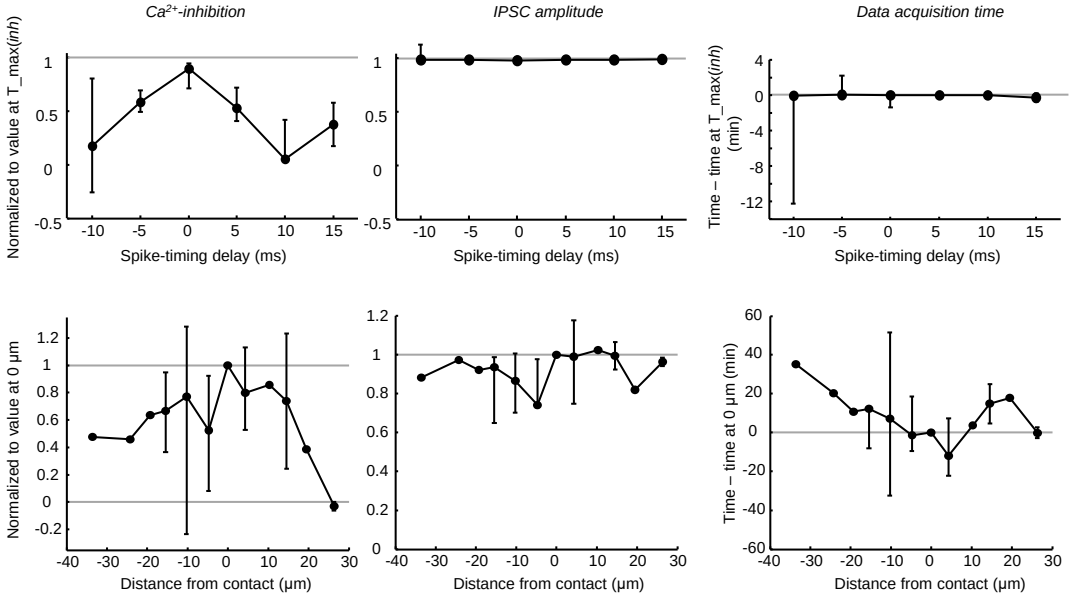

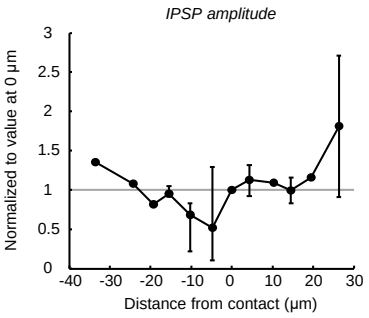

Figure 8: Results are independent of variations in synaptic response strength. To rule out pseudo-correlations, I controlled for changes in IPSC amplitudes or data acquisition times. I repeated the Ca^{2+} inhibition analysis of distance-dependence (upper panels, for Ca^{2+} inhibition > 0) or spike-timing-dependence (lower panels, for Ca^{2+} inhibition > 0.085), analyzing IPSC amplitudes or data acquisition time in place of Ca^{2+} inhibition (IPSP only comparable for equal spike-timing, right panel). Data were normalized to the respective parameter value at 0 μm (upper panels), or to the parameter value of the spike-timing for which maximum inhibition had occurred ($T_{max(inh)}$). Shown are median values per 5 μm / 5 ms with errorbars indicating bootstrapped 70% confidence intervals. In all cases, the control analysis did not reproduce a similar distance-dependence or spike-timing-dependence of the respective parameter.

eraged over 4 μm around its maximum) were normalized to the average of all dendritic ROIs, and subsequently averaged to its average baseline value (i.e. before plasticity induction).

2.4.7 Structure selection

In line scans, structures (shafts or spines) were selected based on the time-averaged intensity profile in the red channel. The selection of structures was semi-automated: structure borders were automatically set to the width at 20% of the local maximum respectively at minima between detected structures. This selection criterion had been determined in simulations to optimize SNR (which increases with the number of photons detected, but decreases if the selection largely exceeds the true diameter). All structure selections were manually confirmed or corrected.

2.4.8 Contact area quantification

For each presumable contact, z-stacks of 20x20 μm and 0.05 μm/pixel were acquired with z-steps of 0.5 μm, which fully covered the contact. After subtraction of image background and applying a 2D median filter (with area of an equivalent circle of radius 0.19 μm), two ROIs were selected which covered the axonal bouton (green channel), respectively the contacted dendritic shaft or spine (red channel). The equivalent radius of the median filter (0.19 μm) was chosen such that it matched the standard deviation of the point-spread function. Both structures (bouton and dendrite) were then thresholded at their half-maximum in the respective channel. Finally, the axo-dendritic contact area was estimated by integrating over all red voxel surfaces which were adjacent to a green voxel. The resulting number is reported as "contact area", since it approximates the surface area of the dendrite that is contacted by the axon. By the cubic approximation, spherical structures (such as idealized boutons or spines) will be overestimated by a factor of $6\pi \approx 2$ (reported values are uncorrected). The thresholding at half-maximum is unbiased, i.e. it does not depend on exact ROI definition, as long as the ROI covers the maximum. Furthermore, similar results were obtained for different choices of median filter radius. The half-width of sub-resolution structures are, in addition to diffraction limits, overestimated up to 15% by the filtering (15% for diameter <0.1 μm, 8% for diameter 0.5 μm, 1% for diameter 1 μm, as estimated by convolving a square of varying size with the empirical point-spread-function in xy, and comparing the resulting full-width at half-maximum with or without applying the median filter).

2.4.9 Distance-measurements

The distance from the synaptic contact to the soma or to the imaging line was measured as integrated path-length from the contact center to the soma circumference, or to the intersection center of imaging line and shaft respectively, by manually defining a trajectory along the dendritic skeleton. For dendritic spines, the shaft center closest to the spine neck was taken as a reference point. Euclidean distance was defined by the length of the vector between start- and end-point of the trajectory. For estimating length-constants, the data recorded at minimum distance to the contact (<2.8 μm, on average 1 μm) were taken as the 0 μm reference.

2.4.10 Analysis of calcium imaging

For Ca^{2+} imaging, signals in both channels were background-subtracted. The borders of dendritic shafts and spines were automatically detected in the red channel (see 2.4.7). For quantification of ΔCa^{2+}, Ca^{2+} transients were lowpass-filtered (50 Hz Gaussian filter), and the maximum within 40 ms after stimulation was determined after subtraction of baseline (minimum 20 ms). To calculate average ΔCa^{2+}, raw Ca^{2+} transients were aligned to the first pyramidal AP kink, subsampled at 10 kHz and averaged prior to lowpass-filtering.

Length-constants were estimated by performing an exponential fit to the Ca^{2+} inhibition weighted by the inverse bootstrapped variance of each measurement. The robustness of the length-constant estimates (Fig. 9 A) and of the cross-validation significance of optimal spike-timing (Fig. 9 B) was confirmed by repeating the analysis with a sliding threshold (data selected by an unbiased threshold criterion of Ca^{2+} inhibition $> \theta$ for any distance-bin, respectively any spike-timing-bin). Alignment-artifacts ("noise-fitting") in the spike-timing profile were additionally ruled out by cross-alignment: One half (D_1) of each data-set D was aligned to the optimal spike-timing observed in the other half (D_2), and vice versa. For each 5 ms time-bin, median values were determined after alignment of all D_1 and D_2 subsets, and subsequently averaged. Similar spike-timing profiles as in Fig. 42 were obtained (Fig. 10). For spike-timing profiles shown in Fig. 42 B and D, only data with cross-validated optimal

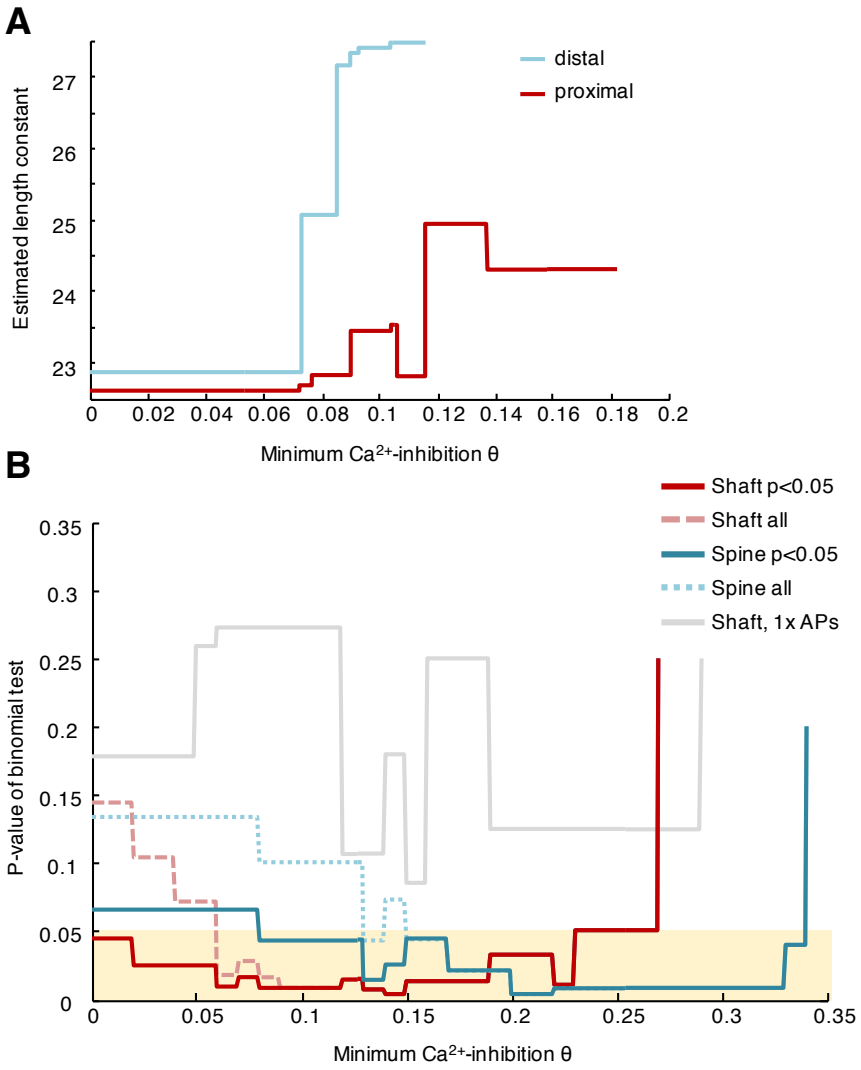

Figure 9: Robustness of results for different threshold choices. (A) Length-constants were estimated by performing an exponential fit to the Ca^{2+} inhibition weighted by the inverse bootstrapped variance of each measurement, after selecting experiments based on an unbiased threshold criterion of Ca^{2+} inhibition $> \theta$ for any distance-bin. Plotted are estimated length-constants against threshold θ. The estimated length-constants depended on the choice of threshold to some degree, indicating that the length-constants were not completely uniform across experiments. Stronger Ca^{2+} inhibition tended to result in longer length-constants. (B) Significant reproducibility of optimal spike-timing was indicated by a binomial test, after selecting experiment based on an unbiased threshold criterion of Ca^{2+} inhibition $> \theta$ for any spike-timing-bin. Plotted are p-values obtained for thresholds between 0 and maximum Ca^{2+} inhibition. The yellow bar indicates significance of the binomial test. For small thresholds, noise dominates and occludes the spike-timing-dependence, unless the analysis is limited to datasets for which overall significant Ca^{2+} inhibition was reported (red solid line). For large thresholds, the drop in sample size results in larger p-values. For shaft data, significance is robustly reported for thresholds up to 0.23, while for spine data with inherently lower SNR, significance is reported only for larger thresholds between 0.08 and 0.33. Data acquired with the single stimulation paradigm (lowest SNR) does not reach significance.

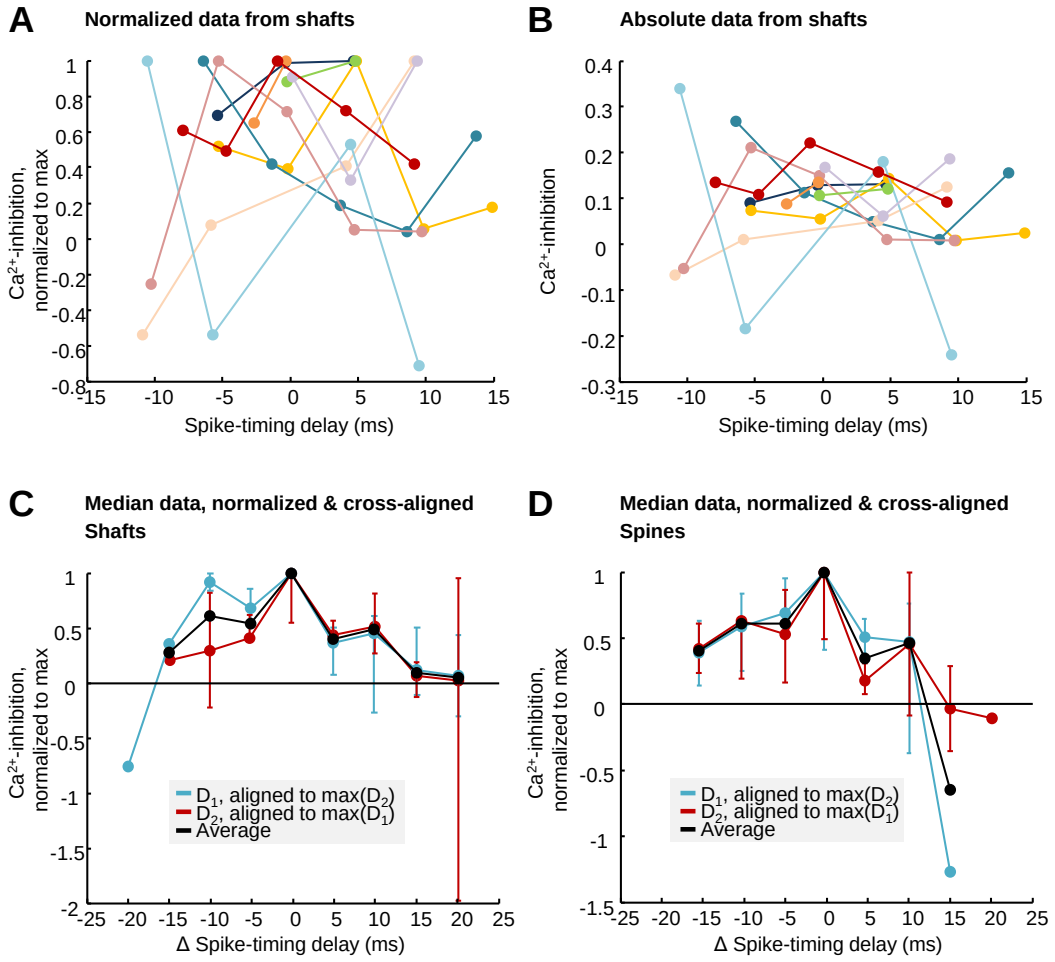

Figure 10: Spike-timing-dependence of Ca^{2+} inhibition. (A-B) Data of single experiments from Fig. 42 is shown after (A) and before (B) normalization. Apparently, the optimal spike-timing varied between recordings. Therefore, (C-D) cross-alignment was performed to rule out alignment artifacts. One half (D_1) of each data-set D was aligned to the optimal spike-timing observed in the other half (D_2), and vice versa. For each 5 ms time-bin, median values were determined after alignment of all D_1 (blue) and D_2 (red), and subsequently averaged (black). The same procedure was performed on data from shafts (C) or spines (D). Error bars indicate bootstrapped 70% confidence intervals.

spike-timing were averaged.

For analyses including Ca^{2+} transients close to baseline (Fig. 11 C, 12 B, 33 C, 34 A-C, 38), integrals were used to minimize errors due to division by small numbers. Ca^{2+} integrals and amplitudes were highly correlated (R=0.99, $p < 0.0001$, median ratio peak/integral of 1.35). Ca^{2+} amplitudes at dendritic spines and the neighboring dendritic shafts were comparable (Fig. 12 A). Measurements were excluded from analysis if no significant Ca^{2+} peak was detected (SNR $\leq$ 3 of both $Ca^{2+}{}_{inh}$ and $Ca^{2+}{}_{ctrl}$ for amplitudes, or $\leq$ 1.5 for integrals), if the green baseline was unstable (significant difference between $Ca^{2+}{}_{inh}$ and $Ca^{2+}{}_{ctrl}$ baseline indicated by Wilcoxon rank-sum $p < 0.01$), if stimulation failed to elicit a spike, or if spontaneous spikes occurred. For analysis of spike-timing-dependence, only data recorded within ± 5 μm were included; for analysis of distance-dependence, only data with simultaneous spike-timing (average between -1.4 and 0 ms) were included. For analyzing branch specificity (Fig. 39), data recorded within 35 μm of a contact with area > 1 μm^2 and with SNR > 10 were included if and only if no contact was detected on the neighboring branch.

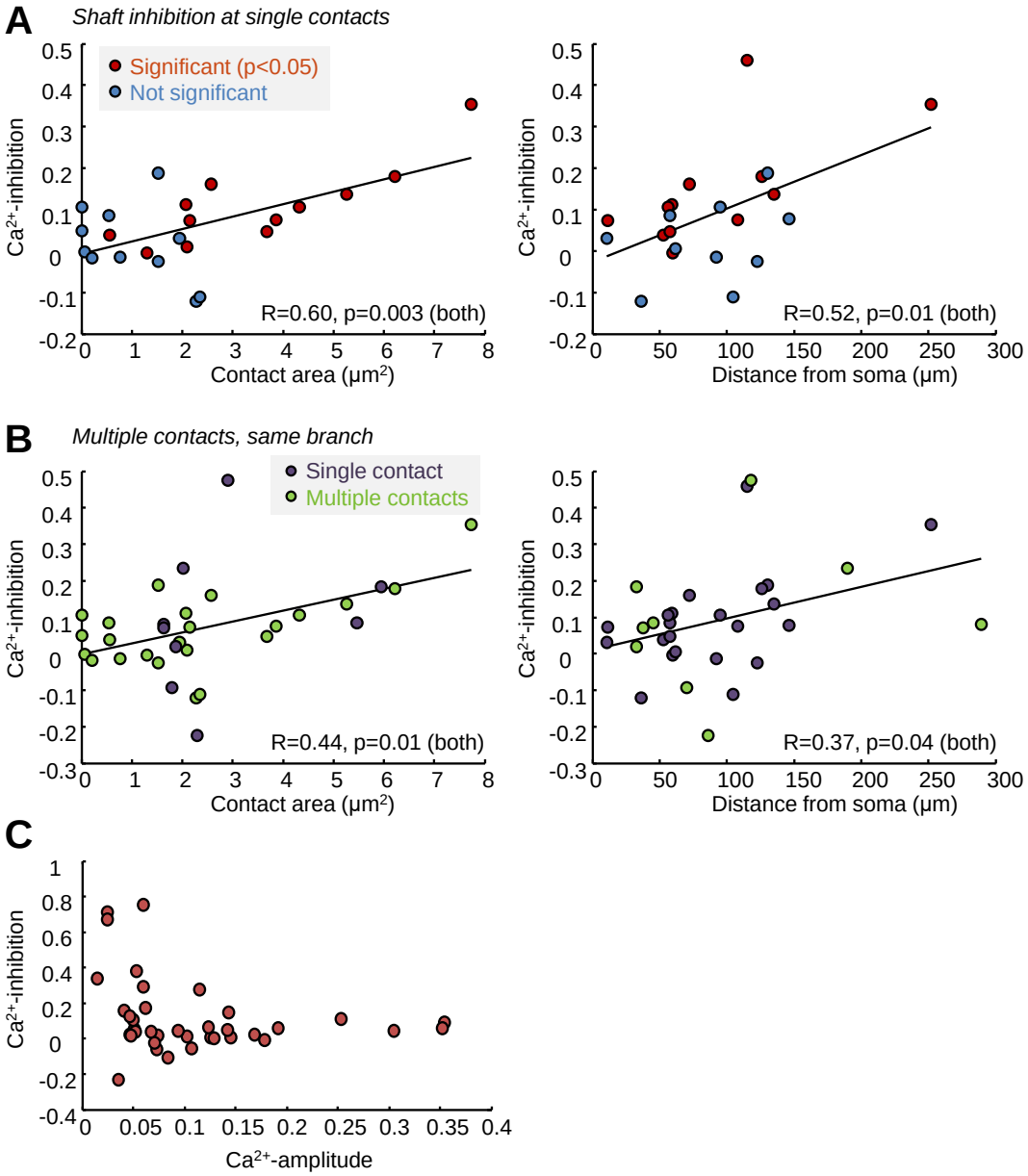

Figure 11: Inhibition at 0 μm and with 0 ms delay. (A-C) Inhibition at minimum distance ($\leq$7.5 μm) and spike-timing delay ($\leq$2.5 ms) was similarly dependent on axo-dendritic contact area (left panel) and distance between contact and soma (right panel), for both single contacts (A) and multiple contacts (B), and shows the characteristic relationship with Ca^{2+} amplitude (C). Reported Pearson correlation coefficients refer to all displayed data in each graph.

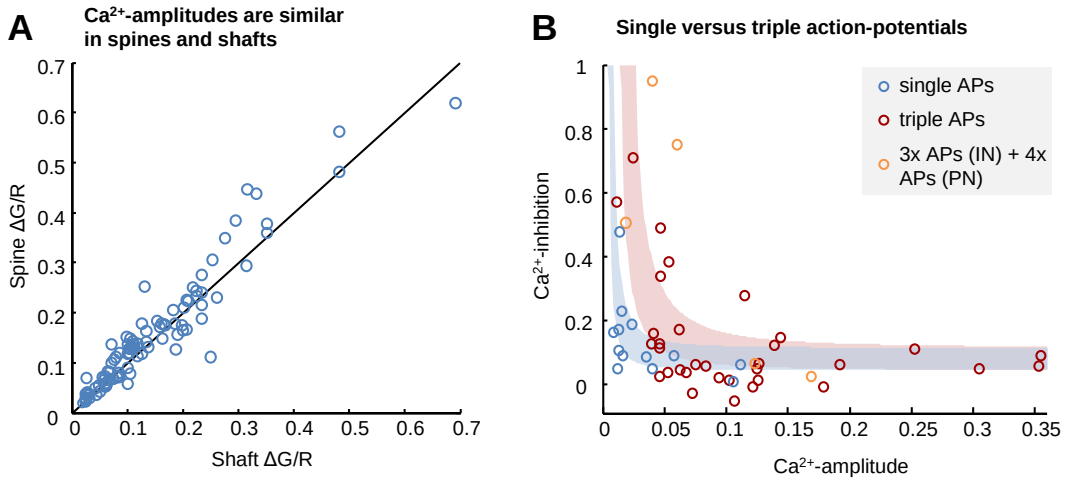

Figure 12: Methodology. (A) Backpropagating APs fully invaded dendritic spines and Ca^{2+} transients reached similar amplitudes. Spine ΔG/R plotted versus shaft ΔG/R scattered around the unity line. (B) The Ca^{2+} inhibition data indicates that the average Ca^{2+} inhibition per spike is preserved in the 3x stimulation paradigm. Red area: model fit to the 3x stimulation data, blue area: same fit scaled to 1/3 of the Ca^{2+} amplitudes matches the 1x stimulation data very well. Fit shown for 2-6 μm^2 contact area. On a side note: The dynamic properties of IPSC in response to 3x APs were variable, as it can be expected for dendritic synapses. According to the simulations, equi-conductant synaptic inputs at distal locations can sum sublinearly due to suboptimal space-clamp and reduced driving force, while equi-conductant inputs at proximal locations can sum supralinearly due to closing of active conductances around holding (-40 mV). Therefore, a "depressing" or "facilitating" IPSC summation does not allow a conclusion as to whether inhibitory conductances were equal, increasing or decreasing.

For analyzing spine-shaft differences (Fig. 40), only data recorded within 35 μm of a contact and with spike-timing >-7.5 ms and <7.5 ms were included. One pyramidal neuron excited additional interneurons (prominent disynaptic IPSPs detected) and was excluded to rule out potential interference. In Fig. 31 E, 32, 33, 34, reported Ca^{2+} inhibition refers to Ca^{2+} inhibition under optimal conditions: data from different spike-timing and distance conditions were averaged in 5 ms/5 μm bins (minimum 5 data-points per bin) and the maximum Ca^{2+} inhibition across conditions was reported. Similar results were obtained for Ca^{2+} inhibition at the putative contact and without time delay (Fig. 11). For stimulations with single APs, the relationship between Ca^{2+} inhibition and Ca^{2+} amplitude, scaled by a factor of 3, is well predicted by the model fitted to data from stimulation with triple APs (Fig. 12 B), confirming that Ca^{2+} inhibition per spike is on average preserved between the stimulation paradigms.

2.5 STATISTICS

Mean ± SD or ± SEM are presented as noted. To detect statistically significant inhibition in an unbiased approach, the non-parametric sign-test was performed on the full Ca^{2+} inhibition dataset of all stimulations between ±15 μm distance and ±15 ms spike-timing delay, calculated based on ΔCa^{2+} integrated over 100 ms (Bonferroni-Holm-correction was applied for different stimulation protocols). The significant absence of inhibition was inferred by a one-tailed sign-test with 0.05 upper bound. In Fig. 42, spike-timing-dependence was considered significant if the number of datasets, for which optimal spike-timing was reproducible after splitting the dataset in half, was significantly above chance levels ($p < 0.05$ with bino-

mial test). Variance and standard error of Ca^{2+} inhibition were estimated by bootstrapping. Errors of inhibition ratios were estimated by error propagation.

Based on the posthoc EM estimates of synapse probability (Fig. 30 B) and the respective contact areas of the samples, it can be estimated as a lower bound that at least 50% of selected putative contacts are synaptic contacts. The data have been additionally selected based on inhibition thresholds (distance/spike-timing analysis Fig. 36 and 42) and significance (selected data in the spine analysis Fig. 40 and spike-timing analysis Fig. 42, except for 1x data), in which case the false-positive rate is only ∼5%. Also for the distance analysis, equivalent results (23-27 μm) are obtained if only data with >2 μm^2 contact area or only significant data are included.

2.6 NEURON MODELING

A previously established morphologically-realistic model (Poirazi et al., 2003a; Poirazi et al., 2003b) of a hippocampal CA1 pyramidal cell (n123 from the Duke-Southampton archive, rat hippocampus) was modified. Briefly, the multi-compartment model included a Ca^{2+} extrusion/buffering mechanism and multiple ionic currents. To prevent the backpropagating APs from evoking secondary spikes in terminal branches, which was not consistent with the present data, axial resistance was increased uniformly to R_a = 100 Ω·cm and the density of one Ca^{2+}-dependent K^+-current (mykca) by a factor of 3. Additional minor modifications: the density of the car mechanism was set to 0, the surface-volume-ratio in the cad mechanism was corrected for dendritic diameter (see Anwar et al., 2014), the internal Ca^{2+} concentration cai was updated by the cat mechanism, potassium reversal potential was set ek = -80 mV uniformly, and the current-balance function (which forces e_pas to arbitrarily negative potentials) was turned off.

Spines were implemented with realistic geometry (neck width 0.147 μm, length 0.667 μm, head width and length 0.519 μm, see Tønnesen et al., 2014) and equipped with the same current densities as the neighboring shaft. GABAergic synapses were modeled as α-synapses (τ = 1 ms) with mixed chloride and bicarbonate conductance (intracellular chloride $[Cl^-]_i$ = 7.5 mM). Mechanisms for $GABA_A$-current and chloride accumulation were adapted from Jedlicka et al., 2011. Varying τ between 0.5 and 2 ms or $[Cl^-]_i$ between 5 and 10 mM had little influence on the results. Excitatory synapses were placed on the spine head and modeled as α-synapses with τ = 0.5 ms and 0 mV reversal. Equivalent results (data not shown) were obtained for the VGCC-mediated Ca^{2+} influx induced by AMPA + NMDA receptors (adapted from Gómez González et al., 2011). Simulations were performed for 34°C with fixed time-step integration (0.025 ms) and sufficiently fine segmentation (equivalent results with 3x nseg obtained). The model was implemented in NEURON (Carnevale and Hines, 2006) and the code for all simulations will be made available at the ModelDB database (http://senselab.med.yale.edu/modeldb).

3 RESULTS

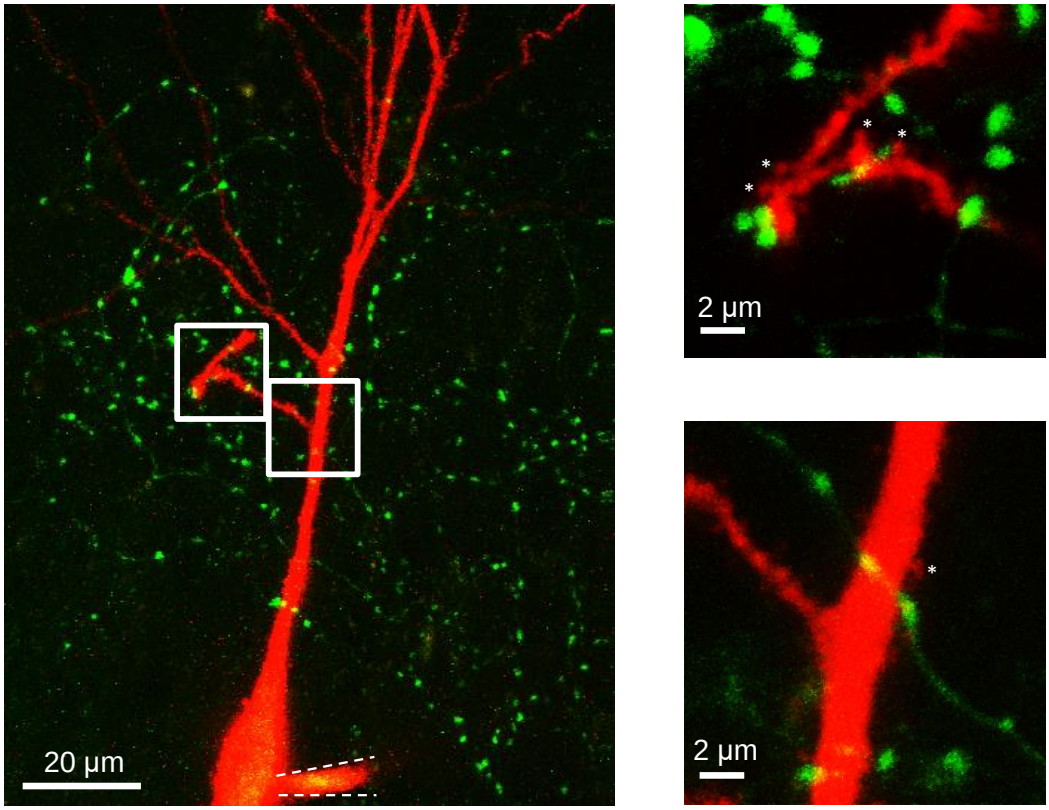

Figure 13: Visualizing the morphological correlates of synapses by 2-photon laser scanning microscopy (2PLSM). A hippocampal pyramidal cell and a GABAergic interneuron were filled with fluorescent markers for visualization in 2PLSM. The apical dendrites of the pyramidal cell (red) are contacted by the inhibitory axon (green). Right panels: zoom-in to boxed areas in the left panel. Morphological correlates of putative inhibitory synapses (axodendritic contacts, yellow), and putative excitatory synapses (spines, some indicated by stars) are visualized. Interneuron: GAD65-GFP-positive and Alexa 488 filled. Pyramidal cell: Alexa 594 filled via patch-pipette (dotted contours in the left panel).

3.1 EXPERIMENTAL PARADIGM AND TOOL-DEVELOPMENT

3.1.1 Objectives

Structural correlates of synapses, like dendritic spines or axo-dendritic proximities between inhibitory axons and postsynaptic dendrites (Fig. 13), can be visualized in intact neuronal circuits by non-invasive high-resolution 2-photon laser scanning microscopy (2PLSM), opening the door to also studying the function of such individual synaptic contacts. While the function of individual excitatory synapses on spines had been intensely studied by 2-photon Ca^{2+} imaging, the function of individual inhibitory synapses had not yet been addressed with

synaptic resolution. Establishing a paradigm to study the function of individual dendritic GABAergic synapses required, on one hand, a reliable and selective method to stimulate individual inhibitory synapse, and on the other hand, a sensitive paradigm to readout the potentially small effects of individual inhibitory synapses.

3.1.2 Choice of model system

As a model system, organotypic hippocampal slice cultures where chosen (Stoppini et al., 1991; Gähwiler, 1981, reviewed by Gähwiler et al., 1997), which offer several technical advantages over acute slices — accessibility for genetic modifications, excellent optical access and electrical recording conditions (no dead or truncated cells present), as well as stability over several hours of recording — while anatomical structure and cell physiology are still close to the in situ situation (De Simoni et al., 2003; Streit et al., 1989).

By the time this study was initiated, a limited number of genetic mouse models were already available in which GABAergic interneurons were labeled with GFP. For example, promoter sequences for the two isoforms of GABA-synthesizing enzymes glutamic acid decarboxylase GAD56 and GAD67 selectively label large subpopulations of GABAergic interneurons, depending on the random transgene insertion site (Oliva et al., 2000). GAD65-GFP mice (López-Bendito et al., 2004) were chosen for the purpose of this study, which had been previously selected to image dendritic GABAergic synapses pre- and postsynaptically with good SNR at 2-photon resolution (Wierenga et al., 2008).

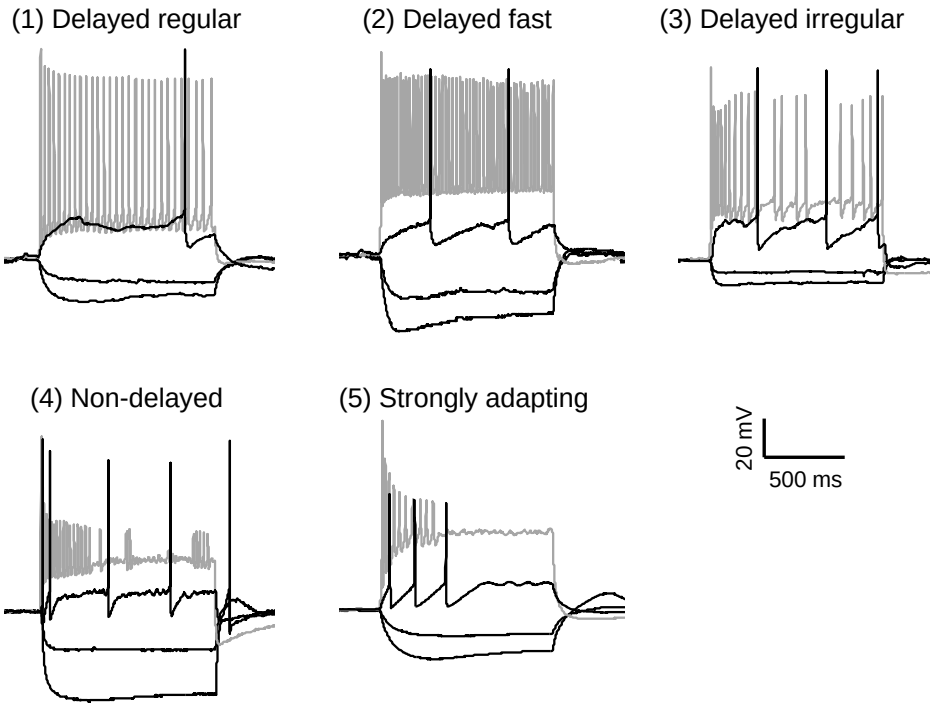

Figure 14: Interneuron classification. Electrophysiological classification of GAD65-GFP positive GABAergic interneurons in acute slices at room temperature. Representative firing patterns of the five classified groups (1) delayed onset regular, (2) delayed onset fast, (3) delayed onset irregular, (4) non-delayed onset firing and (5) fast adapting (Wierenga et al., 2010). Raw data of (2) and (4) were acquired by Ilka Rinke.

3.1.3 Characterization of GABAergic interneurons

In order to understand which subpopulation of GABAergic interneurons is targeted in the hippocampus of GAD65-GFP mice, a separate study was conducted (Wierenga et al., 2010), for which I recorded and analyzed passive properties and firing patterns of GFP-positive interneurons in acute slices from GAD65-GFP mice at room temperature. Our study concluded that GAD65-GFP cells are mostly dendrite-targeting GABAergic interneurons which express either Reelin (69±2 %, mean mean ± SEM) or VIP (15±2 %), and therefore most likely have their developmental origin in the caudal ganglionic eminence (CGE, Miyoshi et al., 2010). I designed the electrophysiological characterization of the GFP-labeled interneurons according to the Petilla nomenclature (Ascoli et al., 2008) and quantified 22 different, yet partially correlated, parameters (see 2.4.2). According to this analysis, cells could be broadly classified into five subgroups (Fig. 14), three groups of cells with delayed onset firing and moderate frequency adaption, a group of non-delayed, mostly irregular firing, and a group of strongly adapting cells:

1. delayed onset, regular spiking (21/48),
2. delayed onset, fast spiking (6/48),
3. delayed onset, irregular spiking cells (7/48),
4. non-delayed spiking cells (7/48) and
5. strongly adapting cells (7/48).

Cells were defined as delayed onset firing if they fired their first action-potential with >100 ms delay upon current injection around threshold. Fast spiking interneurons were defined by their high firing rates >50 Hz (59 ± 2 Hz, mean ± SEM). In addition, they displayed action-potentials with shorter width (1.25 ± 0.07 ms versus 1.62 ± 0.07 ms, group 2 versus 1, mean ± SEM) and frequently fired rebound action-potentials upon hyperpolarizing current injection (5/6 cells). Irregular spiking interneurons were defined by the variance of inter-spike intervals (coefficient of variation ≥0.5, 0.68 ± 0.11, mean ± SEM). In most delayed onset cells (group 1-3), the first action-potential was delayed ≥100 ms even for current injections which evoked more than one action-potential (corresponding to the LS1 type of Miyoshi et al., 2010). In group 4 interneurons, the first action-potential around threshold was not delayed (occuring at 29 ± 7 ms, mean ± SEM). In addition, they displayed a fast membrane time constant (21 ± 4 ms versus 63 ± 9 ms, group 4 versus 1), low input resistance (284 ± 59 MΩ versus 610 ± 80 MΩ, group 4 versus 1) and low action-potential threshold (-42 ± 1 mV versus -35 ± 1 mV, group 4 versus 1). Finally, group 5 interneurons were strongly adapting, i.e. they stopped firing prematurely before the end of moderate (<3x rheobase) current injections. In addition, they displayed small action-potential amplitudes. None of the recorded GFP-labeled interneurons showed intrinsic burst firing.

For the subsequent study addressing Ca^{2+} inhibition by individual GABAergic dendritic synapses, GFP-positive interneurons were additionally selected based on the following criteria:

1. Somata located in stratum oriens, radiatum, or close to the pyramidal cell layer
2. Detectable postsynaptic IPSC in a randomly patched pyramidal cell in the vicinity
3. Visually detectable proximity between the inhibitory axon and the postsynaptic pyramidal cell dendrites (i.e. putative inhibitory synaptic contacts)

GABAergic interneurons targeted by this procedure were also analyzed electrophysiologically and morphologically. Briefly, paired patch-clamp recordings were performed at 35°C

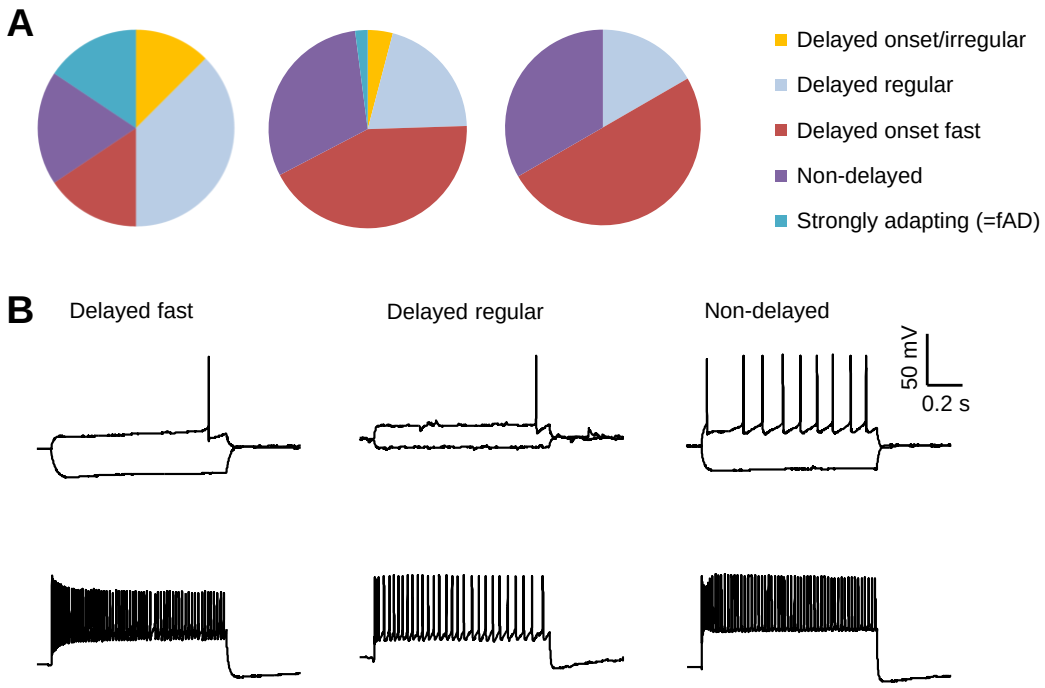

Figure 15: GABAergic interneurons selected for studying Ca^{2+} inhibition. (A) Comparison of the firing patterns of GAD65-GFP positive GABAergic interneurons: overall population of interneurons (INs) as analyzed in Wierenga et al., 2010 (left panel, n=48), INs which fulfill selection criteria 1-2 (middle panel, n=49), and subset of INs included in the Ca^{2+} inhibition dataset (right panel, n=12), excluding e.g. cells with no contacts detected or with IPSC rundown. (B) Representative firing pattern of the 3 groups delayed fast/delayed regular/non-delayed firing interneurons.

from a GFP-positive interneuron and a nearby pyramidal cell in GAD65-GFP organotypic hippocampal slice cultures. IPSCs in the pyramidal cell were evoked by current injection to the interneuron, and both cells were filled with fluorescent markers for detailed morphological analysis by 2-photon imaging. In interneurons selected by criterion (1-2), all 5 groups described in the previous paragraph were present, although strongly adapting and irregular spiking interneurons were strongly underrepresented (Fig. 15 A, left versus middle panel). GABAergic interneurons fulfilling all three criteria (1-3), only the major groups delayed onset regular or fast spiking and non-delayed onset spiking were represented (Fig. 15 A, right panel, and B). Altogether, the selected GABAergic interneurons were multipolar (36 of 36 morphologically analyzed) and displayed regular firing patterns with moderate frequency and/or amplitude adaptation (Fig. 15 B).

Looking more closely at the firing characteristics of the interneurons included in the study on Ca^{2+} inhibition, all delayed onset cells could be well classified by the scheme of Miyoshi et al., 2010 as delayed non-fast spiking (dNFS3), late-spiking (LS1 or LS2), burst non-adapting type 2 (bNA2) or fast adapting (fAD) cells. Delayed onset fast-spiking cells were almost exclusively (20/21) dNFS3 cells (1/21 was LS1), while delayed regular cells were mostly (9/10) LS1 or LS2 (1/10 was dNFS3), indicating that the firing frequency criterion indeed separated two distinct interneuron groups. The dNFS3 cells show delayed firing at threshold, regular firing with slight frequency adaptation, continuing spike height adaptation, and a sharp AHP as in Miyoshi et al., 2010. The nomenclature "delayed non fast spiking" is slightly misleading in this regard, since this group of cells is the fastest firing amongst the CGE derived INs (78.4 ± 19.9 Hz in Miyoshi et al., 2010, room temperature, 82.9 ± 22.2 Hz in my sample, 34°C, mean ± SD). Therefore, "moderately-fast-spiking" is an appropriate description for this

cell group. The fast adapting fAD cell was, as in Miyoshi et al., 2010, electrically smaller than all other groups and showed hyperpolarization after current offset. Notably, no intrinsic bursters (dIB or sIB) or burst non-adapting type 1 cells (bNA1) were found, identified by Miyoshi et al., 2010 as Reelin-negative/VIP-negative CGE-derived cells, confirming that the cells studied were Reelin-positive or VIP-positive interneurons.

Non-delayed cells consisted of bNA2 cells (5/15) or cells that could not be unambiguously identified following the scheme of Miyoshi et al., 2010 (10/15), but shared characteristics with dNFS3, irregular spiking (IS) or bNA2 cells. In contrast to our previous study, non-delayed cells were mostly regular (14/15) by our definition (average coefficient of variation (CV) of interspike intervals <0.5, but here 0.17-0.41). The non-delayed bNA2 cells (5/15) could also be termed "mildly irregular" (maximum CV 0.45-1.2 and presence of an onset burst). The difference in regularity of non-delayed cells between our previous and the present study could be due to temperature differences, but also due to the selection criteria. The latter is also indicated by the morphological analysis: all analyzed cells were multipolar in the present study, whereas irregular spiking (IS) cells were bipolar in Miyoshi et al., 2010. "Subthreshold oscillation" (as qualitatively described for IS cells by Miyoshi et al., 2010) were not obvious anywhere. A few cells with non-delayed onset also showed pronounced spike height adaptation for suprathreshold currents and somewhat irregular firing for intermediate currents. However, their AHPs were more similar to dNFS3 cells, rather than small and round as described for IS cells. They did not have particularly fast spike kinetics or higher spike thresholds, and did not have a pronounced sag. They therefore are rather a non-delayed version of dNFS3 cells.

A few additional differences between the firing pattern profiles in the present study and Miyoshi et al., 2010 are probably due to regional differences between somatosensory cortex and hippocampus and/or temperature differences. Regarding input resistance and maximum firing frequency, the group of LS1 and LS2 interneurons were closer to LS2 in the present study (R_{in} = 159 MΩ, maximum frequency 39 Hz), although in 8/10 cells the delay persisted with multiple spikes as in LS1. The spike thresholds of dNFS3 cells were, in contrast to Miyoshi et al., 2010, not particularly low. This is in line with the general observation that in the present data sample spike thresholds were higher, spike widths smaller and input resistances smaller, as one would expect due to the higher temperature. The cells which I identified as bNA did not show a hump around threshold (and therefore are rather bNA2 than bNA1), but also look differently than the examples of bNA2 shown by Miyoshi et al., 2010. Since "bursts" are not clearly defined by Miyoshi et al., 2010 (see 2.4.2 for the definition applied here), some of the non-classified non-delayed cells with non-adapting firing pattern could potentially be bNA2 according to their classification.

Altogether, the firing profiles of GABAergic interneurons targeted in the study on Ca^{2+} inhibition were consistent with the firing profiles of Reelin- or VIP-positive CGE-derived interneurons as described by Miyoshi et al., 2010 and Wierenga et al., 2010. Differences in the detailed characteristics of subgroups indicate that firing patterns are sensitive to recording temperature and vary with brain region, while differences in the distribution of subgroups strongly indicate that a more homogeneous sample was targeted, which consisted of multipolar, regular-firing, dendrite-targeting, Reelin- or VIP-positive cells.

3.1.4 Methods for single-cell stimulation

Regarding the question how to stimulate individual GABAergic synaptic contacts, optogenetics or single-cell electrical stimulation were the two available methods. While single-cell electrical stimulation via a patch-clamp electrode is straightforward and comes close to the physiological situation by evoking somatic action-potentials with physiological waveform, it

also requires stable prolonged electrical access. Optogenetics on the other hand offers optical stimulation without the issues of electrode stability or interference with the intracellular milieu, and it allows the (simultaneous or successive) stimulation of multiple cells, thereby potentially increasing the success rate of finding synaptic connections. Yet, optically evoked action-potentials and postsynaptic responses differ from physiological waveforms (Schoenenberger et al., 2011), and the spatial selectivity of stimulation depends on expression sparseness as well as the point-spread function of the microscope. Moreover, optogenetics does not offer any control over stimulation success and AP onset jitter, for which electrical stimulation provides a clear readout.

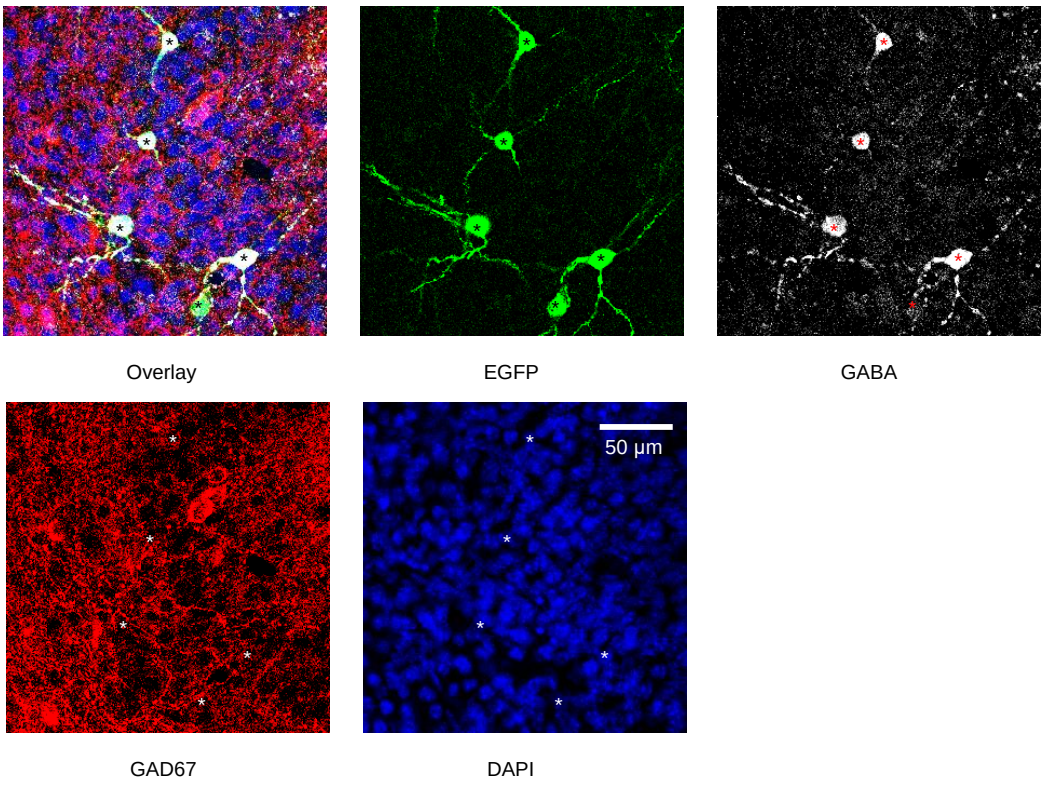

Figure 16: Immunohistochemistry of biolistically transfected cultures. Hippocampal slice cultures previously transfected with pmGAD67-EGFP were immunohistochemically labeled with antibodies against EGFP (green), GABA (white) and GAD67 (red), and nuclei were DAPI-stained (blue). Asterisks mark five EGFP-positive cells. While 4/5 cells were strongly and 1/5 weakly stained for GABA, GAD67 signals overlapped neither with EGFP nor with GABA (see Overlay), indicating poor antibody performance. Please note that the shown GABA- and GAD67- stainings are not representative, since signal-to-background levels were often considerably worse.

3.1.5 Targeting GABAergic interneurons by biolistic transfection

To conduct optogenetic stimulation in organotypic hippocampal slice cultures, biolistic transfection provided a straightforward method to achieve the required sparse transfection rate. Two plasmids containing promoter sequences for GAD65, respectively GAD67 (pmGAD65-lacZ, Kobayashi et al., 2003, and pmGAD67-lacZ, Makinae et al., 2000) were provided by courtesy of Dr. Yuchio Yanagawa, Japan. To mark GABAergic interneurons fluorescently, lacZ was replaced by EGFP using standard molecular biological techniques (2.3.2), and the resulting plasmids were partially DNA-sequenced. Hippocampal slice cultures were biolistically transfected with both constructs following standard procedures (McAllister, 2000, pressure

100-200 psi). Both constructs successfully targeted GABAergic interneurons as confirmed by GABA-immunohistochemistry. However, transfection rates were very low, with on average 0 and 5 EGFP-positive cells per culture (range 0-3, n=37 and 0-20, n=96) for the pmGAD65-EGFP respectively pmGAD67-EGFP plasmids.

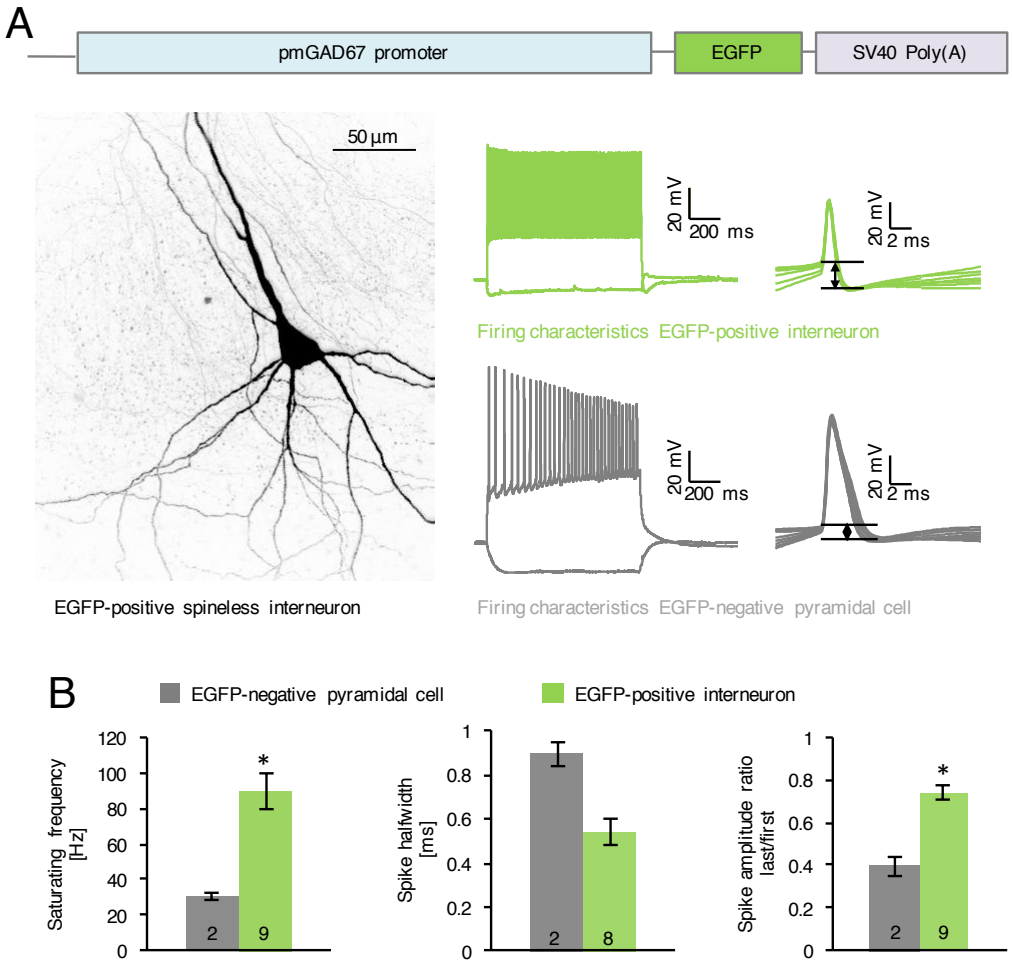

Figure 17: pmGAD67-EGFP transfects mainly fast-spiking GABAergic interneurons (A) Biolistic transfection with the pmGAD67-EGFP vector (schematized in the upper panel) resulted in preferential labeling of fast-spiking cells (saturating frequency >50 Hz, n=9/14, also see Fig. 2, left panel). Left panel: morphology of a fast-spiking interneuron (note the absence of dendritic spines and dense local axon arborization). Right panel, green: firing pattern and AP waveform of the shown EGFP-positive interneuron, gray: firing pattern and AP waveform of an EGFP-negative pyramidal cell. Arrows indicate afterhyperpolarization measured from spike-threshold. (B) Comparison of firing characteristics reveals that the fast firing interneurons (left panel, mean saturating frequency >80Hz, $p<0.05$) also display a shorter spike half-width (middle panel) and less amplitude adaptation, quantified by the ratio between first and last spike amplitude (right panel). p-values: Wilcoxon signed-rank.

Immunohistochemistry with GABA-antibody had a high background level, which did not permit quantifying the targeting-specificity and -selectivity in a rigorous manner, but ≥19/65 pmGAD67-EGFP-positive cells and ≥1/2 pmGAD65-EGFP-positive cells were also positive for GABA. Immunohistochemistry results with antibodies against GAD65 and GAD67 were inconclusive: while GAD65-antibody staining did not result in any specific labeling, GAD67-antibodies seemed to specifically label some cells, albeit with poor signal-to-background ratio,

but these did not overlap with pmGAD67-EGFP cells (0/67 EGFP-positive cells were GAD67-positive), and often not even with GABA (Fig. 16).

On the other hand, morphological and electrophysiological characterization EGFP-positive neurons in pmGAD67-EGFP transfected cultures confirmed that GABAergic interneurons were targeted: n=9/14 EGFP-positive cells were fast-spiking (saturating frequency >50H and narrow APs typical for fast-spiking interneurons, Fig. 17, some of them with clear basket-cell morphology as shown in Fig. 2), n=1 was irregular spiking, n=1 exhibited an accelerating firing pattern, n=1 exhibited a ramping firing pattern and the remaining n=2 had a regular, adapting firing pattern, but a clearly non-pyramidal, multipolar morphology.

Altogether, biolistic transfection with the pmGAD65 and pmGAD67 constructs offered a tool for sparsely targeting GABAergic cells in slice cultures. However, low transfection efficiency limited its usability, and cells counted as EGFP-positive could even have very low expression levels, especially for the pmGAD65 construct. Considering that channelrhodopsin-activation with 2-photon resolution needs an even larger excitation area than 1-photon activation (Oron et al., 2012), this approach did not appear promising for single-axon stimulation. Together with the caveats of altered synaptic transmission and uncontrolled AP failures/jitter which go along with the optogenetic approach, electrical stimulation by patch-clamp electrophysiology was ultimately the method of choice for stimulating individual GABAergic synapses.

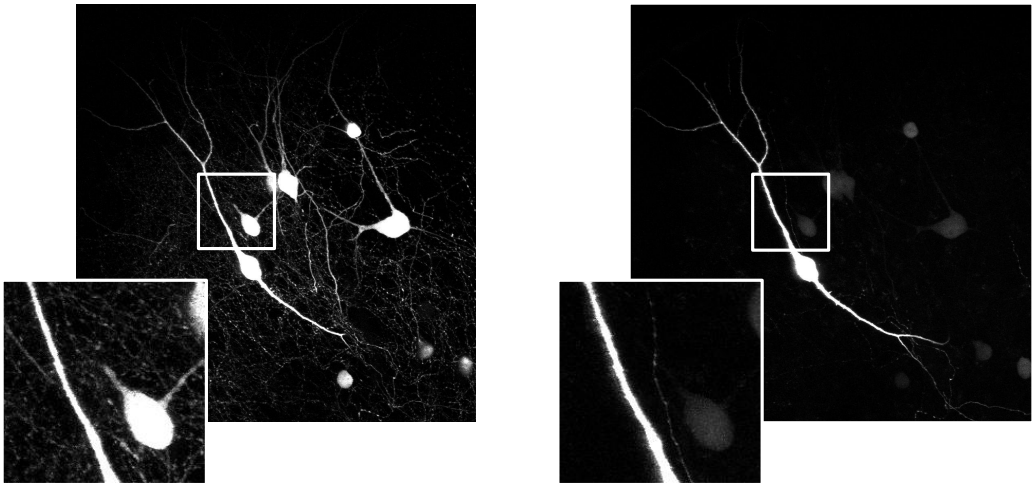

Figure 18: Double-dye filling and spectral separation strategy to visualize individual inhibitory axons In GAD65-EGFP slice cultures, the dense arborization of GFP-positive axons (left panel, imaged at 910 nm), together with the faint labeling of thin axon stretches, makes tracing of single axons back to the soma impossible. If, however, one of the interneurons is filled with an additional green fluorescent dye that is preferentially excited at lower wavelengths, its substructures and axon can be easily distinguished by spectral separation (right panel, imaged at 750 nm).

3.1.6 Identification of individual GABAergic axons

The usage of slices from GAD65-GFP mice allowed the identification of GABAergic interneuron somata based on GFP-expression. However, in order to unambiguously identify synaptic contacts made by the stimulated interneuron, the corresponding axon needed to be discriminated from other GFP-positive axons (Fig. 18, left panel). To achieve this goal, a double-labeling strategy was developed: via the patch-electrode, the GFP-expressing interneuron was filled with an additional green fluorescent dye (Calcein or Alexa 488). Since the additional

dye is preferentially excited at lower wavelengths, the targeted GFP-positive axon, which is indistinguishable at 910 nm imaging wavelength in 2PLSM, can be spectrally separated at 750 nm excitation (Fig. 18, right panel).

3.1.7 Readouts of inhibitory synapse function

Regarding the experimental readout, the function of individual dendritic GABAergic synapses is thought to comprise the following three aspects (see Fig. 3):

1. Inhibition of incoming excitatory synaptic input
2. Inhibition of backpropagating action-potentials
3. Inhibition/modulation of synaptic plasticity at nearby spines (resulting from 1 and 2)

Aspect 1 and 2 can be studied either on the level of membrane potential or intracellular Ca^{2+} levels, while aspect 3 can be studied by reading out changes in spine morphology as a correlate of synaptic plasticity (Matsuzaki et al., 2004). This latter aspect, which has direct implications for the role of inhibition in learning and memory, was chosen as a first approach to study individual inhibitory synapse function.

3.1.8 Mimicking excitatory synaptic input with intact inhibition

This approach required establishing an experimental paradigm to study inhibition of plasticity at individual dendritic spines. Previously established paradigms to induce plasticity at individual spines employed 2-photon uncaging of caged glutamate (1.11). However, caged-glutamates in their un-uncaged form dose-dependently block $GABA_A$-receptor mediated synaptic responses, and in particular, the most widely used caged MNI-glutamate blocks inhibition very efficiently (Fino et al., 2009). In order to establish a protocol for spine plasticity induction in which inhibition is preserved, an alternative caged glutamate (RuBi-glutamate, introduced by Fino et al., 2009) was tested. While 2.5 mM MNI-glutamate, a concentration commonly used for spine plasticity induction, completely suppressed miniature IPSCs, the alternative RuBi-glutamate largely preserved inhibition (Fig. 19) at a concentration sufficient to evoke excitatory synaptic responses in a physiological regime (300 μM). The comparison between uncaging evoked and spontaneous EPSCs also illustrates that the kinetics of uncaging evoked excitatory synaptic responses are, albeit a bit slower (Fig. 20), still close to the physiological situation, a goal which is not even closely achieved by GABA-uncaging as a means to stimulate inhibitory synaptic responses (see Kantevari et al., 2010, their Fig. 2).

3.1.9 A quality control for caged-glutamate

Establishing glutamate uncaging under near-physiological conditions was severely impeded by unexpected side-effects of the RuBi-glutamate compound. Despite immense efforts to avoid exposing the caged-glutamate solution to any stray light which could uncage the glutamate (see 2.3.6), some batches of RuBi-glutamate acted strongly excitatory on the network. When 1 mM RuBi-glutamate was puff-applied to the culture, a radical increase in spontaneous activity (both inhibitory and excitatory) could be observed (Fig. 21, upper panel). Puff application of 50 μM of free glutamate mimicked the effect regarding amplitude (Fig. 21, lower panels), reversal potential and sensitivity to DNQX (not shown), indicating that the increase was due to free glutamate in the solution and not a side-effect of the cage-compound itself.

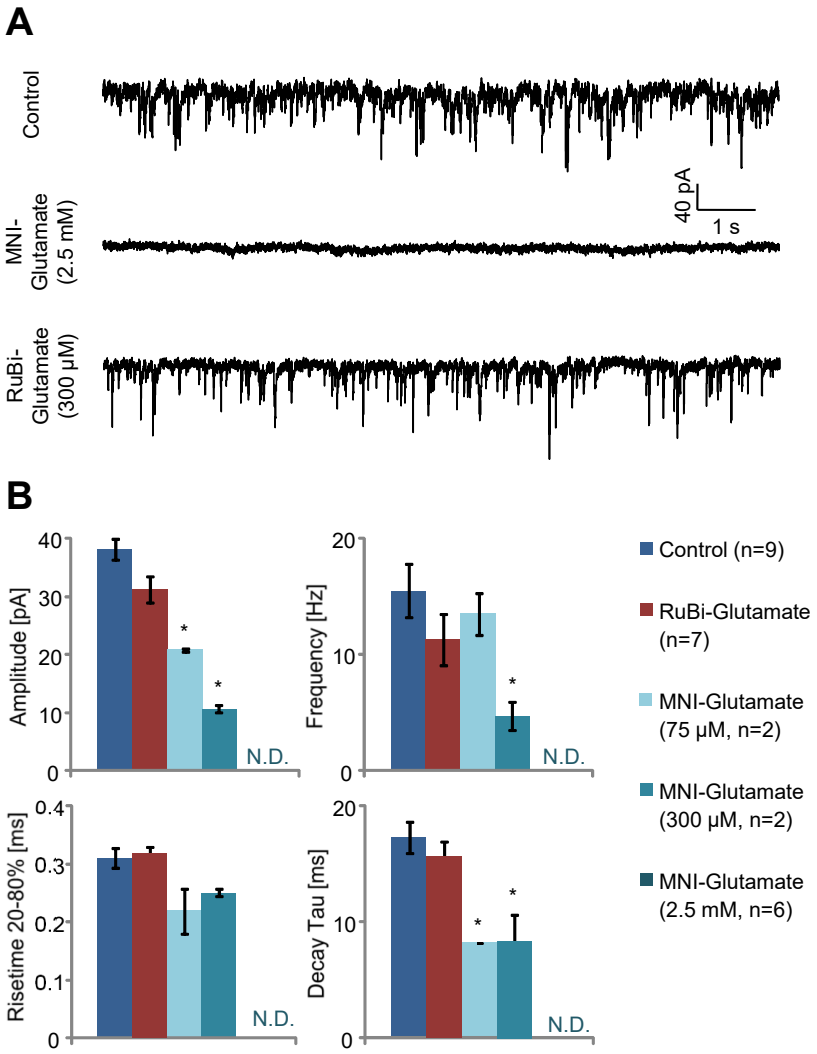

Figure 19: MNI-glutamate blocks GABAergic synaptic transmission (A) Miniature IPSCs which are frequent in control ACSF (upper panel) are fully blocked 2.5 mM MNI-glutamate (middle panel), but largely preserved in 300 μM RuBi-glutamate (lower panel). Recordings were performed in 10 μM DNQX, 20 μM D-AP5 and 0.5-1 μM TTX with CsCl internal at -70 mV holding potential to isolate mIPSCs. (B) Quantification of mIPSC amplitude, frequency and kinetics (20-80% risetime and monosynaptic decay time-constant) revealed that 300 μM RuBi-glutamate preserved inhibitory synaptic transmission in all aspects (amplitude reduction by 18%, n.s.), while MNI-glutamate dose-dependently reduced mIPSC amplitude, frequency and decay time-constant. See Fino et al., 2009 for equivalent effects on evoked inhibitory responses.

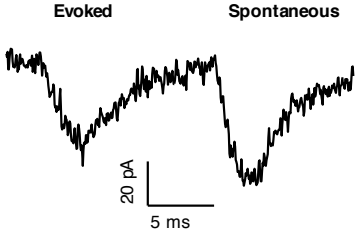

Figure 20: Glutamate-uncaging mimicks excitatory synaptic responses An uncaging evoked EPSC, followed by a spontaneous EPSC, confirm that the kinetics of uncaging evoked responses are close to the physiological situation (with slightly longer decay time-constant).

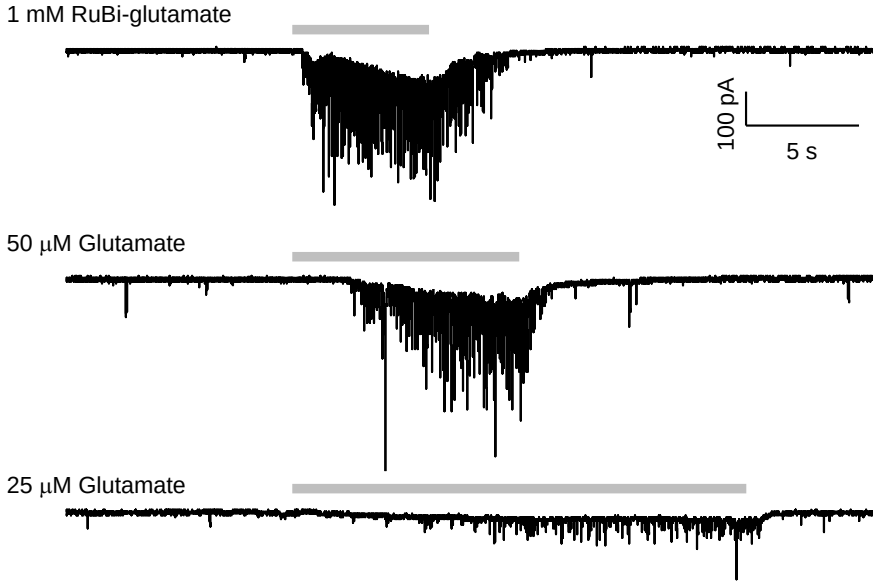

Figure 21: Side-effects of free glutamate Some batches of RuBi-glutamate strongly increased slice activity during puff-application (upper panel), comparable to the effect of 50 μM free glutamate (middle panel), while lower glutamate concentrations (25 μM, lower panel) caused considerably less activity (same cell in all panels).

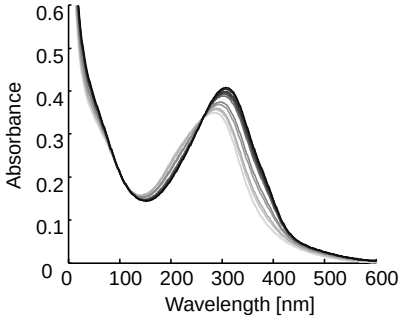

Figure 22: Quality control for caged glutamate by spectral analysis The absorption spectrum of a caged-glutamate solution exhibits a typical spectral rightward shift which can be used to determine the percentage of uncaged glutamate. Gray-levels indicate the degree of uncaging from presumably 0% (light gray) to 100% (black).

When bath-applied, network activity was in a more normal range, presumably due to compensatory/homeostatic processes. Still, excessive free glutamate could potentially have side-effects on synaptic transmission or plasticity. To overcome this problem, an essay was established to control the quality of the caged-glutamate prior to an experiment. Since the caged glutamate exhibits a spectral shift upon light exposure or pH change (Fig. 22), the free/uncaged glutamate content of every stock solution could be estimated based on its absorption spectrum. For calibration, a fresh solution (with presumably no free glutamate), and the same solution with fully uncaged glutamate after prolonged exposure to blue light were measured. Each sample was then fit by a linear model $f_1 \cdot A_0 + f_2 \cdot A_{100} = B$, where A_0 and A_{100} are the calibration spectra corresponding to 0 % and 100 % free glutamate, and B is the test spectrum. The relative content in free glutamate could then be estimated as $f_2 / (f_1 + f_2)$. And indeed, samples with strong excitatory side-effects contained 3.6–6.7% of free glutamate, while the other samples contained around 0 %. Value estimated down to -3.5 % could indicate variability in the baseline free glutamate content of fresh solutions. Measurement accuracy was about ± 1 %, as estimated by repeated measurements. Using this quality control essay, batches with especially low quality could be sorted out, and free glutamate in the solution was kept to a minimum (within the limits of measurement accuracy).

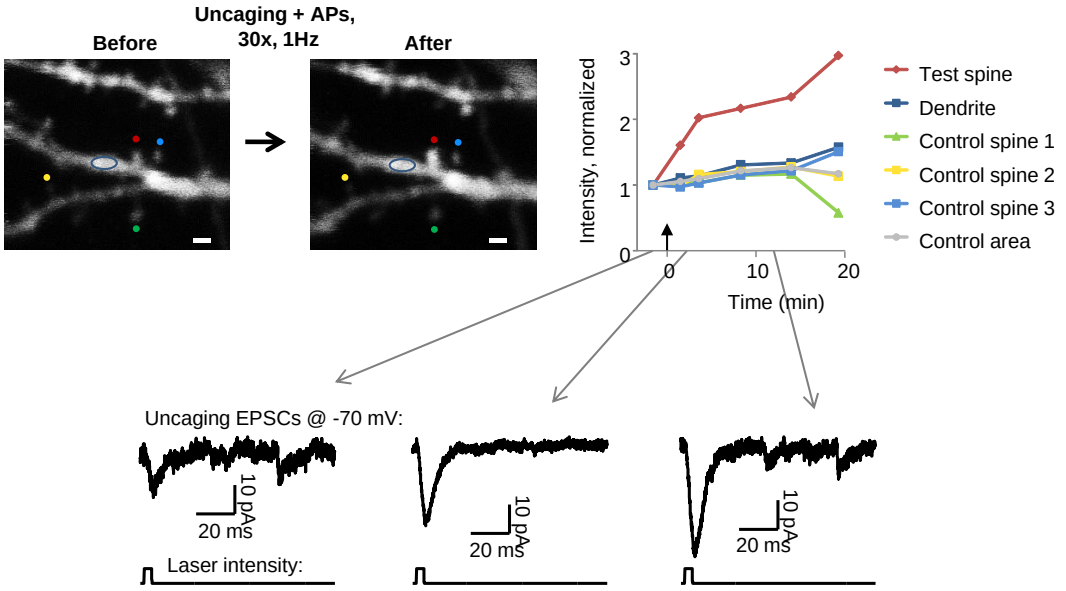

Figure 23: Pairing paradigm for inducing spike-timing dependent plasticity By pairing uncaging-evoked postsynaptic responses with backpropagating action-potentials (evoked by somatic current injection, 30x paired stimuli with 1 Hz), synaptic plasticity could be successfully induced, as indicated by the specific growth of the stimulated spine (upper panel, stimulated spine red) and the potentiation of the uncaging-evoked EPSC (lower panels). The upper right panel shows the quantification of spine volume, estimated by integrated intensity normalized to baseline, in the test spine (red), the dendritic shaft (dark blue) and neighboring control spine (yellow/green/light blue).

3.1.10 A paradigm for studying inhibition of synaptic plasticity

Potentially, two-color uncaging of glutamate and GABA would have been one approach to address the question how inhibition can modulate synaptic plasticity. However, on top of the insufficient temporal resolution, efficient GABA uncaging has only been achieved with 1-photon excitation, which together with the high abundance of extrasynaptic GABA-receptors limits its spatial scale and therefore the usability of GABA uncaging for mimicking inhibitory responses with synaptic resolution. For this reason, a paradigm was set up in which induction of spine plasticity could be combined with single-cell stimulation of APs to evoke physiological inhibitory synaptic responses. This precluded both the use of TTX and low magnesium conditions commonly used in spine plasticity paradigms, which would prevent, respectively alter synaptic GABA release. The method of choice was therefore a spike-timing dependent plasticity paradigm in which glutamate-uncaging is paired with postsynaptic action-potentials to relieve the magnesium blockade of NMDA receptors (Tanaka et al., 2008).

Indeed, repeated pairing of glutamate uncaging with APs could in several cases selectively induce growth of the stimulated spine, going along with a potentiation of the uncaging-evoked EPSC (Fig. 23). Spine growth was defined as an increase in summed fluorescence (3D-integral over a ROI covering the spine, see 2.4.6) with respect to control ROIs at the shaft. However, the overall outcomes of the plasticity induction paradigm were more variable than expected. To describe the different outcomes, 6 broad categories were defined based on quantitative and qualitative criteria, and each experiment was assigned to one category which matched the outcome best: (1) Growth, if the stimulated spine grew specifically, i.e. more than the neighboring spines and shaft; (2) Non-specific, if the stimulated spine as well as the neighboring spines and/or shaft showed an increase in intensity; (3) Retraction, if the stimulated spine shrank, retracted or moved away from the uncaging spot; (4) Toxicity, if branch blebbing,

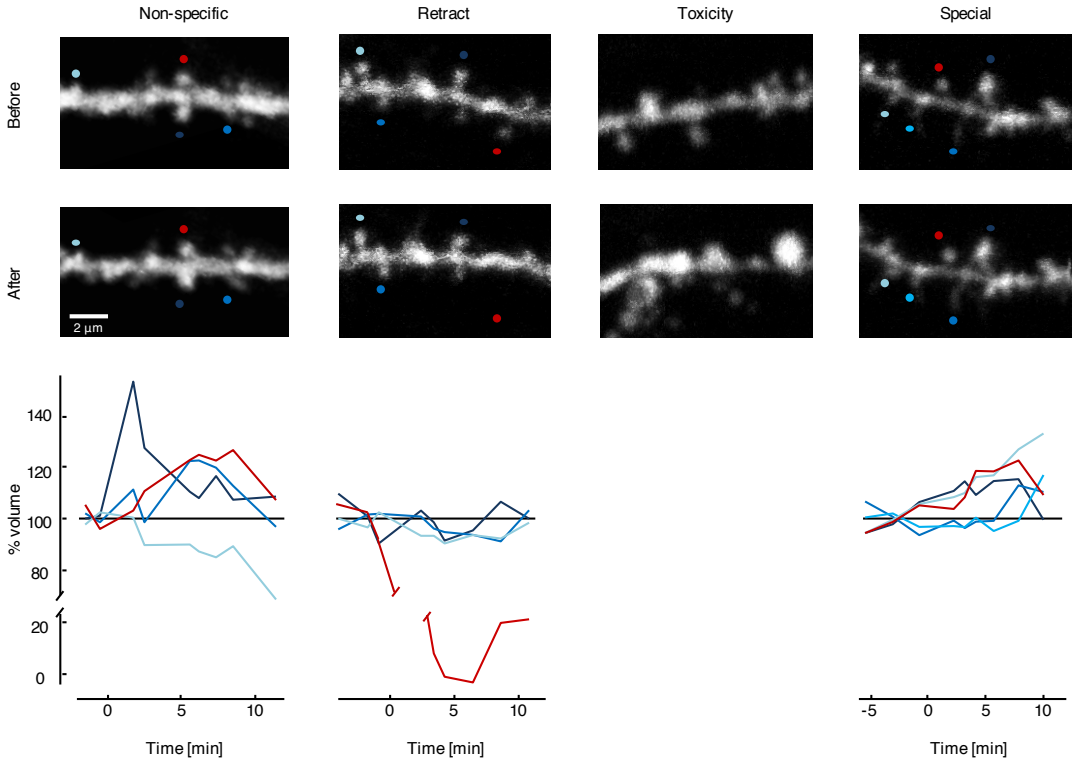

Figure 24: Alternative outcomes of the pairing paradigm In addition to specific spine growth, the following outcomes were frequently observed (upper panels, from left to right): (2) Non-specific growth, (3) Retractions, (4) Toxicity and (5) Special effects. Lower panels: quantification of % spine volume change in the test spine (red) or control spines (blue). In the "non-specific" example, test-spine volume increases by 20%, but also the volume of 2 out of 3 control spines increases. In the "retraction" example, the stimulated spine disappears, and its volume drops to zero accordingly. In the "toxicity" example, massive blebbing of the stimulated branch is observed and precludes the volume quantification. In the "special" example, the stimulated spine moves towards its neighboring spine.

strong swelling or dye leakage was observed, often going along with a depolarization of the cell; (5) Special, if the effect did not fall into one of the 4 standard categories, e.g. spine elongation without growth, spine broadening without growth, spine moving back and forth or moving along the shaft; (6) No effect, if no effect was observed. Examples for alternative outcome (2)-(5) are given in Fig. 24.

Applying a pairing paradigm with APs induced within 10-15 ms after the uncaging (as introduced by Tanaka et al., 2008), specific growth was induced only in 10% of the experiment, while toxicity and special effects predominated (Fig. 25 A). With a more closely spaced pairing of 0-10 ms, spine growth was successfully induced in 37.5% of experiments, whereas – as expected from the STDP framework – no growth was induced with APs preceding the uncaging by 0-10 ms.

Interestingly, the "washout" of plasticity was not as severe as expected, since spine growth could still be successfully induced after >60 minutes in the whole-cell configuration. Yet, the ratio of successful growth induction decreased slightly over time, which could be prevented by including β-actin (5 μM, adds 0.1 mM TrisHCl, 4.3 μM $CaCl_2$, 4.3 μM ATP, 0.02% (w/v) dextran and 0.1% (w/v) sucrose) in the pipette solution as suggested by Tanaka et al., 2008 (Fig. 25 B). Notably, culture age had an influence on the success rate, since spine growth was rarely induced in slices cultured for more than 3 weeks (Fig. 25 C). While plasticity induction

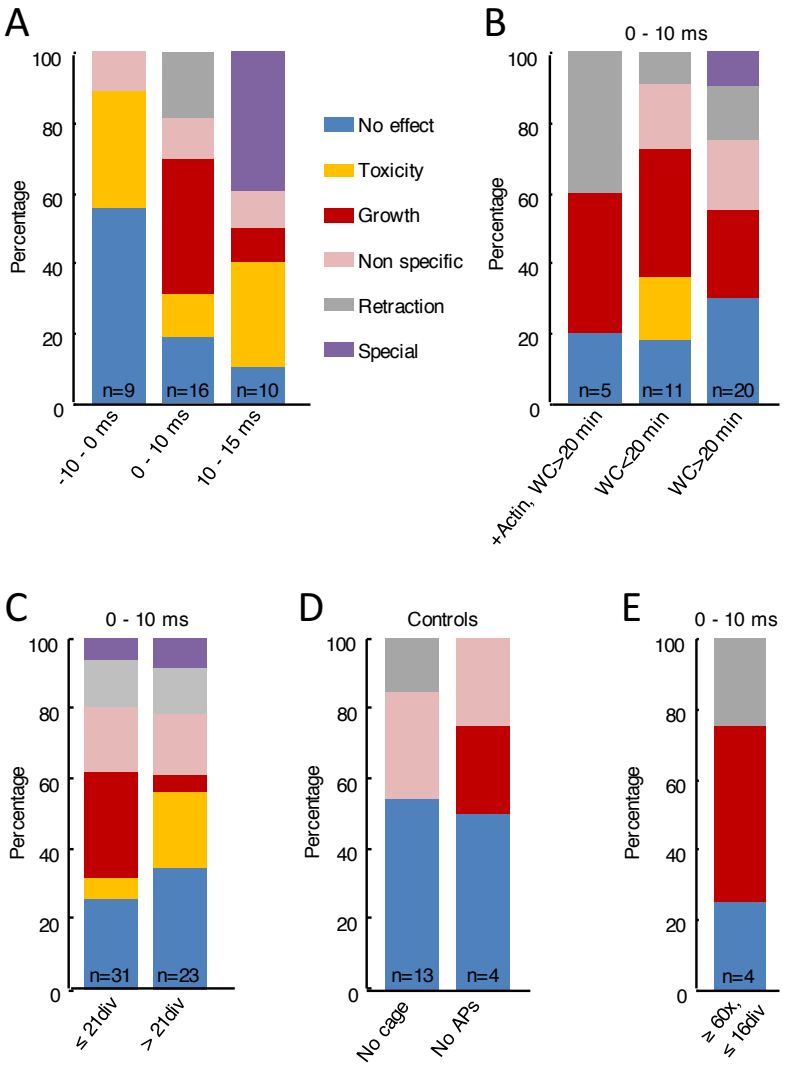

Figure 25: Outcomes of the pairing paradigm are variable and depend on culture age Plasticity outcomes were classified as described in Fig. 24. (A) Spine growth was, as expected, spike-timing dependent and required the backpropagating AP to follow the EPSP within 10 ms. (B) Spine growth was successfully induced in 36% of trials in the first 20 minutes of whole-cell configuration, if actin was substituted in >20 min recordings, but also in 25% of trial with >20 min of whole-cell configuration without actin-substitution, indicating that washout was only a minor issue. (C) Spine growth was nearly absent in cultures older than 21 div. (D) Under control conditions with laser pulses of comparable intensity, no plasticity was induced in the absence of caged glutamate (left bar). However, spine growth could be induced by glutamate uncaging without APs (1 out of n=4, right bar). (D) Under optimal conditions (cultures of 16 div or younger, at least 60 paired pulses, APs within 10 ms) spine growth could be induced in half the trials.

was not a side effect of laser-stimulation (no growth induced by stimulation without caged glutamate present, Fig. 25 D), unpaired uncaging without APs could also rarely induce spine growth (n=1/4, Fig. 25 D). Under optimal stimulation conditions (young cultures $\leq$16 div and stimulation with $\geq$60 repetitions, Fig. 25 E), successful growth induction could reach levels around 50%. However, slice cultures are in the process of maturation during the first 16 days is culture and connectivity levels continue to increase (Muller et al., 1993), which means one needs to compromise between efficiency of the spine plasticity paradigm and maturity of

the network.

Altogether, the variability of experimental observations following plasticity induction exemplifies that a more than 1-dimensional analysis could be necessary in this experimental framework. Moreover, reducing the experimental readout to the canonical dimensions of spine volume is considerably impeded by movements, especially by spine retractions which obscure the border between spine and shaft. Studying potentially subtle modulation by inhibitory synaptic input in this experimental framework presents additional challenges. As described below, finding putative inhibitory synaptic contacts requires several hours of experimental preparation, and at this stage there was no information available from either theory or experiment to decide (1) which morphological contacts between inhibitory axon and pyramidal cell dendrites would carry synapses, and (2) which timing of the inhibitory input would be necessary to modulate plasticity. Together with the variability of the outcome, an incalculable large number of experiments would have been needed to detect an effect.

3.1.11 A paradigm for studying inhibition of dendritic Ca^{2+} signals

Altogether, the avenue towards studying inhibition of synaptic plasticity seemed impassable at this point, and several important, more basic questions had arisen which demanded looking directly at Ca^{2+} signals as the common underlying mechanism of different forms of synaptic plasticity (Sjöström and Nelson, 2002):

1. How can one identify functional inhibitory synaptic contacts?
2. What is the impact of individual GABAergic synapses on dendritic calcium?
3. Are there spatial restrictions for Ca^{2+} inhibition by individual synapses?
4. What is the optimal timing of the inhibitory synaptic input?

To address these questions, a paradigm was developed combining 2-photon Ca^{2+} imaging and paired patch-clamp recordings between a GABAergic interneuron and a CA1 pyramidal cell. Dendritic Ca^{2+} transients were evoked by backpropagating action-potentials in the pyramidal cell which were paired with inhibitory synaptic input in every second trial. 2-photon Ca^{2+} imaging line scans in the vicinity of putative inhibitory synapses enabled quantifying local changes in the Ca^{2+} signal caused by the inhibitory synaptic input.

To identify putative inhibitory synapses, paired patch-clamp recordings between an inhibitory interneuron and a nearby pyramidal cell (target region CA1) were first selected if an inhibitory postsynaptic current (IPSC) was detected in the pyramidal cell (connectivity probability was ∼60%). Subsequently, the dendritic tree (∼600 μm along the somatodendritic axis) of the pyramidal cell was screened by 2-photon imaging for axodendritic contacts, some of which must carry the inhibitory synapses which mediated the IPSC. On average 10±5 putative axodendritic contacts (mean ± SD) were mapped.

3.1.12 Quantification of contact area

To quantify the contact size of axo-dendritic proximities detected by 2-photon imaging, a rigorous and unbiased quantification was developed, which estimates the 2D contact area between axon and dendrite by integrating voxel surfaces (see 2.4.8). In comparison to the quantification of 3D voxel overlap, 2D area is the more accurate estimate, both in the super-resolution and in the sub-resolution regime:

1. Even for moderately super-resolution structures (1 μm width in 2D), directly adjacent structures will result in voxel overlap only with ∼15% probability (simulation estimate).

Therefore, voxel overlap would actually underestimate the contact between the two structures. In 3D, things are slightly more complicated due to the asymmetry of the point-spread function. If the contact area is perpendicular to the z-axis, the standard-deviation of the point-spread function along z determines the overlap, and this problem only occurs for very large structures (super-resolution with respect to the z-resolution). If, however, the contact area is parallel to z, only the xy standard deviation matters, and even for moderately super-resolution structures with ∼1 μm radius, voxel overlap will likely be zero although they are directly adjacent. For oblique areas, overlap will be in between the two extremes. But altogether, imaging two neighboring super-resolution structures will not always result in voxel overlap. In contrast, voxel surface area will (apart from the cubic approximation error) correctly report the contact area between super-resolution structures, independent of their orientation in space.

2. The smaller two adjacent structures become, the more their contact will be overestimated. If one overestimates the structure radius by F due to the diffraction limit, the voxel overlap will scale with F^3, while the voxel surface area will only scale with F^2. That means, quantifying voxel surface area reduces errors due to diffraction limits by one order of magnitude for sub-resolution structures. In a very realistic scenario, in which the contacted dendritic shaft is super-resolution and the contacting bouton is sub-resolution, the contact area scales, due to the diffraction-limited overestimation, with the distance between the two structure centers. So even in a diffraction-limited regime, contact area will reflect proximity of the structures. Altogether, contact area proved to be, despite its diffraction limitation, a valid proxy for synapse functionality (see functional imaging Fig. 32 A+D and electron microscopic (EM) data Fig. 30).

3.1.13 Choice of Ca^{2+} indicator

To determine which Ca^{2+} indicator would be suitable for measuring dendritic Ca^{2+} inhibition, the Ca^{2+} response to backpropagating action-potentials with increasing frequency was measured in pyramidal cell dendrites. With 50 μM Oregon Green BAPTA-1 (OGB1, K_d = 210 nM, Fig. 26 A, see Yasuda et al., 2004 for K_d estimates), action-potentials were clearly detectable, but the Ca^{2+} response readily saturated the indicator even with single action-potentials. Therefore, the indicator Fluo5F with lower Ca^{2+} affinity (K_d = 1.3 μM) was chosen, for which single action-potentials are also readily detectable (orange traces in Fig. 26 B-E), but the Ca^{2+} response is in the linear range, even if triple action-potentials are applied for improved SNR (gray line in Fig. 26 B-F). With an even lower-affinity indicator Fluo4FF (K_d = 8.1 μM), dendritic Ca^{2+} transients were hardly detectable. Fluo5F is not saturated up to 200 Hz sustained firing frequency and 40% $\Delta G/R$ (Fig. 26 B-C). An apparent saturation of $\Delta G/R$ in dendrites does not necessarily reflect indicator-saturation, but can also reflect AP failures at high sustained frequencies (Fig. 26 D). Moreover, saturation in further distal dendrites can also reflect that action-potential amplitude and concomitant Ca^{2+} influx decrease along the dendrites (Gasparini et al., 2007). Finally, in distal dendrites, Ca^{2+} transients can be more transient, even to sustained input (Fig. 26 E), or show an extreme non-linearity, in which only strong sustained firing can elicit any Ca^{2+} response (Fig. 26 F). Taken together, 200 μM Fluo5F proved to be a good Ca^{2+} indicator for measuring dendritic backpropagating action-potentials over a large linear range up to ∼50% $\Delta G/R$ (Fig. 26 C), which sufficiently covers the range of dendritic Ca^{2+} transients upon stimulation with triple action-potentials (up to 35% $\Delta G/R$ see Fig. 34 A-B).

3.1.14 Stable long-term stimulation of inhibitory synapses

To avoid induction of inhibitory plasticity, interneurons were stimulated with ≤0.1 Hz. Since screening of the dendritic tree for inhibitory contacts and testing Ca^{2+} inhibition was time-

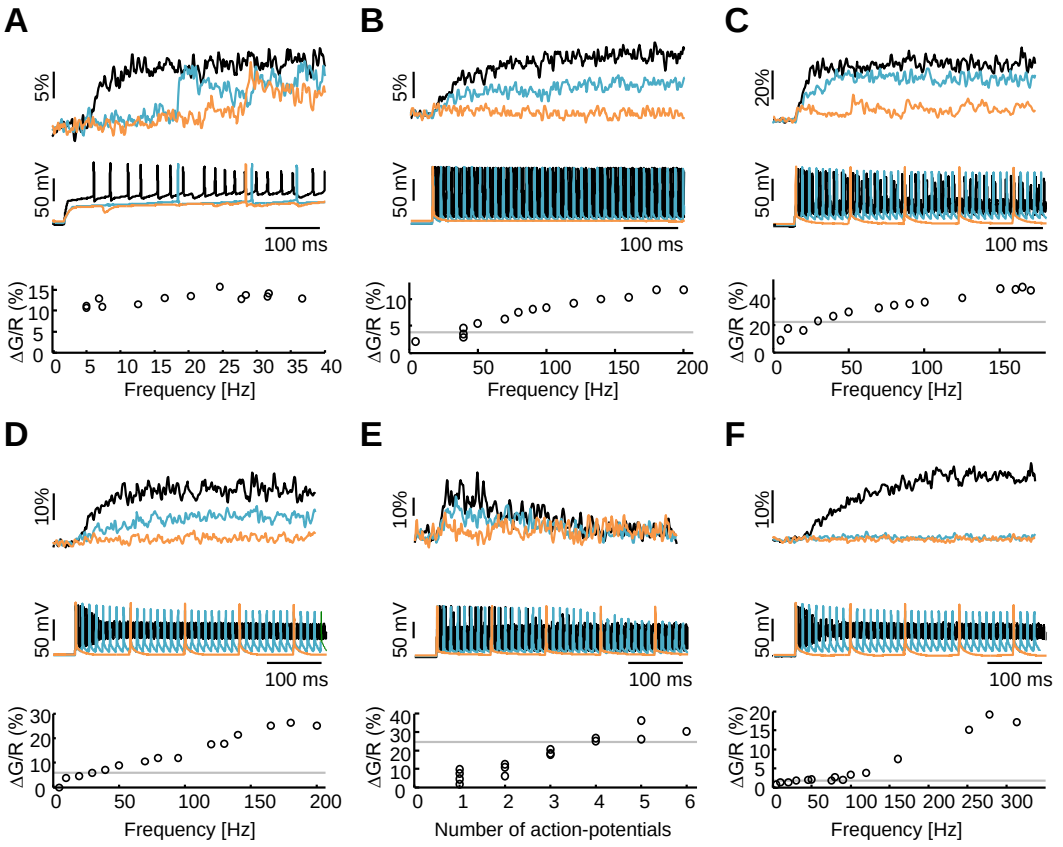

Figure 26: Ca^{2+} indicator calibration at dendrites (A-F) Ca^{2+} transients in pyramidal cell dendrites (upper panels) were measured in response to action-potential firing (middle panels) upon somatic current injection. To estimate the dynamic range of the Ca^{2+} indicator (lower panels), Ca^{2+} amplitude (% ΔG/R) is plotted relative to the firing frequency, both detected within 200 ms after the first AP (A-D,F) or Ca^{2+} amplitude is plotted relative to the number of action-potentials (E), both detected within 25 ms after the first AP. Pyramidal cells were filled with (A) 50 μM OGB1 + 20 μM Alexa 468, (B-E) 200 μM Fluo-5F + 30 μM Alexa 594, or (F) 400 μM Fluo-5F + 30 μM Alexa 594. Note the larger dynamic range, but also the faster kinetics of the Fluo-5F indicator.

consuming, experiments could span several hours (up to 4 hours). To ensure that inhibitory synapses were fully functional over this time period, IPSC amplitudes were tracked over the time-course of every experiment (see below for series resistance corrections). In a separate set of experiments, the stability of IPSC amplitudes during long-term recordings was examined. As described previously (Bouhours et al., 2011), IPSCs exhibit a temporary increase in amplitude ("run-up") within the first few minutes (Fig. 7 A), followed by a relaxation of amplitude, and finally a run-down over longer time-scales. As one strategy to potentially prevent run-down, cell-attached stimulations were established in which an intact membrane patch separates the intracellular milieu from the pipette solution. While run-up was still present with cell-attached stimulation, run-down seemed to be reduced. However, long-term cell-attached stimulation proved to be extremely difficult to achieve, since stability of the seal (especially in loose-patch configurations) and/or the membrane patch (especially in tight-patch configurations) degraded over time. Postsynaptic cell-attached stimulation comes with the additional disadvantage that IPSC amplitudes and failures cannot be controlled. Therefore, whole-cell stimulation with intermittent IPSC control measurements was ultimately the method of choice for long-term inhibitory synapse stimulation. Run-down of IPSC amplitudes was

alleviated by using small pipettes (series resistance 20.3 ± 8.1 MΩ, mean ± SD, average SD = 2.3 MΩ) and including GABA in the presynaptic internal solution (Bouhours et al., 2011). In a subset of experiments, washout was further prevented by retracting the pipette with GΩ-seal after filling the cell for 15-20 minutes, and by repatching the cell (without change in membrane potential, -0.3 ± 0.6 mV difference, mean ± SEM, n = 54) after the excessive screening of the dendritic tree for synaptic contacts. Run-up, on the other hand, was robust. It was also present with hyperpolarizing instead of depolarizing pulses and without GTP in the internal solution. Moreover, run-up was not due to chloride diffusion, leaving the question open whether run-up is due to a (very sensitive) stimulation-dependent process and/or induced by any missing or excessive component in the intracellular solution. IPSC baseline was therefore defined as the short period immediately after going whole-cell or as the steady-state after initial increase and relaxation. To ensure functionality of inhibitory synaptic transmission, IPSC amplitudes were tracked over the time-course of each experiment, run-down was defined as a decrease of IPSCs below the 95% prediction interval of baseline mean ±1.96 SD for more than 2 minutes, and trials recorded during or after run-down were discarded.

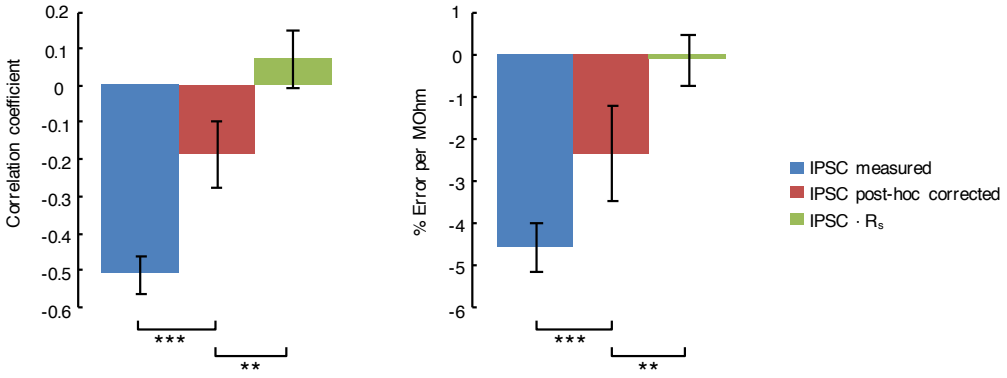

Figure 27: Post-hoc series-resistance compensation. The relationship between IPSC amplitude and series resistance (mean ± SEM) was quantified by Pearson correlation coefficients (left panel) and percentage of error per MΩ (estimated by linear regression, right panel). Both parameters were compared between uncorrected IPSC amplitudes (blue), IPSC amplitudes after standard post-hoc series-resistance correction (red), and measured IPSC amplitudes multiplied with series-resistance values IPSC x Rs (green). For estimating the relationship between IPSC amplitude and series resistance, datasets were taken as a reference for which series resistance varied strongly within 20 minutes of IPSC recordings (coefficient of variation ≥15 after filtering). Results of Wilcoxon signed-rank test indicated: *** for $p < 0.001$, ** for $p < 0.01$, n = 18 in N = 17 cells.

3.1.15 Series resistance correction for dendritic inhibitory inputs

Tracking IPSC amplitudes over hours required correction of amplitudes for changes in series resistance (R_s). To avoid the risk of feedback oscillations which can disrupt the recording, online compensation can only achieve ∼80% compensation at 4 kHz. Furthermore, it decreases SNR, is sensitive to unnoticed changes in series resistance during compensation, and uncompensated signals cannot be recovered. Post-hoc correction on the other hand is achievable (Traynelis, 1998 and APPENDIX I), but still limited by estimation errors, e.g. of input resistance. Online as well as posthoc correction are limited by the approximation errors of assuming a one-compartmental circuit, by estimation errors of membrane capacitance and series resistance, and by the trade-off in filter selection between achieving maximal compensation or preserving SNR (for which one workaround is presented in APPENDIX I).

To quantify how IPSC amplitudes depend on series resistance, IPSC amplitudes (I_{peak}) and R_s were recorded with conditions under which R_s varied strongly within a short time-interval

(20 minutes, coefficient of variation ≥ 0.15 after applying a running average filter of width 5), e.g. by retracting the pipette. For the given dataset with IPSCs of mostly dendritic origin, the relationship between IPSC amplitudes and series resistance could be roughly described by $1/R_s$, and therefore a reasonable compensation for R_s was given by multiplying R_s and I_{peak} (remaining correlation between I_{peak} and R_s: Pearson $R = 0.07 \pm 0.08$, remaining IPSC change per MΩ: $0.1\% \pm 0.6\ \%$, mean $\pm$ SEM). This empirically found relationship was revisited in a theoretical context (see APPENDIX II) and used as a posthoc correction for the full IPSC dataset: $I_{corrected} = I_{peak} \times R_s / 10$ MΩ, corresponding to IPSC amplitudes at 10 MΩ series resistance.

3.2 INHIBITION OF DENDRITIC CA^{2+} TRANSIENTS BY INDIVIDUAL GABAERGIC SYNAPSES

The following chapter has been adapted with minor modifications from:

Müllner FE, Wierenga CJ, Bonhoeffer T (2015) *Precision of inhibition: Dendritic inhibition by individual GABAergic synapses on hippocampal pyramidal cells is confined in space and time*, Neuron 87:576–89.

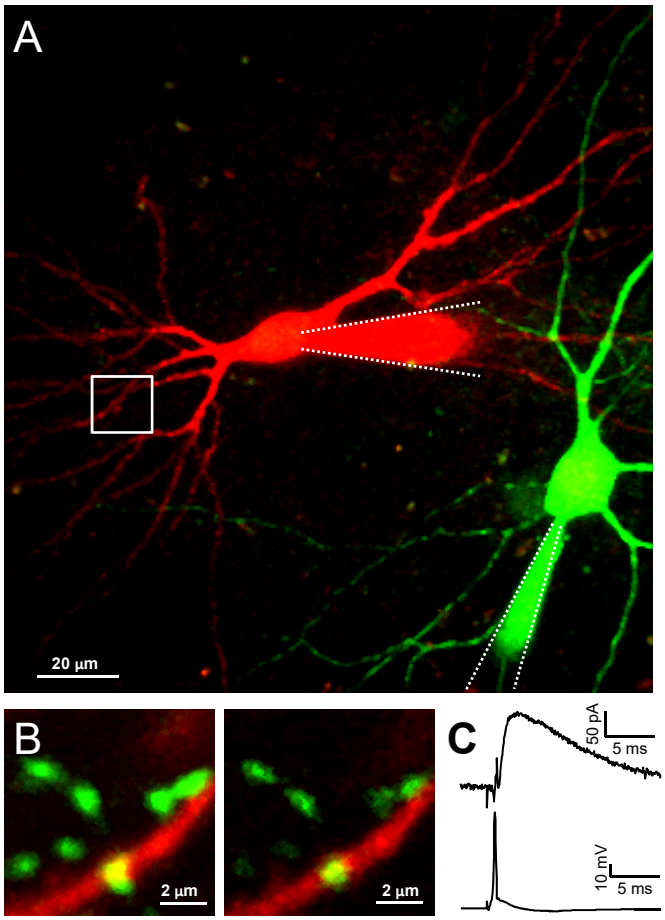

Figure 28: Recording configuration. (A) GAD65-GFP positive interneuron (200 μM Alexa488 filled, green) and pyramidal cell (30 μM Alexa594 and 200 μM Fluo5F filled, red). Dotted lines contour patch-pipettes. (B) Zoom-in to boxed area in (A): Morphological contact between the axon (green) and dendrite (red) indicates a putative inhibitory synapse (2PLSM image, left: maximum projection, right: single z-plane). (C) IPSC recorded in the pyramidal cell voltage-clamped at -40 mV (upper panel), following an AP in the inhibitory interneuron (lower panel).

3.2.1 Individual GABAergic synaptic contacts inhibit dendritic Ca^{2+} transients

In order to quantify the impact of individual GABAergic dendritic shaft synapses on local Ca^{2+} transients, I performed paired patch-clamp recordings from GABAergic interneurons and nearby pyramidal cells in organotypic hippocampal slice cultures prepared from GAD65-GFP mice (López-Bendito et al., 2004). Here I took advantage of the strong GFP expression in a subset of mostly dendrite-targeting GABAergic interneurons (Wierenga et

al., 2010). A GFP-positive interneuron with its soma in stratum radiatum/oriens or at the border to stratum pyramidale and a nearby pyramidal cell were patched simultaneously (Fig. 28 A). I visually confirmed that the interneuron axon contacted the pyramidal cell dendrites (Fig. 28 B). I additionally checked whether the axon also contacted the soma and found that ∼80% of the interneurons did not make contacts with the cell body; in the remaining ∼20%, one axon branch contacted the soma with 1-3 boutons, but never in a basket-like fashion. Action-potentials (APs) in both cells were elicited by somatic current injection. Whenever interneuron stimulation elicited a unitary IPSC in the voltage-clamped pyramidal cell, it was taken as evidence for a direct synaptic connection (Fig. 28 C connection probability ∼60 %, IPSC amplitude 5-400 pA at -40 mV, latency 1.6 ± 0.6 ms; mean ± SD). Unitary IPSC kinetics were (without exception) intermediately fast (range of halfwidths 3.5 – 13.1 ms at 40 mV, 34°C, see Fig. 28 C and Table 1), with negative correlations between amplitude and kinetics (Spearman rank correlations with $p < 0.05$), confirming that IPSCs were of dendritic origin and e.g. neurogliaform cells were not targeted. Morphological and electrophysiological analysis revealed that the selected interneurons (n = 50) were multipolar (36 of 36 morphologically analyzed interneurons) and displayed regular firing patterns with moderate frequency and/or amplitude adaptation (Fig. 15 A, n = 46 (middle panel), including 12 of the 50 interneurons (right panel) and 34 equivalently targeted interneurons with detected IPSCs). The firing profiles are consistent with previous reports for VIP- or Reelin-positive CGE-derived interneurons (Miyoshi et al., 2010; Wierenga et al., 2010) and consist of ∼50% delayed and (moderately) fast-spiking (20/21 dNSF3), ∼20% delayed and regular-spiking (9/10 LS1/2), and ∼30% non-delayed, mostly regular-spiking interneurons (5/15 bNA2) (Fig. 15 B). Reversal potentials were well within the physiological range, as confirmed by gramicidin perforated-patch recordings (Fig. 29, -69.6 ± 1.5 mV vs. 71.4 ± 1.2 mV at 24°C and 74.1 ± 2.2 mV vs. -75.3 ± 2.1 mV at 34°C in whole-cell vs. perforated, mean ± SEM, differences not significant, n = 9/11/7/5), and stable during whole-cell recordings of the cells (Fig. 7). In summary, the inhibitory interneurons studied were multipolar, regular-firing, most likely Reelin or VIP-positive cells.

	Halfwidth [ms]	*Risetime 10-90% [ms]*	*Decay tau (mono-exp.) [ms]*	*Delay [ms]*	*N*
IPSCs at -100mV, no R_S correction (mean R_S=16 MΩ)	6.2 ± 0.7 [3.0,11.4]	1.2 ± 0.1 [0.5,1.8]	6.1 ± 0.7 [2.3,11.9]	1.7 ± 0.1 [1.0,2.2]	12
IPSCs at -40mV, no R_S correction (mean R_S=16 MΩ)	9.7 ± 0.4 [3.8,24.0]	2.2 ± 0.1 [0.6,5.7]	9.0 ± 0.4 [4.3,20.3]	1.9 ± 0.1 [0.9,5.3]	71-72
IPSCs at -100mV, R_S online compensated ~80%, 4kHz	5.7	0.8	5.8	1.3	1
IPSCs at -40mV, R_S online compensated ~80%, 4kHz	7.5 ± 0.5 [3.5,13.1]	1.5 ± 0.2 [0.5,3.0]	8.3 ± 0.6 [4.0,15.4]	1.6 ± 0.1 [0.5,3.4]	22-23

Table 1: IPSC kinetics. The kinetics of IPSCs with and without series resistance compensation are displayed as mean ± SEM and range [minimum, maximum]. To determine the 10-90% risetime and the synaptic delay (with reference to the AP kink), the IPSC rise was fitted with a monoexponential function. R_s: series resistance.

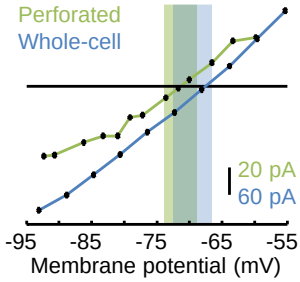

Figure 29: Reversal potentials are in the physiological range. Representative IV-curves for perforated-patch and whole-cell recordings. The overlapping blue and green bars represent the respective 95% confidence intervals of mean reversal potential at 24°C.

3.2.2 Structure-function correlation

To identify putative inhibitory synaptic contacts, I exhaustively screened a major part of the dendritic tree (~600 μm along the somatodendritic axis) by 2-photon laser scanning microscopy (2PLSM) for morphological contacts between the inhibitory axon and the pyramidal cell dendrite (Fig. 28 B, 10 ± 5 putative contacts mapped, mean ± SD). EM analysis showed that this procedure readily detects inhibitory synapses (Fig. 30 A) and that the probability of finding an inhibitory synapse at an identified contact depends on its 2PLSM axo-dendritic contact area (n = 6/26, Fig. 30 B). Once a putative axo-dendritic contact was identified, Ca^{2+} transients were evoked in the pyramidal-cell dendrite by backpropagating APs and measured locally by 2PLSM line scans (Fig. 31 A). I observed that the amplitude of Ca^{2+} transients could drop substantially when I simultaneously stimulated the interneuron. To quantify this inhibition, I compared Ca^{2+} transients evoked by simultaneous APs and IPSPs (ΔCa^{2+}_{inh}) with AP-evoked Ca^{2+} transients under control conditions (ΔCa^{2+}_{ctrl}, Fig. 31 B-C). I report Ca^{2+} inhibition as $inh = 1 - \Delta Ca^{2+}_{inh}/\Delta Ca^{2+}_{ctrl}$.

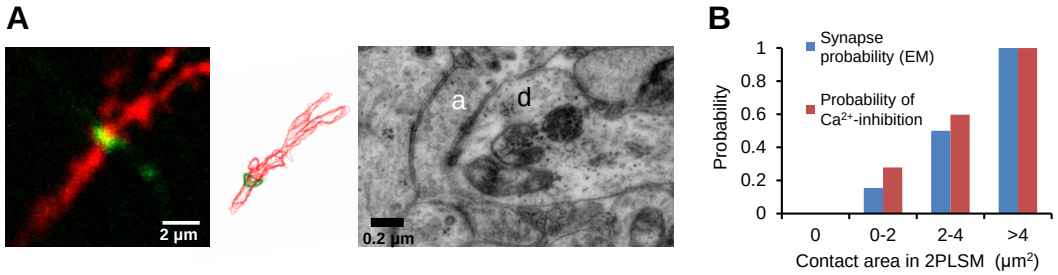

Figure 30: Ultrastructural correlates of putative inhibitory synapses. (A) Inhibitory synapse detected in 2PLSM (left), post-hoc verified in EM (right) and reconstructed (middle panel). a: axon (green), d: dendrite (red). (B) Comparison of the probability of finding an inhibitory synapse at a putative contact detected in 2PLSM (blue) and the probability of detecting significant Ca^{2+} inhibition at a contact (red), given its 2PLSM contact area.

Since single APs sometimes failed to evoke detectable Ca^{2+} transients in more distal dendrites, and in order to generally improve the signal-to-noise-ratio (SNR), I stimulated both cells with short bursts of three APs (5 ms interstimulus-interval). Significant Ca^{2+} inhibition ($p < 0.05$ sign-test) occurred in 58% of morphologically identified contacts with a contact area >1 μm^2 (n = 15 of 26, Fig. 31 D). For a given contact area, the probability of detecting significant Ca^{2+} inhibition was similar to the probability of finding a GABAergic synapse in EM (Fig. 30 B), indicating that I indeed measured synaptic inhibition. For each contact, the Ca^{2+} inhibition under optimal conditions (optimal spike-timing and distance from contact)

was quantified. Ca^{2+} inhibition varied largely and reached values up to 70% (representative traces for different inhibition levels shown in Fig. 31 C, F-G). With a median inhibition of 8.8% across all contacts (n = 38, Fig. 31 E), and 17.9% across contacts where inhibition reached significance (n = 17), Ca^{2+} transients were only modulated in amplitude, but not completely blocked.

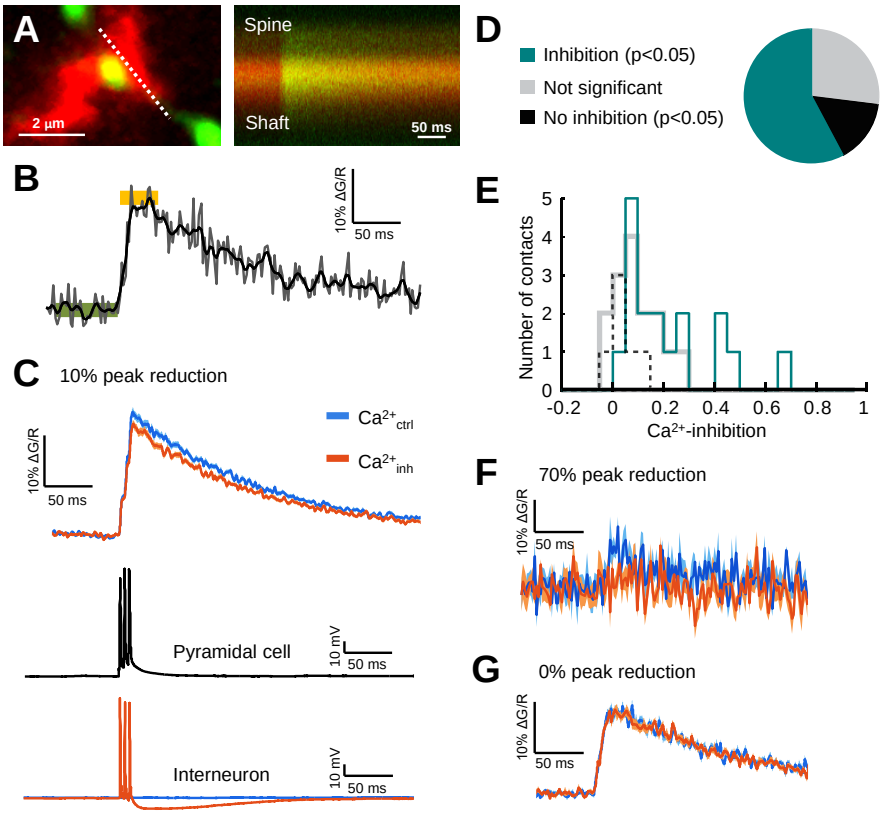

Figure 31: Ca^{2+} imaging of synaptic inhibition. (A) Left panel: 2PLSM image of a dendritic shaft and spine close to a putative inhibitory synapse (yellow); dotted line indicates line scan. Right panel: AP-evoked Ca^{2+} signal in the dendritic shaft and spine. (B-C) Ca^{2+} transients in the shaft shown in (A). (B) Single raw (gray) and Gaussian-filtered transient (50 Hz low-pass, black). Green bar: baseline, yellow bar: peak detection-region. (C) Upper panel: Average unfiltered transients (mean ± SEM), evoked by APs only (blue) or by simultaneous IPSPs + APs (orange). Lower panel: Corresponding spikes in the pyramidal cell (black) and interneuron (orange: AP, blue: no AP). (D) Proportion of contacts with area >1 μm^2 (n = 26) and (E) distribution of Ca^{2+} inhibition at all contacts (n = 38) for which significant inhibition, significant absence of inhibition (<5% reduction), or no significance was reported. (F-G) Ca^{2+} transients representative for strong inhibition (70%, F) and no inhibition (0%, G); mean ± SEM.

3.2.3 Ca^{2+} inhibition is determined by local factors

To characterize dendritic Ca^{2+} inhibition in more detail, I first asked what are the main determinants of Ca^{2+} inhibition. While local Ca^{2+} inhibition was highly correlated with axo-dendritic contact area (Pearson R = 0.76, $p < 0.001$, Fig. 32 A), it was only moderately correlated with the distance from the soma (Pearson R = 0.58, p = 0.005, Fig. 32 B), and completely uncorrelated with the somatically measured compound IPSC amplitude (Pearson R = -0.21, p = 0.33, Fig. 32 C), arguing against the possibility that the observed dendritic inhibition was due to a global interference of the compound IPSP with the AP or its backprop-

agation. Measurements from dendritic spines cross-validated the results: Ca^{2+} inhibition at dendritic spines also depended on contact area (Fig. 33 A), but not IPSC amplitude (Fig. 33 B).

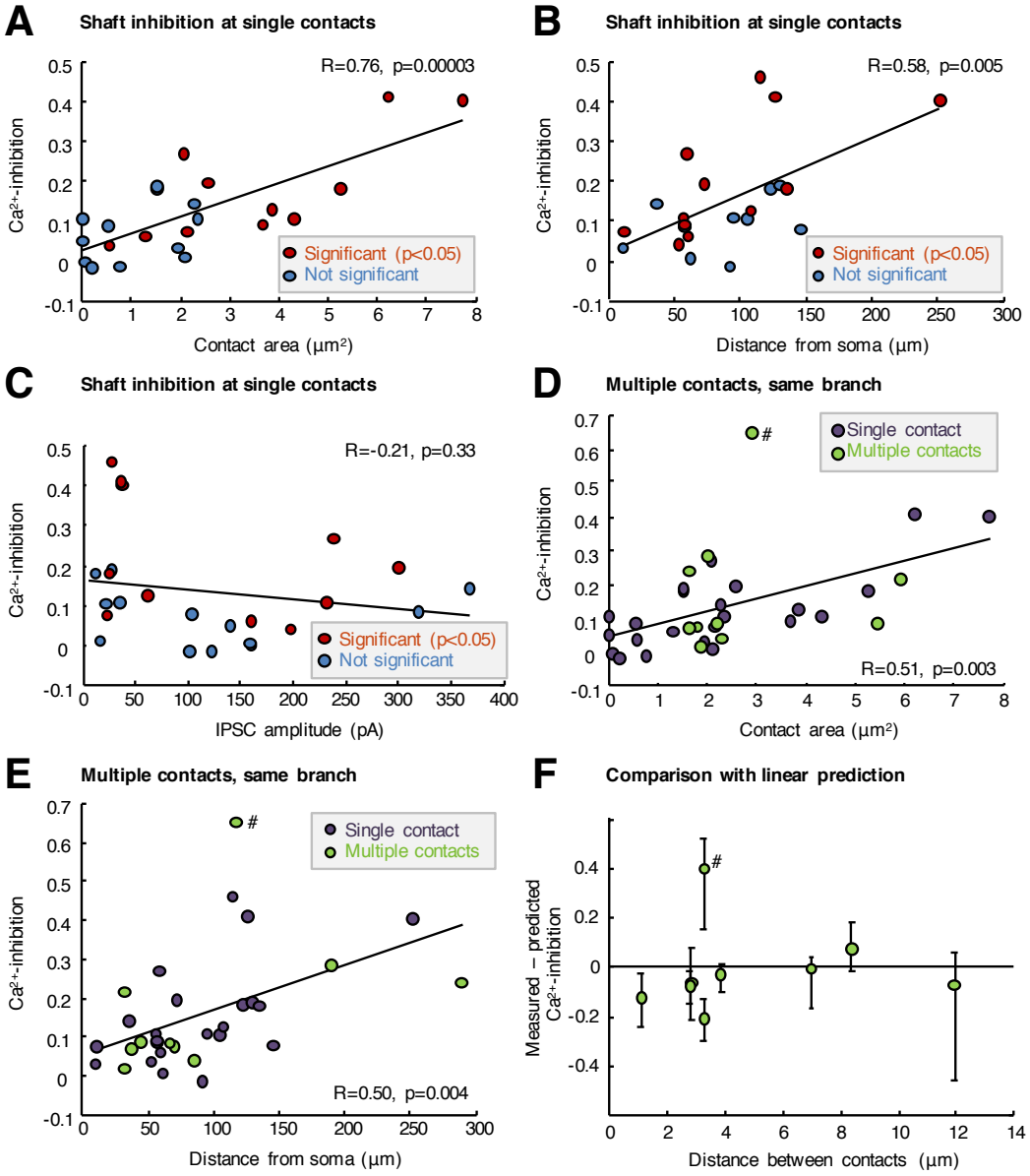

Figure 32: Ca^{2+} inhibition depends on contact area and distance from soma. (A-C) Ca^{2+} inhibition at dendritic shafts carrying single contacts plotted versus axo-dendritic contact area (A), versus distance between contact and soma (B), and versus somatic IPSC amplitude (C). Contacts with significant inhibition are labeled in red, all others in blue. Pearson R include all data to avoid bias; n = 22-24 contacts between n = 18 pairs. For the subset of significant data: R = 0.76, p = 0.007 (A) and R = 0.68, p = 0.01 (B).(D-E) Ca^{2+} inhibition recorded at branches carrying multiple contacts (green) is compared to the single contact data (purple) from (A-B); n = 32-33 contacts between n = 25 pairs. (F) Ca^{2+} inhibition measured at multiple contacts is compared to the Ca^{2+} inhibition predicted by their summed contact area, based on an additive linear model of contact area and distance derived from the single contact data. # marks the same data-point in (D-F). In (D), contact area of multiple nearby contacts refers to the largest contact area. The contact area of spherical surfaces is $6/\pi \approx 2$-fold overestimated due to the cubic approximation (reported values are uncorrected). Error bars indicate bootstrapped 95% confidence intervals.

3.2.4 Ca^{2+} inhibition at multiple contacts

The data shown so far were acquired at dendrite-sections carrying single inhibitory contacts. Additionally, in ∼30% of dendrite-sections I found multiple contacts nearby on the same branch (2-3 contacts within 1-12 μm) and I wondered whether these contacts could interact. Ca^{2+} inhibition at multiple contacts depended in a similar way on the largest contact area and distance from soma (Fig. 32 D-E), and for most contact pairs, Ca^{2+} inhibition was equal or even smaller than predicted by the summed contact area (based on a linear model fit to single contact data, Fig. 32 F). This suggests that multiple contacts on the same dendritic branch did not interact, but added their effect (sub)linearly.

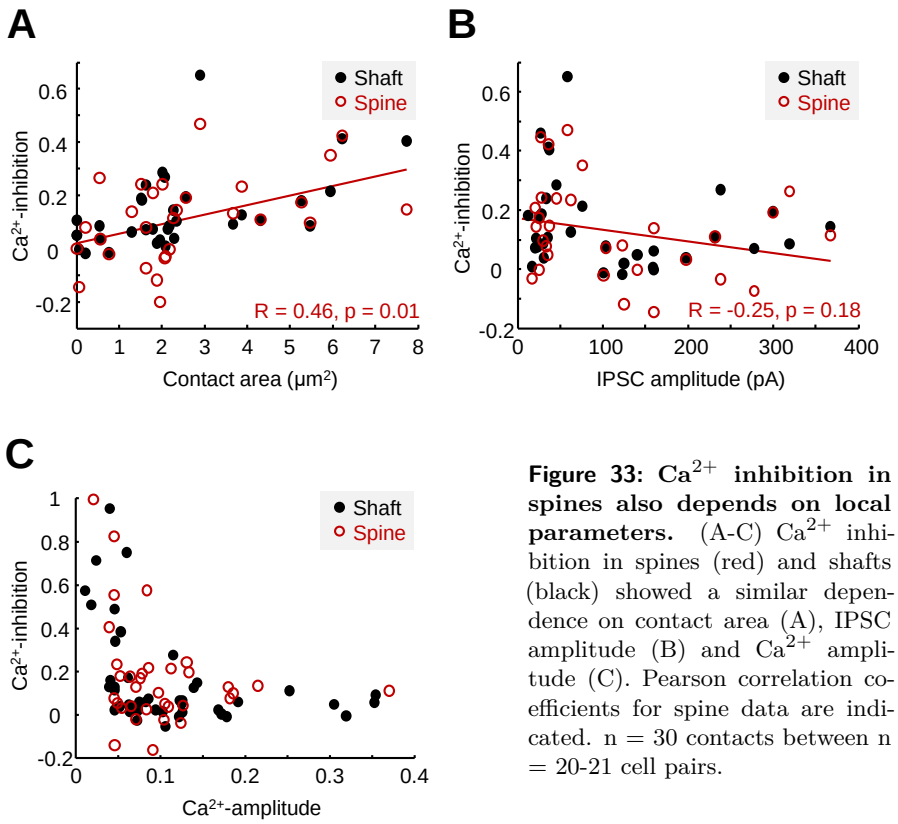

Figure 33: Ca^{2+} inhibition in spines also depends on local parameters. (A-C) Ca^{2+} inhibition in spines (red) and shafts (black) showed a similar dependence on contact area (A), IPSC amplitude (B) and Ca^{2+} amplitude (C). Pearson correlation coefficients for spine data are indicated. n = 30 contacts between n = 20-21 cell pairs.

3.2.5 Ca^{2+} inhibition can be modeled as a function of peak calcium and contact area

One pair of contacts with exceptionally strong inhibition (marked by # in Fig. 32 D-F, 5.4 μm^2 summed contact area) caught my eye. Since it had an unusually small Ca^{2+} transient, I looked more closely at the relation between Ca^{2+} inhibition and Ca^{2+} transient amplitudes. For contacts on distal dendrites at which ΔCa$^{2+}_{\text{ctrl}}$ was close to baseline fluctuations, I additionally applied bursts of 4 APs to the pyramidal cell (n = 3) to increase Ca^{2+} amplitudes. When I compared Ca^{2+} inhibition from both stimulation paradigms to the respective Ca^{2+} amplitude without inhibition, I found a striking, yet nonlinear correlation (Fig. 34 A-B, Spearman R = -0.59, p = 0.0006 for contacts >1 μm^2), indicating that inhibition was significantly larger for small Ca^{2+} transients. This finding was consistent across different contact areas and distances (Fig. 34 A-B), and also observed in spines (Fig. 33 C). I next derived a basic model describing inhibition of a thresholded voltage-dependent mechanism as a function of Ca^{2+} amplitude and inhibitory conductance (see APPENDIX III) which provided an excellent fit to the data (Fig. 34 B). As the model predicts, transients of small (slightly

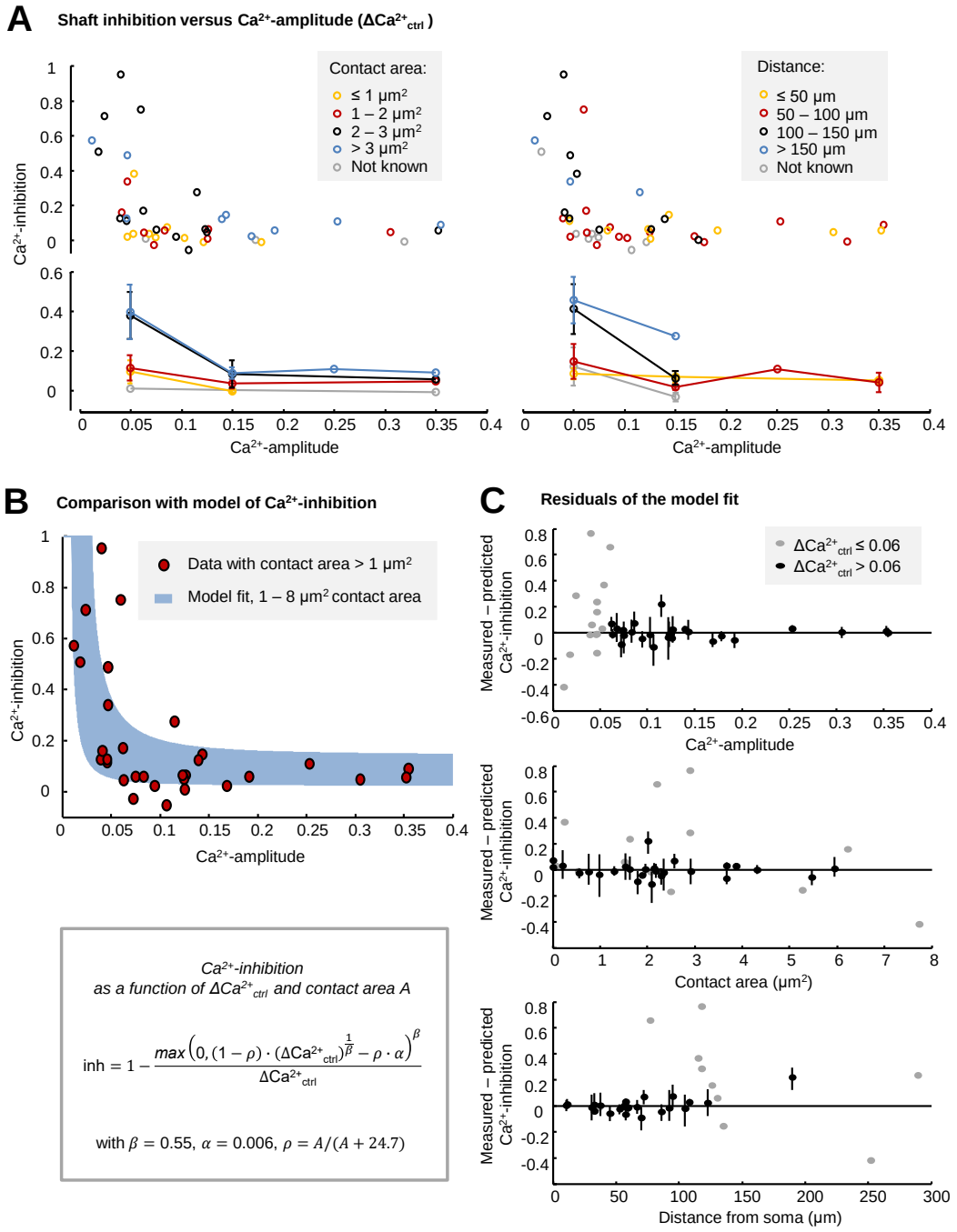

Figure 34: Model of Ca^{2+} inhibition. (A) Ca^{2+} inhibition at shafts strongly depended on the Ca^{2+} amplitude (ΔCa^{2+}_{ctrl}) for different contact areas (left panel) and distances (right panel). Lower panels present mean ± SEM of data in the upper panel, averaged in bins of 0.1 ΔCa^{2+}_{ctrl}. (B) Upper panel: Ca^{2+} inhibition was well fitted by a function of Ca^{2+} amplitude and contact area, indicating inhibition of VGCCs as the underlying mechanism. Red circles: data from contacts with area 1-8 μm^2, blue area: model fit, plotted for contact areas 1-8 μm^2. The fit was weighted by the inverse of bootstrapped variances. To avoid overestimation of small transients, ΔCa^{2+}_{ctrl} was quantified by averaging $\Delta G/R$ over 100 ms, corresponding to ∼75% of peak ΔCa^{2+}_{ctrl}. Lower panel: model function and fitted parameters. ρ: shunt-level, related to contact area A as a correlate of inhibitory conductance by $\rho = A/(A+\gamma)$. α, β, γ: free model parameters. (C) Residuals after fitting the model,

plotted versus Ca^{2+} amplitude (left), contact area (middle), and distance from soma (right). Data-points with $\Delta Ca^{2+}_{ctrl} \leq 0.06$ are shaded gray, since, due to the reciprocal function, small errors in ΔCa^{2+}_{ctrl} will result in large prediction errors for these data-points. Error bars indicate bootstrapped 95% confidence intervals.

supra-threshold) amplitude can be blocked by a comparably small inhibitory shunt. Analysis of the residuals shows that the model fully accounts for the observed relation between Ca^{2+} inhibition, Ca^{2+} amplitude, and contact area as a correlate of conductance (Fig. 34 C). Also, most of the increase of Ca^{2+} inhibition with distance from the soma is accounted for by the model, suggesting that part of the correlation seen in Fig. 32 B is a secondary effect of decreased Ca^{2+} amplitude with distance (Fig. 34 A, right). Therefore, the reduction in membrane potential which, in turn, reduces activation of voltage-gated Ca^{2+} channels (VGCCs) can mechanistically explain the strong dependence of Ca^{2+} inhibition on Ca^{2+} amplitude.

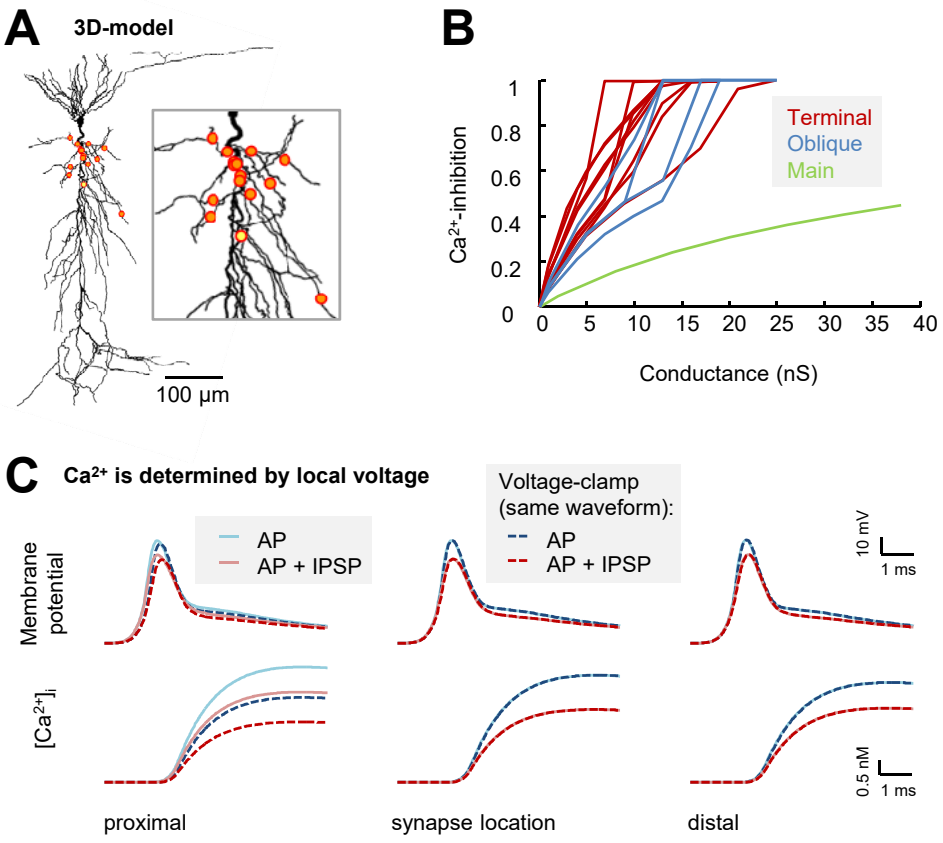

Figure 35: 3D-model of Ca^{2+} inhibition. (A) Shape plot of the multi-compartmental CA1 pyramidal cell model (n123 from Southampton archive). Red circles indicate locations of the 15 randomly distributed synapses (activated one at a time). Inset: zoom-in. (B) Relationship between maximum Ca^{2+} inhibition and inhibitory conductance at the 15 randomly distributed synapses. Colors code for branch-type (terminal oblique/oblique/main apical). (C) Comparison of recorded membrane-potentials (upper panels) and Ca^{2+} transients (lower panels) when an AP (blue) or AP + IPSP (red) were elicited (full lines) or when the recorded membrane potential was played back to a voltage-clamp at the synapse location (dashed lines). Representative example shown with 4 nS inhibitory conductance (synapse location yellow in A).

3.2.6 A model for the spatiotemporal profile of Ca^{2+} inhibition

While the simplified model of Ca^{2+} inhibition fits the data very well, it ignores the spatial and temporal dynamics of both the backpropagating AP and the IPSP. To account for these and help us interpret the following experiments mechanistically, I set up a multi-compartmental CA1 pyramidal cell model with detailed morphology, voltage-gated channel distributions and Ca^{2+} dynamics (Fig. 35 A, based on Poirazi et al., 2003a, for modifications see 2.6). Inhibitory synapses were randomly placed across the proximal third of the apical dendritic tree, across which Ca^{2+} responses were evoked by backpropagating APs. In the 3D-model, I could simultaneously record Ca^{2+} transients and membrane potentials associated with backpropagating APs, with and without activation of an individual inhibitory synapse. When I clamped the dendrite to the recorded voltage-waveforms, the same Ca^{2+} transients were induced at the synapse location and downstream in the dendrite, indicating that the local dendritic membrane potential fully dictates Ca^{2+} influx through VGCCs (Fig. 35 C). The level of Ca^{2+} inhibition increased roughly linearly (on average slightly sublinearly) with inhibitory conductance (Fig. 35 B) in accordance with the data (Fig. 32 A+D). These results are in agreement with the simple model and show that Ca^{2+} inhibition can be explained by a local reduction of dendritic membrane potential.

3.2.7 Ca^{2+} inhibition is highly spatially confined

My finding that Ca^{2+} inhibition is highly correlated with the local Ca^{2+} amplitude and contact area, but not with the global IPSC amplitude, strongly indicated that individual inhibitory contacts have a localized impact. I therefore wanted to determine the spatial (and temporal) precision of inhibition exerted by individual GABAergic synapses. To experimentally map the spatial profile of Ca^{2+} inhibition along the dendrite, I systematically varied the distance between the imaging line and the synaptic contact. I found that inhibition of Ca^{2+} transients was significantly reduced >2.5 μm proximally and distally of the contact (Fig. 36 A, $p < 0.05$, sign-test). After normalizing Ca^{2+} inhibition to the value measured at 0 μm (Fig. 36 B), length-constants of 22.6-24.9 μm proximal and 22.9-27.5 μm distal were estimated by variance-weighted exponential fitting (Fig. 36 C). Ca^{2+} inhibition in spines exhibited a similar bidirectional decline (Fig. 37). Exceptionally strong inhibition on the other hand, could propagate further into the distal compartment (Fig. 38). The results were in line with the model simulations (Fig. 36 D), which also showed an exponential and bidirectional decline of Ca^{2+} inhibition for moderate inhibition levels. To understand quantitative differences between the simulation and data, I explored some key parameters. Consistent with the shorter length-constants and the smaller cell size in the data (mice organotypic slice culture, compared to rat acute slice), length-constants scaled with the model size (Fig. 36 E). Length-constants were additionally shortened by ~13% if spines were added along the recorded branches with density 0.5/μm (orange symbols). A more symmetric profile (better matching the data) was achieved e.g. by slightly more delayed inhibition (see full spatiotemporal profile further below) or faster synapse kinetics (blue symbols).

3.2.8 Ca^{2+} inhibition is branch-specific

In addition to its high spatial precision, Ca^{2+} inhibition was also branch-specific: when I simultaneously recorded from a dendritic branch which carried an inhibitory contact and from one of its neighboring branches, inhibition dropped significantly between them (Fig. 39 A-B). Importantly, inhibition dropped significantly more between branches than predicted based on the average length-constants and the respective distances along the dendritic axis (right panel). According to the model, one major biophysical mechanism which promotes branch-specificity of Ca^{2+} inhibition is that branch-points act as a current-sink and proximal length-constants get smaller towards the branch-points (Fig. 39 C, left panel), which is the

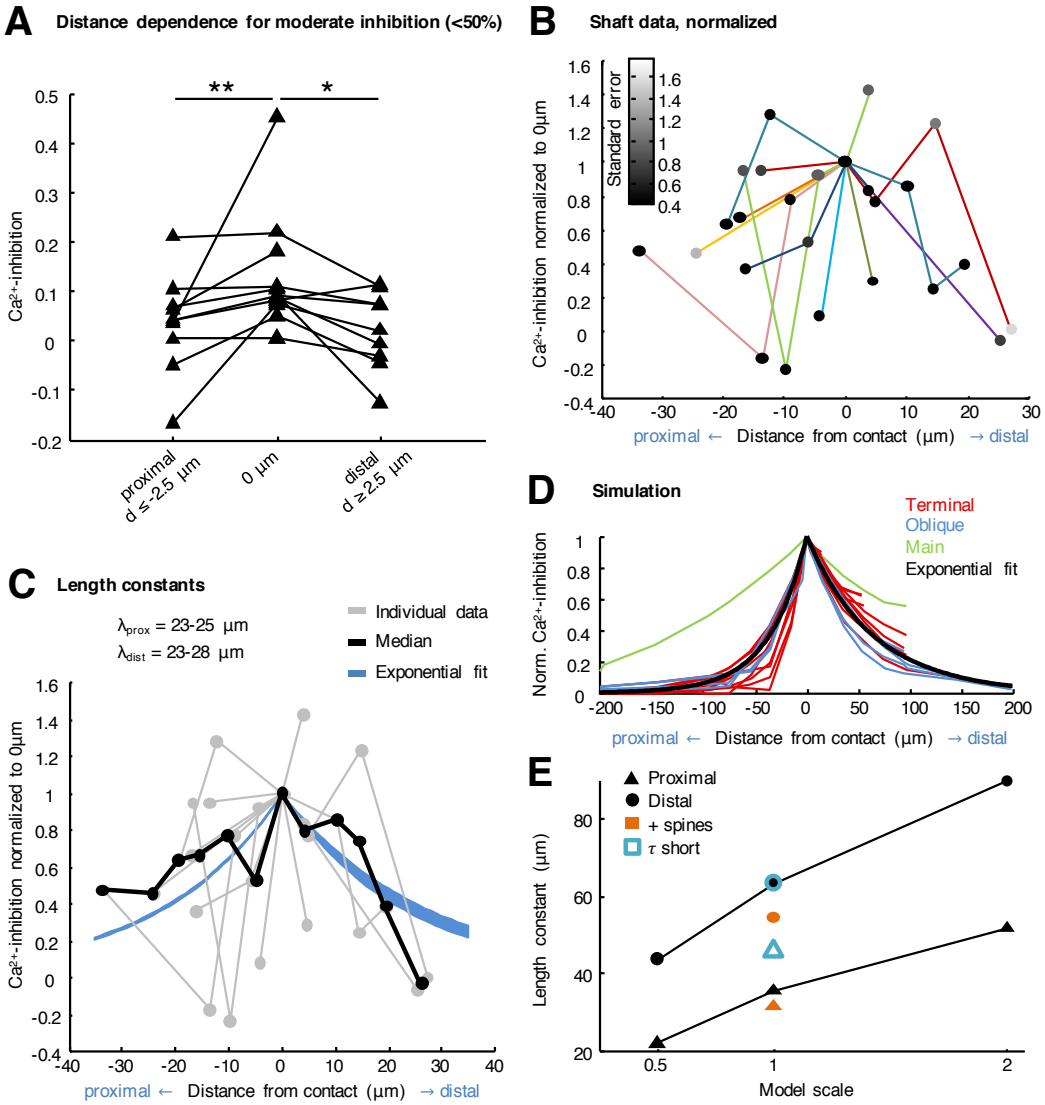

Figure 36: Ca^{2+} inhibition is distance-dependent. (A) Comparison between average inhibition at the contact (0 μm) and $\leq$ -2.5 μm or $\geq$ 2.5 μm away from the contact revealed that inhibition significantly drops in both directions (n = 10, p = 0.002 proximal, n = 9, p = 0.04 distal, sign-test, one data-series with Ca^{2+} inhibition <0 at 0 μm was excluded which did not affect significance). (B) Shaft Ca^{2+} inhibition for varying distances between imaging line and inhibitory contact, normalized to the Ca^{2+} inhibition at 0 μm for each dataset. Grayscale indicates the error estimated by bootstrapping and error-propagation. Data with Ca^{2+} inhibition > 0.5 was separately analyzed (Fig. 38). Colors code different contacts. (C) Normalized shaft data (gray) and median per 5 μm (black). Blue areas indicate the range of length-constants estimated with sliding threshold over the full dataset (n = 3-14 contacts in n = 12 cells). Data-points with error $\geq$1.75 were omitted in (B-C), but were included in the variance-weighted fit. One data-series with <0 Ca^{2+} inhibition at 0 μm was excluded before normalization. (D) Simulated spatial profile of Ca^{2+} inhibition (maximum <30%) at optimal spike-timing, normalized to its maximum. Black line: exponential fit. Colors code for branch-type. (E) Length-constants vary with model-parameters. Black: Length-constants of the simulated Ca^{2+} inhibition profile after scaling the model in size by 2 or 0.5. Orange: spines added with density 0.5/μm along the recorded branches. Blue: α-synapse with = 0.5 ms instead of 1 ms. Circles: distal, triangles: proximal length-constants.

opposite of the sealed-end effect which produces an increase of distal length-constants towards branch terminals (Fig. 39 C, right panel).

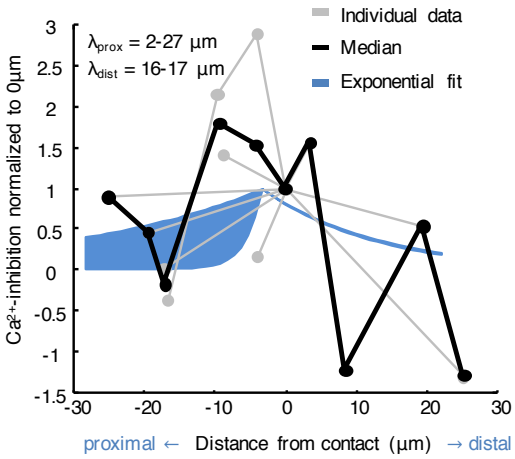

Figure 37: Distance-dependence of Ca^{2+} inhibition in spines. Normalized spine data (gray) and median per 5 μm (black). Blue areas indicate the range of length-constants estimated with sliding threshold over the full dataset (spines: n = 3-10 contacts in n = 10 cells). Variance of the data from spines was larger due to the intrinsically lower SNR (fewer pixels averaged), therefore the length-constants estimated from shaft data are more robust.

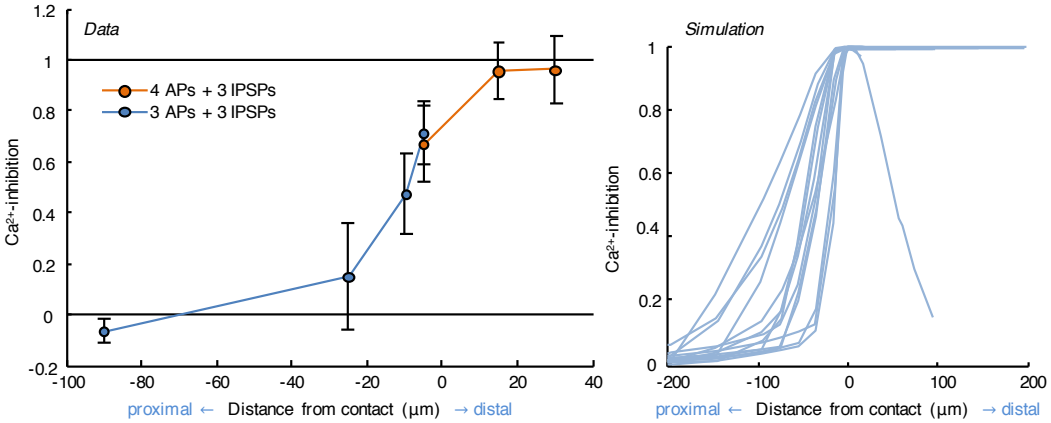

Figure 38: Strong inhibition of close-to-threshold signals. Left panel: Ca^{2+} inhibition at a contact with >50% inhibition also declined proximally, but extended up to 30 μm on the distal side (n = 1). Triple stimulation was barely detectable at the contact position, therefore the pyramidal cell was stimulated 4x for distal locations and Ca^{2+} inhibition was quantified by averaging ΔCa^{2+} over 100 ms. At 35 μm, even 4x stimulation failed to evoke a detectable Ca^{2+} transient (data not shown). Error bars indicate the bootstrapped standard deviation of each measurement. Right panel: Simulated spatial profiles of strong Ca^{2+} inhibition.

3.2.9 Ca^{2+} amplitudes in spines and shafts are inhibited to the same degree

Having observed the pronounced spatial confinement of Ca^{2+} inhibition along the longitudinal dendritic axis, I wondered whether Ca^{2+} inhibition would also be attenuated transversely between dendritic shafts and spines. Since theoretical studies have predicted that, due to chloride accumulation, $GABA_A$-receptor mediated inhibition will be ineffective on spines (Qian and Sejnowski, 1990), I focused on inhibitory shaft synapses, which are overall more abundant (Megías et al., 2001). Hence, the majority of inhibitory contacts in the dataset were located on dendritic shafts (87%, n = 48/55), while only 9% (5/55) were located on spine heads, and another 4% (2/55) contacted shaft and spine. Notably, at each contact the average Ca^{2+} inhibition under optimal conditions was highly correlated between spines and shafts (Pearson R = 0.73, p < 0.0001). However, since spines had an average minimum distance of 1.6 μm to the inhibitory contact, an exact quantification of attenuation required the pairwise comparison between equidistant spines and shafts. Remarkably, when I analyzed paired data acquired at spines and their neighboring shafts, Ca^{2+} inhibition was equally strong in both spine and shaft (Fig. 40, Pearson R = 0.36, p = 0.0004, median ratio $(1 - inh_{spine})/(1 - inh_{shaft}) = 0.98$ per individual spine/shaft pair). To rule out that a potential attenuation

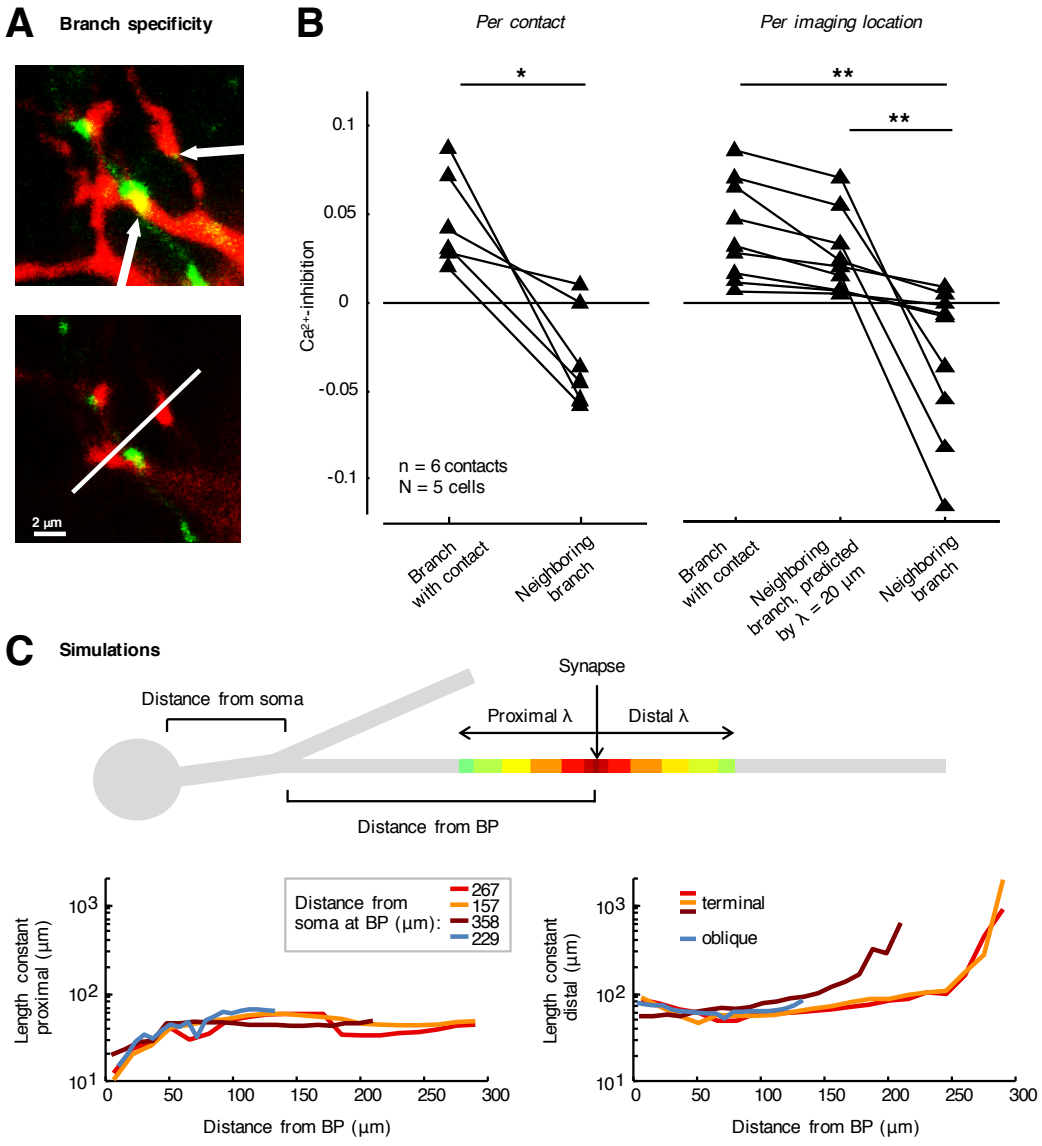

Figure 39: Long-term synaptic stimulation To measure differences in Ca^{2+} inhibition between branches, I analyzed paired data from simultaneous recordings at two neighboring branches. (A) Example configuration for a paired dataset; upper left: maximum projection, arrows point at branch with inhibitory contact and its neighboring branch; lower left: single z-plane, line scan over both branches indicated by white line. (B) Left panel: Pairwise comparison between Ca^{2+} inhibition at branches with inhibitory contact and their neighboring branches (n = 6 contacts, p = 0.03 sign-test, average across different imaging locations). Right panel: For every imaging location, Ca^{2+} inhibition at the neighboring branch was corrected for the distance along the dendritic axis, based on a length-constant of 20 μm. Ca^{2+} inhibition at the neighboring branch was significantly smaller than the distance-corrected values (p = 0.004 sign-test, n = 9 imaging locations). (C) Simulated proximal (lower left) and distal (lower right) length-constants for synapses with varying distance from a branch-point (BP). Simulations are shown for optimal spike-timing. Colors code different branches. Upper panel: Simulation scheme.

could be obscured by data-points exhibiting little inhibition or low SNR, I selected the subset of data showing significant inhibition (sign-test with $p < 0.025$ in the spine or shaft). This unbiased criterion was met in 9 spines, all with neck length <1 μm, and all in proximity (1-4 μm) to a shaft contact or a combined shaft+spine contact. Like in the full dataset, I observed

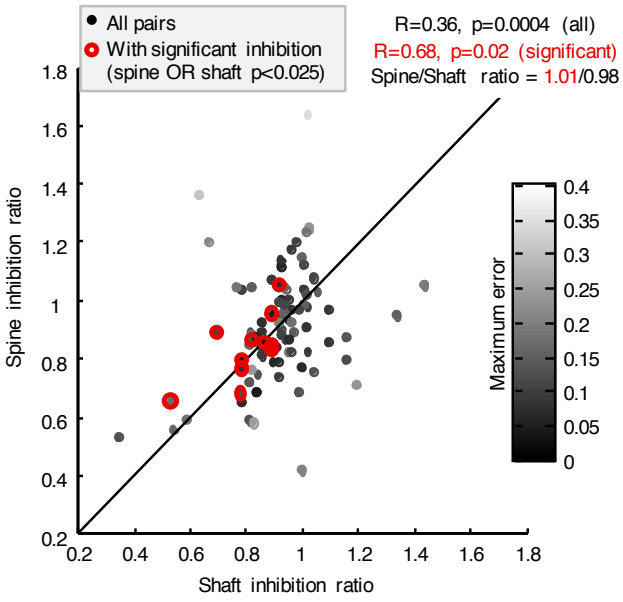

Figure 40: Ca^{2+} transients are equally inhibited in spines and shafts. Pairwise comparison of Ca^{2+} inhibition in individual dendritic spines and their neighboring shafts, averaged per stimulation protocol (94 protocols for n = 65 spines in n = 23 cells). For estimating the median ratio between spine inhibition and shaft inhibition (Spine/Shaft ratio), I used Ca^{2+} inhibition ratios (1-inh) to avoid division by negative numbers. Pearson correlation coefficients are indicated. Solid line is the unity line.

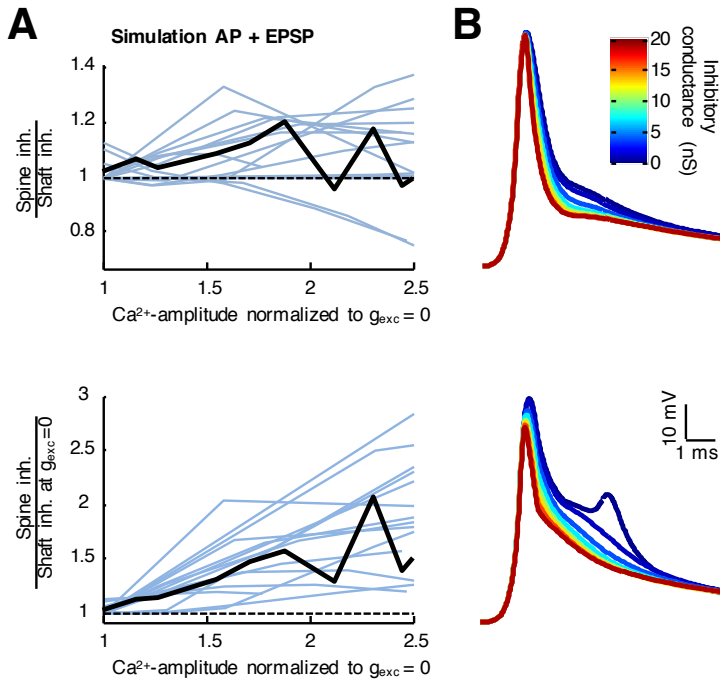

Figure 41: Ca^{2+} transients are equally inhibited in spines and shafts. Simulated pairing of a backpropagating AP and an EPSP arriving at a spine next to the inhibitory synapse; EPSP 2 ms delayed (LTD protocol). (A) Maximum Ca^{2+} inhibition at the spine head relative to the shaft, for varying excitatory conductances (relative increase of Ca^{2+} amplitude on the x-axis). Average across spines in black. (B) Same as (A), but normalized to the shaft Ca^{2+} inhibition for the AP alone. (C-D) Example membrane potentials recorded at the spine head for varying inhibitory conductances (color code).

no detectable attenuation along the spine neck (Pearson R = 0.68, p = 0.02, median ratio (1 - inh_{spine})/(1 - inh_{shaft}) = 1.01). In conclusion, the inhibition of Ca^{2+} transients spreading from the shaft to the spine is not attenuated along the spine neck.

In the model, this result was fully reproduced with spines of the average geometry suggested by the latest STED measurements (Tønnesen et al., 2014). Moreover, when I added an excitatory synapse on the spine which was activated with delay to the AP (mimicking an LTD-protocol), inhibition of the combined Ca^{2+} response could be even stronger in the spine than in the shaft for moderate excitatory conductances (Fig. 41 A, upper panel, data shown with maximum 30% shaft inhibition). And even more importantly, Ca^{2+} inhibition increased with the EPSP-size (Fig. 41 A, lower panel), since inhibition mechanistically acts by reducing the afterdepolarization around threshold for VGCCs (Fig. 41 B, upper panel) or even blocking secondary spikelets (Fig. 41 B, lower panel), which is both comparable to the supralinear inhibition of small Ca^{2+} signals which I have observed (Fig. 34). My results suggest that Ca^{2+} inhibition by shaft-synapses is on average equally effective in the spine and in the shaft, and that inhibition of Ca^{2+} signals in the presence of synaptic input can be much stronger than inhibition of APs alone.

3.2.10 Ca^{2+} inhibition is spike-timing-dependent

Synaptic integration and plasticity often depend crucially on the exact timing of different inputs, as exemplified by phenomena like spike-timing-dependent plasticity (Bi and Poo, 1998). In order to test the temporal precision of Ca^{2+} inhibition, I systematically varied the timing between pre- and postsynaptic APs, and found that Ca^{2+} inhibition was strongly spike-timing-dependent. On average, maximum inhibition occurred for simultaneous spikes (0 ms delay) and declined to its half-maximum within ±5-10 ms (Fig. 42 A). While the timing at which maximum inhibition occurred ('optimal spike-timing') exhibited some variation between inhibitory contacts, it was reproducible within most datasets (7 out of 10, corresponding to p=0.008). Comparing the data with simulations based on different synapse kinetics (Fig. 42 A, τ = 1 or 3 ms) suggested that the observed spike-timing dependence reflects fast synaptic currents. With fast synapse kinetics, the model further predicts a modulation of Ca^{2+} inhibition at smaller time-scales, and indeed, after aligning the cross-validated data to their optimal spike-timing, the median data showed a similar periodicity (Fig. 42 B). Furthermore, the model showed that the spike-timing profile of Ca^{2+} inhibition has the interesting property of being a mirror-image of the synaptic current (Fig. 42 B, inset), which indicates that the underlying mechanism of Ca^{2+} inhibition is a direct interaction between the inhibitory current and a fast AP-mediated process (Fig. 42 C), like VGCC-activation as suggested by the simplified model. Consistent with the simulation, the spike-timing-profile around 0 for triple stimulations matched a (lower SNR) dataset acquired using single APs (Fig. 42 D). Both were reasonably well-fit by an α-synapse current with time constant 1 ms (a simple synaptic conductance model, orange trace in Fig. 42 D), providing a (noise-limited) estimate for the kinetics of an individual GABAergic synaptic contact. Expectedly, the estimated kinetics of individual GABAergic synaptic inputs on dendrites is considerably faster than IPSC kinetics measured at the soma (Table 1) due to dendritic filtering. Notably, the simulated spike-timing profile was unchanged when I scaled the model to different sizes (data not shown), suggesting that the main conclusions in all likelihood will also hold (in a scaled fashion) in different model systems/animals.

Finally, I used the model to predict the 2-dimensional spatio-temporal profile of Ca^{2+} inhibition (Fig. 43). Besides demonstrating the high spatio-temporal precision of Ca^{2+} inhibition, the 2D-profile gives two more insights. Firstly, the two variables space and time are not independent, but the temporal profile becomes more symmetric for more delayed inhibition. Secondly, at earlier timing Ca^{2+} inhibition can be inverted (darker blue areas in

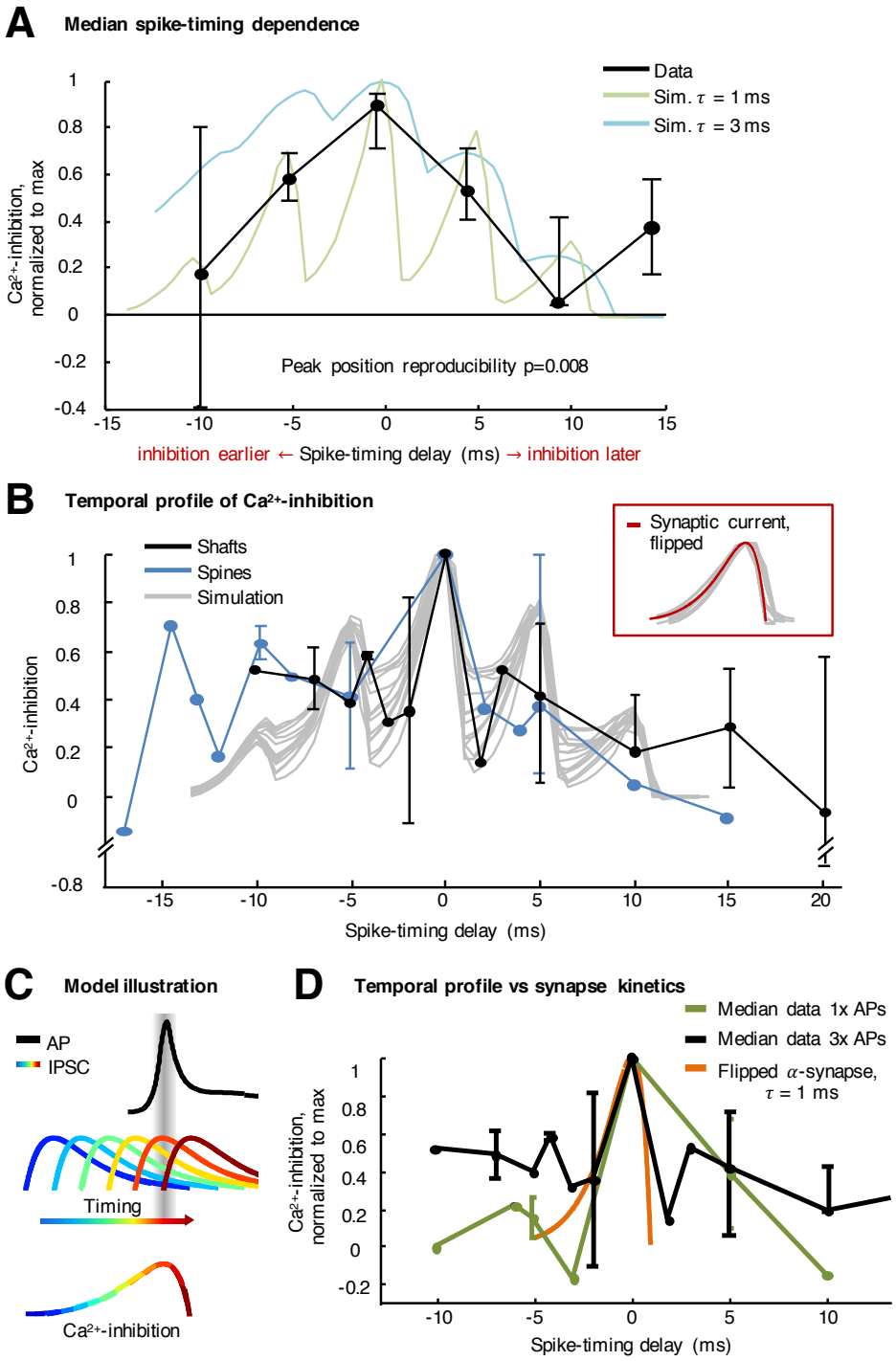

Figure 42: Ca^{2+} inhibition is spike-timing-dependent. (A) Median Ca^{2+} inhibition measured by 3x stimulation in dendritic shafts, plotted versus spike-timing delay. Ca^{2+} inhibition for each dataset was normalized to its maximum, before calculating the median per 5 ms bin. The optimal spike-timing was reproducible within most data-sets ($p = 0.008$ in shafts, $n = 10$, $p = 0.04$ in spines, $n = 9$). Light blue/green lines are representative examples for simulated Ca^{2+} inhibition profiles of 3x APs, shifted to optimal spike-timing. 3x α-synapse simulated with $\tau = 3$ ms (blue) or $\tau = 1$ ms (green). Note the higher frequency modulation for fast kinetics.

(B) When the data were aligned to respective optimal spike-timing and binned with 1 ms bins, a similar periodicity was observed in shafts (black) and spines (blue) as in the simulation for $\tau = 1$ ms (gray). Inset: The simulated spike-timing dependence of Ca^{2+} inhibition (1x stimulation in gray) is a mirror image of the synapse kinetics (flipped synaptic current in red). (C) Model illustration of a time-variant IPSC (colors indicate successive time-points) interacting with a time-invariant AP, resulting in a flipped time-course of inhibition. For negative spike-timing, the decaying flank of the IPSC coincides with the AP, while for positive spike-timing, the rising flank coincides with the AP. (D) Aligned 3x stimulation data (black) and 1x stimulation data (green) from shafts provide an upper estimate of synapse kinetics, and are well fit by an α-synapse with = 1 ms (orange). (A-D) Medians and bootstrapped 68% confidence intervals shown, no errorbars for singular observations. Medians included only data with significant Ca^{2+} inhibition > 0.085 (3x AP data) or Ca^{2+} inhibition > 0.085 (1x AP data in D). For aligned data (B+D), only data with cross-validated optimal spike-timing are shown to avoid noise-fitting: 8/11 (shafts) and 5/9 (spines) in (B), 4/8 (1x AP) in (D). Cross-validation was significantly above chance-level over a broad range of threshold choices (0 – 0.23 for shafts).

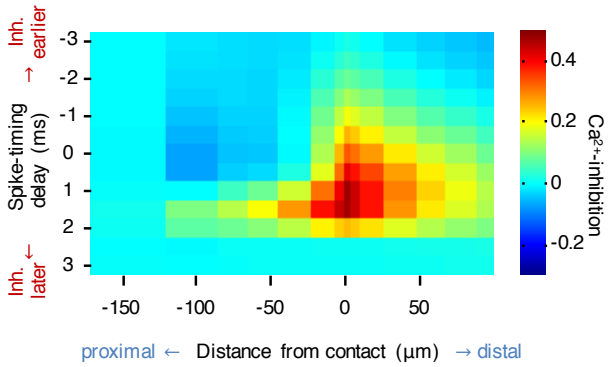

Figure 43: The spatiotemporal profile of Ca^{2+} inhibition Representative example for the spatio-temporal profile of Ca^{2+} inhibition around an individual inhibitory synapse. Taking synaptic and AP onset delays into acount, the simulation is about +1.3 ms shifted compared to the data.

Fig. 43) and effectively increase Ca^{2+} amplitudes by a small amount, which corresponds to a subtle broadening of the AP, e.g. due to a hyperpolarization-mediated relief of VGCCs from inactivation. This may explain the observed trend towards inverted Ca^{2+} inhibition at neighboring branches (right panel Fig. 39 B, not significant), and suggests that this is not a branch-specific effect per se.

3.3 THE MECHANISM OF CA^{2+} INHIBITION

Understanding that Ca^{2+} inhibition can be modeled as a direct consequence of altering the voltage-waveform of the backpropagating action-potential (Fig. 35), which in turn dictates a reduced opening of VGCCs, is already an important step towards understanding the mechanisms of Ca^{2+} inhibition. Yet, it leaves open the question how an opening of $GABA_A$-receptor conductances reduces or shapes the action-potential voltage-waveform. Traditionally, the actions of synaptic inhibition on membrane potential have been viewed as a dichotomy of shunt and hyperpolarization (1.13), which differ substantially in their biophysical behavior, both in the spatial and temporal domain. In the temporal domain, a transient hyperpolarization in response to the finite opening of inhibitory conductance reflects the local charging of the membrane, rendering the kinetics of IPSPs slower than the underlying inhibitory conductance (1.4 – 3.3 x halfwidth for the 15 synapses modeled in Fig. 35). In the spatial domain, attenuation of voltage and shunt level also differ: The attenuation of steady-state signals can be described by transfer resistances (Koch et al., 1982, Koch et al., 1983), and the attenuation in shunt level between two locations i and j equals the product of the voltage attenuation from i to j, times the voltage attenuation from j to i (Koch et al., 1990;

Gidon and Segev, 2012, summarized in Fig. 6). Therefore, shunt level attenuates more symmetrically along dendrites, while voltage attenuation is highly asymmetric due to increasing input impedance towards the sealed end (Rall and Rinzel, 1973, see Fig. 4 for comparison). Looking at the spatio-temporal profile of Ca^{2+} inhibition (with its temporal profile matching the time-course of synaptic conductance and with its fairly symmetric spatial profile), it is very appealing to attribute it to the inhibitory shunt level. Yet, the spatial profile is still considerably sharper than the attenuation of steady-state shunt levels would predict (with length-constants on the order of 100 μm, see Gidon and Segev, 2012 their Fig. 5). Again, an appealing explanation for these short length-constants is provided by the transient nature of both the IPSC and the action-potentials, since transient signals attenuate much faster than steady-state signals (Rinzel and Rall, 1974 and Koch, 1998, chapter 2). But to fully answer the question how the inhibitory shunt level really contributes to Ca^{2+} inhibition, one needs to take a closer look at the interaction between excitatory and inhibitory conductances.

Interestingly, if one describes the interaction between inhibition at a location i with excitation at a location e in terms of transfer resistances, one can show (see APPENDIX IV) that the relative inhibition at location e for large excitatory conductances g_e not only depends on the shunt level SL_e introduced by the inhibitory conductance g_i at location e, but additionally on the ratio between excitatory conductance and shunted leak conductance $K_{ee}*$ (eqn. 13):

$$\Delta V/V = SL_e \cdot 1/\left(1 + g_e \cdot K_{ee}*\right).$$

Intuitively, this means that the inhibition at location e is not purely dictated by the inhibitory leak, but by the balance between inhibitory and excitatory conductance. If the excitatory conductance is very large ($g_e \to \infty$), it can overcome the inhibitory shunt and therefore eliminate the inhibition ($\Delta V/V \to 0$). While equation 13 is derived for steady-state conditions and will quantitatively not be sufficient to fully describe Ca^{2+} inhibition happening at short time scales, it nevertheless points out a general principle. Equation 13 confirms that for very large excitatory conductances (as they open during a spike), the pure shunt-level attenuation is no longer sufficient to predict the spatial profile of inhibition, but the balance between inhibitory and excitatory shunt has to be taken into account. Furthermore, equation 13 provides an intuitive explanation for the spatial profile of Ca^{2+} inhibition exhibiting an unexpectedly fast decay distally: towards the sealed distal end, the contribution of excitatory conductance increases along with the input resistance and can therefore overcome the decreasing shunt level more easily. Only if the excitatory conductance itself decreases rapidly (i.e. for fading action-potentials), distal inhibition can increase despite the decreasing shunt level (see Fig. 38). Taken together, both observations (the graded, rather symmetrically attenuating inhibition of larger spikes, and the full blockade of small spikes) can be explained by the derived biophysical mechanism describing voltage inhibition as depending on shunt level, local input resistance and excitatory conductance (equation 13).

4 DISCUSSION

4.1 EXPERIMENTAL PARADIGM AND TOOL-DEVELOPMENT

4.1.1 Choice of the model system

Although the anatomical structure is preserved in organotypic hippocampal slice cultures and synapse properties closely mimick what is measured in ex-vivo preparations (De Simoni et al., 2003; Streit et al., 1989), certain limitations have to be taken into account when working with this model system. Main parameters which possibly differ between the culture and the in vivo situation are: (1) intercellular connectivity, (2) cell size, and synapse properties like (3) synaptic strength, (4) release statistics and (5) response kinetics. Since inhibitory function was measured at the level of individual synaptic contacts – in a way the quanta of synaptic inhibition – the results can be expected to be independent of the connection statistics between the inhibitory axons and the pyramidal cell dendrites (1). A much denser interconnectivity between inhibitory interneurons and pyramidal cells would have precluded the measurements, but would not make the results invalid. Of course, the extrapolation from the measured "quanta" of inhibition to what happens in the case of more inhibitory synapses being active simultaneously will depend on the connection statistics and inhibitory synapse density (see example calculation in 4.2.3).

The impact of cell-size (2) can be nicely studied in the 3D pyramidal cell model with realistic geometry by scaling all length-variables (dendrite length and radius, as well as length-variables of channels-distributions) by a certain factor, effectively squeezing or blowing up the model (Fig. 35 C). Interestingly, the length-constants of Ca^{2+} inhibition scale with the model size (with roughly a factor of 1.5 per factor 2 size change), while the spike-timing profile stays constant. Therefore, the main conclusions do not depend on cell size and in all likelihood will also hold (in a scaled fashion) in different model systems, and even in different animals.

While the basic rules which one can derive from the model regarding the length-constants of inhibition should also hold in different cell-types, the exact numbers for the length-constants are expected to vary. Since length-constants decrease towards branch-points and increase towards the distal ends (Fig. 39 C), the exact geometry and branching pattern will influence the spread of inhibition. Also the diameter of the dendrites will have an influence (compare main apical versus oblique dendrites in Fig. 36 D), as well as the presence or absence of dendritic spines (Fig. 36 E). Also very basic electrical properties like axial resistance or membrane resistivity will influence the length-constants, although their effect are small in comparison to the impact of geometry (Fig. 36 E). The effect of inhibitory conductance on length-constants is negligible over a large range, until it gets so large that it effectively blocks propagation (Fig. 38).

Differences in synapse properties like synaptic strength (3) or release statistics (4) will effectively vary the average amplitude of the inhibitory response. The experiments presented here do not have the resolution to look at variation between individual synapse properties or even single synaptic responses. The conclusions are therefore restricted to average synaptic responses. How Ca^{2+} inhibition depends on amplitude variations of the average synaptic response can be predicted based on the (simple or 3D) model of Ca^{2+} inhibition. According

to both models, the relationship between inhibitory conductance and Ca^{2+} inhibition is predicted to be roughly linear for moderate conductances (consistent with the correlation with contact area found in the data, Fig. 32 A+D), but to saturate for larger conductances, giving the relationship an overall slightly sublinear shape.

Differences in response kinetics (5) are predicted by the model to be directly reflected in the spike-timing profile of Ca^{2+} inhibition. It therefore turns out that differences in response kinetics are actually not a limitation for, but rather a strength of the experimental approach (see 4.2.6).

The variance in the Ca^{2+} inhibition level can be sufficiently explained by the parameters Ca^{2+}-amplitude and contact area (Fig. 34 C). While there is no evidence for additional cell-to-cell variability, it will be very interesting to study potential differences between interneuron-subtypes in the future.

4.1.2 Characterization of GABAergic interneurons

The firing profiles are overall consistent with previous reports for Reelin- or VIP-positive CGE-derived interneurons, yet, a number of differences were found between the interneurons targeted here for studying Ca^{2+} inhibition, and the overall population of GAD65-GFP interneurons (Wierenga et al., 2010), respectively the overall population of CGE-derived interneurons (Miyoshi et al., 2010). The overrepresentation of fast (>50 Hz) spiking cells in the present sample can be explained by the high recording temperature (34°C versus room temperature). The underrepresentation of irregular and strongly adapting cells indicates that a more homogeneous subgroup was selected by the applied selection criteria. For example, neurogliaform cells (small cells located in stratum lacunosum-moleculare) were successfully avoided, since none of the recorded cells displayed the slow, $GABA_B$ mediated response or persistent firing typical for this cell type. The fact that all selected interneurons were multipolar confirms that Calretinin-/VIP-positive interneuron-targeting interneurons (which are mostly bipolar, Wierenga et al., 2010) were most likely not included. The multipolarity is also consistent with the fact that no irregular spiking cells were found, since irregular spiking cells were described as bipolar by Miyoshi et al., 2010.

Based on our previous immunohistochemistry, GAD65-GFP positive INs are 70% Reelin- and 15% VIP-positive (Wierenga et al., 2010). However, most GFP-positive VIP cells, which either target other interneurons or form basket-like somatic synapses (Acsády et al., 1996), are located within or close to the pyramidal cell layer (Wierenga et al., 2010) which was not targeted for paired recordings. This finding is compatible with the fact that the interneurons selected here made functional inhibitory synapses with pyramidal cell dendrites (as indicated by the detectable IPSC) and suggests that Reelin-positive cells were targeted in the main.

Additional differences in the characteristics of certain cellgroups, e.g. LS1 and LS2 cells, indicate regional differences and temperature sensitivity on the one hand, but on the other hand also point out that clear definitions are often missing. These definition deficits are partially due to the fact that characteristics are overlapping between cell-groups and that there is no a priori rule which would dictate where to draw the borders. In the future, specific targeting of (at least) genetically defined subtypes of interneurons will help to evaluate the validity of subtype definitions.

4.1.3 Targeting GABAergic interneurons by biolistic transfection

Biolistic transfection with pmGAD65-EGFP and pmGAD67-EGFP vectors was established as a tool for targeting GABAergic interneuron. However, in addition to the low biolistic transfection efficiency, usability of the cloned pmGAD65-EGFP and pmGAD67-EGFP vectors was limited by the insufficient validation of their target specificity. A general problem for targeting GABAergic interneurons based on the GAD65 or GAD67 promoter is the enormous promoter length (>12 kb), impeding viral transfection strategies, and the uncertainty about which control elements are sufficient to ensure specificity. Probably due to the construct length, PCR amplification introduced a few point mutations as indicated by posthoc sequencing, which could in principle have affected targeting specificity. A more likely explanation, however, for the negative labeling with GAD67-antibodies (Fig. 16) is poor antibody performance, since GAD67-signals often did not even colocalize with GABA-signals. Moreover, GABA-staining, morphological analysis and firing patterns indicated that GABAergic interneurons were targeted. In general, antibodies performed much more poorly in slice cultures than in cryoslices of perfused brains. Likewise, an attempt to label inhibitory synapses in Ca^{2+} inhibition experiments posthoc with Gephyrin antibodies failed due to poor antibody labeling. In the future, posthoc embedding and subsectioning of slice cultures might help to at least increase penetration depth of the antibodies.

4.1.4 Choice of the stimulation paradigm

Electrical stimulation of inhibitory synapses was applied in this study, since it produces synaptic responses which are in their spatio-temporal precision closest to the physiological situation. The alternative route of optogenetic stimulation was not chosen, firstly for a lack of a proper transfection tool (see above), secondly for the inefficieny of single-axon stimulation, and thirdly since synaptic release is not fully physiological with optogenetic stimulation (Schoenenberger et al., 2011). Nevertheless, optogenetic stimulation might be in the future a valuable tool to perform similar experiments in vivo. The option of GABA uncaging on the other hand was not chosen, since only one-photon GABA-uncaging has so far been successfully established which does not even come close to mimicking synaptic responses, neither regarding spatial nor temporal resolution. Moreover, release statistics and variability in synaptic response amplitude or kinetics are unknown and can hence not be mimicked. The excellent practice of matching GABA-responses to miniature IPSCs (Murnick et al., 2002), albeit dendritically filtered and of unknown origin, cannot overcome this limitation, and is not even achieved in uncaging-paradigms (see slow kinetics of the uncaging IPSC in Hayama et al., 2013). Similar concerns hold for the iontophoretic application of GABA, albeit the temporal resolution is better in this case (Murnick et al., 2002).

While electrical stimulation produces the most physiological synaptic responses, it also has some disadvantages. Rundown of inhibitory responses due to washout was reduced by including GABA in the pipette, but could not be fully avoided. As a workaround, IPSC amplitudes were tracked throughout the experiments, and only data recorded with IPSC amplitudes varying around baseline (see Methods) were included. Additionally, the data were tested for rundown artifacts (see Fig. 8). Nevertheless, especially since the cause of the "run-up" phenomenon is not understood, it cannot be guaranteed that synaptic response amplitudes were fully physiological (see 4.1.1 on the consequences). Cell-attached stimulation, which prevents washout, proved technically intractable for long-term stimulation, since it decreased the success rate due to reduced, respectively incontrollable electrode stability. In addition, IPSC amplitudes cannot be measured in the cell-attached configuration, and changes in synaptic functionality or simply stimulation failures might occur unnoticed. Nevertheless, especially for shorter-term experiments, cell-attached stimulation will provide a valuable alternative stimulation tool to address similar questions in the future.

4.1.5 Calcium as readout of inhibitory synapse function

The function of inhibitory synapses can be addressed on many different levels, including its effects on voltage, calcium, or calcium-dependent phenomena like synaptic plasticity. Since fluorescence of a Ca^{2+} indicator was chosen as a functional readout, this study can only provide indirect, model-based information about membrane-voltage. However, Ca^{2+} signals are to a certain extent the more interesting readout, since they are more important than membrane voltage for downstream effects like synaptic plasticity. If membrane voltage had been measured, the question which effect this would have on calcium would be completely unresolved. By reading out calcium directly, this study can provide (direct or indirect) evidence to better understand both processes.

4.1.6 A paradigm for studying inhibition of synaptic plasticity

The paradigm for studying inhibition of synaptic plasticity was severely hampered by technical difficulties with the caged RuBi-glutamate. Time-consuming quality controls ruled out that experiments were started with excessive free glutamate concentrations in the solution, but still, moderate increases in free glutamate and built-up of free glutamate during the duration of an experiment could not be excluded or controlled for. Although endogenous glutamate concentrations are with ∼25 nM fairly low, 4 μm of exogenous glutamate can be cleared by endogenous glutamate uptake mechanisms (Herman and Jahr, 2007). However, contaminations of 4-7% as measured by spectral analysis, corresponding to 12-21 μM free glutamate, might very well exceed the uptake capacity. Excessive free glutamate could potentially also provide an explanation for the blockade of IPSCs, since as little as 0.5 μm glutamate have been shown to suppress inhibitory synaptic transmission (Chvanov et al., 1998). On the other hand, the blockade was a robust phenomenon and did not appear to depend on the quality of the caged glutamate batch.

Despite technical limitations, a pairing protocol for induction of synaptic plasticity was successfully established. However, the outcomes were more variable than expected, and the intended spine growth was induced, even in the most optimized setting, in only half of the experiments. Since concentrations of the caged glutamate were kept as low as possible to prevent inhibition of GABAergic synaptic transmission (Fig. 19), low uncaging efficiency often required full laser-power (up to 100 mW on sample, 4 ms pulse duration) targeted closely to the spine head in order to elicit responses, which probably contributed to the low efficiency of the uncaging paradigm, the considerable fraction of phototoxicity, and the blurred border between the two, since uncaging responses could be potentiated in cases otherwise classified as phototoxicity. It is very well conceivable that a certain percentage of phototoxicity was caused by the spine head expanding into the uncaging beam. Altogether, the variable outcome, especially the common observation of spine movements and retractions, indicate that a more-dimensional morphological analysis might be required to fully describe spike-timing-dependent plasticity in the presence of intact inhibitory synaptic transmission.

The time dimension provided additional challenges for the experimental setting: mapping the axodendritic contacts of an inhibitory interneuron with a pyramidal cell to identify putative synapses often required hours of screening. To prevent priming effects, only one plasticity paradigm with one inhibitory spike-timing delay could have been tested per cell. Additionally, it was completely unclear, which spike-timing difference would have an effect, thereby boosting the number of experiments required to potentially detect an effect.

The data presented in the previous chapters now moves the experiments for studying inhibition of synaptic plasticity closer into reach. The strong spike-timing-dependence of Ca^{2+} inhibition confirms the necessity of a very precisely timed pairing paradigm, and together with

the predictions of the model, offers the possibility to design such. In addition, a study combining glutamate and GABA-uncaging to address a very similar question has been published in the meantime (Hayama et al., 2013), which provides valuable insights into how GABAergic inhibition can promote spine shrinkage in an LTD protocol, which are fullly consistent with the data and modeling presented here. In the LTD pairing paradigm modeled here, shaft inhibition can indeed inhibit Ca^{2+} signals at the spine, and even more effectively than the AP alone. Interestingly, NMDA-receptor mediated Ca^{2+} influx was in the model inhibited to a much smaller degree than VGCC-mediated calcium, consistent with the inhibition-resistant nanodomains of NMDA-receptor-mediated Ca^{2+} influx described by Hayama et al., 2013. In order to design a spike-timing dependent pairing paradigm for vetoing LTP or spine growth, one will need to look closer into the interplay between inhibition and NMDA-receptor mediated Ca^{2+} influx. For this aim, the model presented here provides an exquisite foundation.

4.1.7 Contact area as a measure of synapse area

The data presented here show a clear correlation between contact area measured in 2PLSM and strength of Ca^{2+} inhibition, which is completely robust (also rank-correlation, variance-weighted correlation and correlation for only significant data all indicate $p<0.05$) and holds for the dataset including only single contacts, but also for the dataset including multiple contacts. Furthermore, assuming that contact area is linearly correlated with inhibitory conductance (as indicated by Fig. 32 A), the simple model of Ca^{2+} inhibition provides an excellent fit to the data (Fig. 34 C). Notwithstanding this result, it needs to be noted that 2PLSM contact cannot, due to resolution-limits of the point-spread-function, accurately quantify the true axo-dendritic contact area, which in turn is much larger than the actual synapse containing $GABA_A$-receptors, and therefore cannot be an exact measure of inhibitory conductance itself. Therefore 2PLSM contact area can only, as suggested by the data and model, serve as a proxy for inhibitory conductance. It is reassuring that also in the independently acquired EM-dataset, a strikingly similar relationship between the frequency of detecting a synapse in EM, and the previously measured frequency of significant Ca^{2+} inhibition, both in relation to the 2PLSM contact area, were found (Fig. 30 B). In the future, this correlation will help to guide experiments which aim at selecting strong individual inhibitory synapses, e.g. for optimizing SNR for sensitive measurements such as synapse kinetics.

Parts of the following chapter are taken from:

Müllner FE, Wierenga CJ, Bonhoeffer T (2015) *Precision of inhibition: Dendritic inhibition by individual GABAergic synapses on hippocampal pyramidal cells is confined in space and time*, Neuron 87:57–89.

4.2 INHIBITION OF DENDRITIC CA^{2+} TRANSIENTS BY INDIVIDUAL GABAERGIC SYNAPSES

Taken together, the data show that individual GABAergic synapses on dendritic shafts significantly inhibit Ca^{2+} transients from backpropagating APs within a narrow spatial and temporal window (length-constant 23-28 μm , time-constant <5 ms), and that Ca^{2+} transients in dendritic spines are inhibited to the same degree as in shafts. The narrow time-window together with the fast IPSC kinetics (Table 1) indicate that the measured Ca^{2+} inhibition is $GABA_A$-receptor mediated. While the degree of Ca^{2+} inhibition is overall moderate (Fig. 31 E, median inhibition 17.9% where significance was reached), it is nevertheless in a range which is likely to be physiologically relevant.

4.2.1 Ca^{2+} inhibition and synaptic plasticity

For instance, long-term potentiation depends steeply on the dendritic Ca^{2+} amplitude and is therefore sensitive even to small changes (Nevian and Sakmann, 2006, see their Fig. 8). In a GABA-dependent long-term depression paradigm, a robust induction of spine shrinkage corresponded to only 20-30% average reduction in Ca^{2+} amplitude (Hayama et al., 2013). Although the data is limited to the inhibition of backpropagating action-potentials, the model predicts that in an LTD protocol, Ca^{2+} inhibition of the combined EPSP+AP can be even larger than Ca^{2+} inhibition of the AP alone, suggesting that individual GABAergic synapses will be able to promote LTD at nearby spines. Moreover, the model provides a mechanistic explanation for the results of Hayama et al., 2013: inhibition can drive the membrane potential below the VGCC threshold or block secondary local spikelets induced by the EPSP, comparable to the supralinear inhibition of small bAPs (Fig. 34 A-B). While the low abundance of dendritic spines receiving inhibitory synapses (<10%, Megías et al., 2001) might have suggested that only a subset of excitatory synapses can be directly modulated by inhibition, the data indicate that potentially all spines can be controlled by shaft inhibition in the vicinity. Thus the data indicate that individual inhibitory shaft synapses have the potential to orchestrate synaptic plasticity and other Ca^{2+}-dependent processes at the surrounding dendritic spines.

4.2.2 Ca^{2+} inhibition acts via membrane potential reduction

My model demonstrates that the underlying biophysical mechanism of Ca^{2+} inhibition is the reduction in the voltage-waveform of the backpropagating AP, which dictates the magnitude and time-course of Ca^{2+} influx via the VGCCs (Fig. 35 C). It should be noted, however, that the spatiotemporal profile of voltage inhibition (measured as inhibition of spike amplitude) is not exactly the same as that of Ca^{2+} inhibition. The main reason for this mismatch is that activation of VGCCs depends on the complex waveform, not only on the amplitude of the spike. But also local properties can vary, such that the same AP waveform can result in different Ca^{2+} influx in different compartments. The interaction between IPSPs and APs which I studied here can be viewed in close analogy to the interaction between EPSPs and APs, which has been shown to also depend on the interference with voltage-dependent

conductances and underlie a sharp (albeit less sharp) spike-timing dependence (Stuart and Häusser, 2001, temporal profile is in their case similar to the EPSP, not EPSC waveform).

4.2.3 Ca^{2+} inhibition has a large dynamic range

The fact that inhibitory contact area is, after Ca^{2+} amplitude, the second major determinant of Ca^{2+} inhibition (Fig. 32 A+D, Fig. 33 A), predicts that not only coarse structural remodeling of inhibitory synapses (van Versendaal et al., 2012; Chen et al., 2012), but also gradual changes in synaptic strength can significantly alter levels of dendritic inhibition. Most interestingly, the dependence of Ca^{2+} inhibition on contact area (Fig. 32 A+D) respectively synaptic conductance (Fig. 34 B and 35 B) suggests that changes in inhibitory synaptic strength can dynamically modulate calcium over a broad parameter range. Considering realistic network activity, it is important to ask how multiple, simultaneously active inhibitory inputs will interact on the dendrite. My data and model suggest that Ca^{2+} inhibition scales roughly linearly (slightly sublinearly) with conductance (Fig. 32 A and Fig. 35 B), so for an average unitary Ca^{2+} inhibition of 15%, it needs ∼16 coactive synapses (simulation average, uniformly distributed over $\pm\ \lambda$) to fully block the Ca^{2+} transient, corresponding to 0.35 synapses/μm for $\lambda = 23\ \mu$m. For larger neurons with presumably longer length-constants (Fig. 36 E), an even lower synapse density would suffice (empirically found density for rat CA1 pyramidal neurons: 0.1-0.6/μm, Megías et al., 2001). In conclusion, different patterns of network activity will cover the full dynamic range of dendritic Ca^{2+} modulation, reaching from the moderate modulation (0-70%) of Ca^{2+} transient amplitude by unitary connections, which I describe here, to the full blockade of Ca^{2+} spikes by activation of inhibitory microcircuits, which others have observed (Miles et al., 1996; Müller et al., 2012).

4.2.4 The spatial profile of Ca^{2+} inhibition

Traditionally, the spatial spread of inhibition has been viewed in terms of electrotonic length-constants for hyperpolarization (e.g. Rall and Rinzel, 1973, in the order of several 100 μm, Brown et al., 1981) or length-constants of shunt-level (e.g. Gidon and Segev, 2012, ∼50% of electrotonic length), in comparison to which the length-constants of Ca^{2+} inhibition measured here are surprisingly short. This discrepancy reflects that Ca^{2+} inhibition is a phenomenon which occurs at and above VGCC threshold and therefore is by definition not a passive process. Furthermore, I show here that Ca^{2+} inhibition is a highly time-dependent process, and interactions between the space- and time-domain additional shape the spatial profile of inhibition, as one can see from the asymmetries in the spatiotemporal profile of inhibition (Fig. 43) as well as from the fact that length-constants depend on inhibitory synapse kinetics (Fig. 36 E). It is interesting to see that even in such a highly non-linear regime, inhibition decays fairly "canonically".

The data presented here estimate the radius over which individual GABAergic synapses influence Ca^{2+} signals on the dendrite. When comparing these length-constants (23-28 μm) to theoretically predicted and previously measured length-constants of inhibition, one needs to distinguish between different experimental paradigms. From a somatocentric viewpoint (with postsynaptic potentials measured at the soma), inhibition on-path of a propagating EPSP is expected to be more effective than inhibition distal of the excitatory synapse (Koch et al., 1983) – a prediction which has been confirmed by studying the interaction of iontophoretically evoked EPSPs and IPSPs (Hao et al., 2009). From a dendrocentric viewpoint however, one expects that local dendritic shunt-levels attenuate rather symmetrically in the proximal and distal direction (Gidon and Segev, 2012), with a slightly weaker attenuation towards the distal end going along with an increasing input resistance. Indeed, I observed a nearly symmetrical attenuation, similar to the inhibition of Ca^{2+} transients from backpropa-

gating action-potentials by one-photon GABA-uncaging (∼20 μm, Hayama et al., 2013). The proximal-distal asymmetry should be more pronounced if the inhibition is moved along the dendrite instead of the measurement (Gidon and Segev, 2012), consistent with measurements from one-photon GABA-uncaging with an uncaging spot moving towards the soma (∼11 μm, Kanemoto et al., 2011). The close correspondence of the results presented here with first approximations obtained by one-photon GABA-uncaging indicates that the limited spatial resolution of one-photon uncaging and co-activation of synapses did not result in an obvious overestimation.

4.2.5 Branch-specificity of Ca^{2+} inhibition

My observation that dendritic inhibition did not propagate into neighboring branches is in line with other recent data looking at compartmentalization of dendritic inhibition on a broader scale Marlin and Carter, 2014; Stokes et al., 2014) and supports the view of the dendritic branch as a fundamental processing unit (Branco and Häusser, 2010). In addition to branch-specific mechanisms which strengthen excitability (Losonczy et al., 2008), branch-specificity of inhibition might provide an important basis for the inhibition-dependence of branch-specific Ca^{2+} spikes (Cichon and Gan, 2015) and for dendritic information storage. Furthermore, branch-specificity confirms that Ca^{2+} inhibition is not diffusion- or spillover-mediated (the Euclidean distance between imaging spot and inhibitory contact was on average only 3.3 μm longer for neighboring branches). Regarding the mechanism of branch-specificity, my model indicates that branch-specificity is promoted by branch-points acting as current sinks. For future studies, it will be interesting to investigate further how additional properties – like branch-point-specific channel-distributions – can contribute to this phenomenon.

4.2.6 The temporal profile of Ca^{2+} inhibition reflects synaptic dynamics

Previous studies addressing the spatial or temporal precision of dendritic inhibition have employed one-photon GABA-uncaging (Kanemoto et al., 2011; Hayama et al., 2013) or GABA-iontophoresis (Liu, 2004; Hao et al., 2009) to activate $GABA_A$-receptors. They led to important insights, but – due to the artificial release of GABA – also have important methodological limitations: (1) synaptic specificity cannot be ensured (a limitation which is aggravated by the high abundance of extrasynaptic $GABA_A$-receptors), and (2) local amplitudes, amplitude-variations, and kinetics of individual synaptic responses are unknown and can hence not be mimicked. Thus, the data provide the first experimental evidence that synaptically mediated Ca^{2+} inhibition is spike-timing-dependent in the millisecond range. Along these lines it is interesting to note that, consistent with the finding that Ca^{2+} inhibition is most effective for synchronous spike-timing, most dendrite-targeting interneurons fire in synchrony with pyramidal cells at the trough of theta-rhythm or at the ascending phase of the theta-rhythm when phase-precessing pyramidal cells start firing (reviewed by Klausberger, 2009).

The time constant of Ca^{2+} inhibition reflects the kinetics of the underlying mechanistic process. The short time-constant indicates that Ca^{2+} inhibition is not due to an inhibitory process with a slower time-constant (e.g. any metabotropic effect), but directly reflects the interaction between the inhibitory conductance and the AP. Moreover, the close match between Ca^{2+} inhibition and IPSC kinetics indicates that inhibition acts on a process with even-faster time-constant, like VGCC activation, which is also suggested by the simplified model as the underlying mechanism. If inhibition would mechanistically act by reducing membrane-voltage over a longer time-scale (>1 ms), also the temporal Ca^{2+} inhibition profile should be broader (as resulting from a convolution of both processes).

In addition to providing mechanistic insight, an additional insight can be gained from the conclusion that the spike-timing dependence of Ca^{2+} inhibition is actually a mirror-image of the synaptic current. Due to this one-to-one correspondence, the data provide (to my knowledge) the first local measurement of inhibitory current kinetics from individual synaptic contacts. While the data do not have the time-resolution to fully resolve the synaptic dynamics, the α-synapse fit with time-constant of 1 ms (corresponding to 2.4 ms half-width and ∼2 ms mono-exponential decay time-constant from peak) provides a noise-limited estimate for dendritic $GABA_A$-synapse kinetics, which is in the range of previous indirect estimates for fast GABAergic synapses (Bartos et al., 2001) and emphasizes that somatically measured IPSCs (see Table 1) largely overestimate kinetics of remote synapses due to dendritic filtering. In future, this method might also be a valuable approach to measure the time-course of IPSCs and its variation between individual contacts, since it allows a local optical readout which is only limited by the precision of AP generation and measurement, not by comparably slow indicator dynamics.

4.2.7 Ca^{2+} inhibition in spines

Since the spine neck limits diffusion between the shaft and the spine head over timescales of 20-100 milliseconds (Svoboda et al., 1996), the Ca^{2+} inhibition which I measure in spines reflects inhibition of VGCCs in the spine head, rather than passively reflecting Ca^{2+} inhibition in the shaft (Sabatini and Svoboda, 2000; I obtained equivalent results to Fig. 40 with amplitudes detected within 20 ms, data not shown). The question of how Ca^{2+} signals in spines can be inhibited by GABAergic synapses on either spines or shafts has recently received a lot of attention. Two studies using an approach with larger scale and lower resolution than ours (multicellular optogenetic stimulation plus GABA uncaging) came to opposing conclusions. The first study concluded that Ca^{2+} inhibition resulting from GABAergic spine synapses is highly compartmentalized to spines (Chiu et al., 2013), the second study concluded that dendritic GABAergic synapses inhibit Ca^{2+} transients to the same degree in spines and shafts Marlin and Carter, 2014). Chiu et al., however, selected spines carrying potential synapses (or similarly "hot spots" of uncaging responses) based on the average Ca^{2+} inhibition, and subsequently used the same dataset for comparing average Ca^{2+} inhibition between selected spines and neighboring spines and shafts. This procedure results in a bias towards stronger inhibition in the selected spines ("regression to the mean" artifact), and spine inhibition is therefore overestimated. I now show with synaptic resolution that Ca^{2+} inhibition mediated by shaft-synapses shows no detectable attenuation in spines (at least for backpropagating APs). The result was reproduced, also in the presence of EPSPs, in the model which explicitly considered chloride accumulation (a factor which severely affects inhibition on spines or very small branches, also see Qian and Sejnowski, 1990).

My data did not provide strong evidence whether inhibitory spine synapses can inhibit Ca^{2+} transients or not. 2 of 55 putative contacts were made on spines and shafts, in which case it was not possible to discriminate spine and shaft inhibition. 5 of 55 putative contacts were made on perpendicular spines, such that spine inhibition could be discriminated from shaft inhibition; in none of the 5 spines or neighboring shafts significant inhibition was detected. Given their contact area, 2-3 of these contacts would have been expected to exhibit significant inhibition. While this sample is not large enough to rule out that inhibitory spine synapses could provide significant Ca^{2+} inhibition, it is nevertheless clear that the Ca^{2+} inhibition exerted by the interneuron-subpopulation selected in this project is mediated by inhibitory shaft synapses in the main.

While the data presented here shed light on the question how inhibition is attenuated across the average spine neck, it still remains an unsolved question, under which conditions spines can be potentially protected from shaft inhibition and which role potential direct spine inhi-

bition could play in this case. The answer to this question is still pending and will most likely require the collection of combined functional data from individual inhibitory spine-synapses and data quantifying local resistances, both of which are not easily accomplished. Interestingly, double-innervated spines in the cat frontal cortex show distinct properties (preferential thalamo-cortical innervation) than their single-innervated counterparts (Kubota et al., 2007), suggesting indeed a distinct physiological role or requirement for spine inhibitory synapses.

4.2.8 Conclusion

Relating the spatial spread of Ca^{2+} inhibition which I observed to the density of GABAergic synapses on pyramidal cell dendrites (Megías et al., 2001, Bourne and Harris, 2011), it is clear that GABAergic synapses form a functionally dense network, providing inhibitory control over basically every spot on the dendrite. Together with the observation that Ca^{2+} inhibition reaches comparable levels in spines and in shafts, this suggests that the collective inhibitory input to a pyramidal cell is sufficient to control dendritic Ca^{2+} levels across the whole dendritic arbor with micrometer and millisecond precision.

4.3 THE MECHANISM OF CA^{2+} INHIBITION

4.3.1 The three regimes of inhibition

The conclusion that the graded Ca^{2+} inhibition of backpropagating action-potentials is determined not by the inhibitory shunt level alone, but by an interaction between inhibitory and excitatory conductance, suggests a subdivision of synaptic inhibition into three regimes (which will overlap as determined by equation 12):

$$\frac{\Delta V}{V} = SL_e \cdot \frac{1}{1 + g_e \cdot K_{ee}^*} \cdot \left(1 - \frac{K_{ee}}{K_{ie}} \cdot \frac{E_i}{E_e} \cdot \frac{1}{ESL_e}\right)$$

1. **The hyperpolarization-regime**
   (small excitation and hyperpolarizing inhibition)

   If the excitation-induced shunt level is small (i.e. the excitatory conductance g_e is small in comparison to the leak conductance $\frac{1}{K_{ee}}$) and inhibition is hyperpolarizing ($E_i < 0$), the term

   $$-\frac{K_{ee}}{K_{ie}} \cdot \frac{E_i}{E_e} \cdot \frac{1}{ESL_e}$$

   can become significantly larger than 1. For example, with an excitation-induced shunt level of 5%, $ESL_e = 0.05$, and reversal of $E_i = -0.5 \cdot E_e$, it can equal up to 10. In this regime, the effect of inhibition is dominated by the hyperpolarization term

   $$SL_e \cdot \frac{1}{1 + g_e \cdot K_{ee}^*} \cdot \frac{K_{ee}}{K_{ie}} \cdot \frac{E_i}{E_e} \cdot \frac{1}{ESL_e}.$$

   Moreover, voltage attenuation dictates the spatial profile of inhibition in this regime, since the attenuation factor of the hyperpolarization term equals $\frac{K_{ie}^2}{K_{ee} \cdot K_{ii}} \cdot \frac{K_{ee}}{K_{ie}} = \frac{K_{ie}}{K_{ii}}$, which is the voltage attenuation from location i to location e. Inhibition acts in this regime, for example, if prolonged depolarizing currents are injected to the dendrite (see Buzsáki et al., 1996, inhibition decays with the IPSP waveform in this case).

2. **The shunt-level-regime**
   (small excitation and shunting inhibition)

If the excitatory conductance is small in comparison to the shunted leak conductance ($\frac{1}{1+g_e \cdot K_{ee}^*} \approx 1$) and the reversal of inhibition is close to resting membrane potential ($E_i \approx 0$), inhibition is proportional to the shunt level. In this regime, the attenuation of inhibition can be described purely by the shunt level attenuation $\frac{K_{ie}^2}{K_{ee} \cdot K_{ii}}$. Inhibition acts in this regime for moderate-sized EPSPs (see simulations by Gidon and Segev, 2012, but note that their model based on shunt-level is insufficient to describe inhibition of spikes, as exemplified by the data presented here).

3. **The tug-of-war-regime**
   (large excitation)

   For large excitatory conductances, excitatory conductances can compete with inhibitory shunt, and attenuation of inhibition can no longer be described by shunt level or voltage attenuation alone, but additionally depends on the contribution of excitatory conductance to the total leak and can in principle be overcome by excitation. Experimental data and a 3D model for this inhibition regime are presented here.

If one considers time-varying signals, also in the temporal domain different regimes can be discriminated. For very sustained increases in excitatory driving force (in the extreme case for steady state depolarizations), the inhibitory current has enough time to re- or hyperpolarize the membrane. In this case, the resulting inhibition will roughly follow the time-course of an IPSP (see Buzsáki et al., 1996). Please note that the membrane-charging time-constant dictates the time-course of inhibition in all three regimes under steady-state conditions, even if the charging will be speeded up by the shunt. In contrast, during very fast depolarizations like during a spike, the inhibitory current does not have time to charge the membrane, instead it instantaneously counteracts the depolarizing active conductances of the spike, thereby modulating the spike waveform. Once the spike has repolarized, the inhibitory current also ceases by lack of driving force, and no enduring change of membrane potential is caused. The fact that the temporal profile of Ca^{2+} inhibition in the case of backpropagating action-potentials matches the synaptic current additionally points out that inhibition acts on a time-scale even shorten than action-potential duration. This can be explained again by a threshold-effect: only around threshold (presumably of VGCCs), inhibition is competing with excitatory conductance and can be effective, while once the threshold has passed and additional voltage-gated conductances have opened, excitatory conductance fully outcompetes inhibitory conductance.

4.3.2 Predictions for spine-inhibition

The distinction between the different inhibition regimes is important for developing an intuition and deriving predictions regarding additional aspects of inhibition, which go beyond the experimental paradigm presented here. What first comes to mind is the long-standing question of attenuation across the spine-neck. The above conclusion, together with the scheme of spine neck attenuation derived earlier in Fig. 6, makes clear that also the question of spine-neck-attenuation needs to be viewed in the light of the three inhibition regimes. An increase in spine-neck resistance will limit the spread of inhibition in all three regimes, but it will have the strongest effect in the tug-of-war-regime, in which the attenuation of inhibition introduced by the excitatory conductance is larger

1. the smaller the shunt level, and

2. the larger the excitatory conductance compared to the leak conductance.

Since spine input resistance increases with neck-resistance, also the impact of excitatory conductance will increase along with the shunt level attenuation. Or in other words: shaft

inhibition will be most easily overcome by large excitatory input to spines with a small neck. It is highly interesting, however, that spines with average geometry do not experience any attenuation of Ca^{2+} inhibition (Fig. 40, 41 A), although the predicted shunt-level attenuation can be as large as 30%. This can be explained by two factors: First, the nonlinearity of Ca^{2+} inhibition causes inhibition to be more effective closer to the VGCC threshold (and hence more effective on additional synaptic input than on the spike alone, Fig. 41). Second, the spike is propagating and the spike-waveform at a downstream location also depends on the spike-waveform at further upstream locations. This exemplifies that the question how inhibition attenuates, depends in addition to the nature of the signal (voltage V/shunt S) and the propagation direction (inward/outward), also on what is inhibited and how sensitive the respective excitation E is to the three aspects of inhibition. In other words, inhibition depends additionally on the local E-V, E-I, and E-S relationships, their respective nonlinearities and time-dependencies.

Shaft input resistance is a crucial parameter for predicting attenuation across the spine neck (Fig. 6, Harnett et al., 2012) and causes a stronger inward voltage attenuation in proximal, less resistive dendrites. Interestingly, the effect of shaft input resistance on attenuation levels will be much less pronounced in the tug-of-war-regime than in the hyperpolarization- or shunt-level-regime: While on the one hand, shunt-levels will be more attenuated proximally with the decreased shaft input resistance, on the other hand, excitatory conductance will compete less with inhibition if multiplied with a smaller input resistance (eqn. 13), thereby partially compensating the stronger attenuation of shunt-level. To exemplify this point, let us assume we have a spine with $R_{neck} = 1$, $R_{head} \to \infty$, $R_{shaft} = 3$, and we reduce shaft resistance by 50% ($R_{shaft} = 1.5$). Absolute inhibition will decrease in any case, since the relative shunt level will decrease. But what happens to the attenuation of inhibition due to the neck? The shunt-level attenuation of $3/4 = 0.75$ (25% reduction) will be increased by a factor of 1.25 to $1.5/2.5 = 0.6$ (40% reduction). If now an excitatory conductance $g_e = 0.2$ opens on the spine head, the contribution of excitatory conductance in the tug-of-war regime will be reduced by a factor of 1.2 from $1/(1 + 0.2 \cdot 4) = 0.\bar{5}$ to $1/(1 + 0.2 \cdot 2.5) = 0.\bar{6}$ (for small g_i, or by 1.1 for $g_i = 0.2$). This example illustrates that passive voltage and shunt level attenuation and their specific distributions along the dendritic axis do not sufficiently reflect the attenuation of large-event inhibition, which acts in the tug-of-war regime and, additionally, displays strongly non-linear effects.

4.4 OUTLOOK

Firstly, the results presented here on the spatio-temporal precision of Ca^{2+} inhibition open the door for finally addressing the question which has initially inspired this project: The potential of inhibition to veto LTP has been repeatedly proposed in the literature, yet it still needs to be experimentally demonstrated that individual inhibitory synapses actually carry this potential. The realistic 3D model for Ca^{2+} inhibition introduced here provides the foundation for designing a pairing-protocol for inhibiting LTP, which could help to solve this long-standing question.

Secondly, the result that the temporal profile of Ca^{2+} inhibtion matches synaptic conductance kinetics provides an unprecedented tool to locally measure inhibitory synapse kinetics, which might help to better understand the biophysical basis of inhibition and dendritic integration.

Finally, the data and modeling results on spine inhibition indicate that individual inhibitory shaft-synapses have the potential to strongly inhibit Ca^{2+} signals in nearby spines, especially Ca^{2+} signals in the non-linear regime like locally generated spikes or spikelets. This exciting

result awaits additional experimental investigation which will shed further light on the long-standing question whether the spine-neck can protect spines from shaft inhibition and if yes, under which conditions. The result that the graded inhibition of spikes works in a tug-of-war-regime, together with the theoretical considerations presented here, might help design and understand these experiments better.

5 APPENDIX I

POSTHOC CORRECTION FOR SERIES RESISTANCE ERRORS

The basic principles of posthoc corrections for series resistance errors have been described elsewhere (Traynelis, 1998). Briefly, the measured current underestimates the true current by the capacitive component that recharges the membrane as a result of the voltage drop across the series resistance. This capacitive current is calculated based on the current derivative, multiplied by the series resistance and the estimated single-compartment membrane-capacitance, and added back to the measured current:

$$I_{corr} = I_{meas} + I_{cap} = I_{meas} + C_m \cdot \frac{dV}{dt} = I_{meas} + C_m \cdot R_s \cdot \frac{dI_{meas}}{dt}.$$

In addition, one has to consider the following error sources:

Firstly, the effective holding potential changes due to the series resistance error, and correspondingly, the amplitudes of any voltage-sensitive current, like the investigated $GABA_A$-receptor current, will change. When the holding potential V_{hold} is applied in voltage clamp, the true membrane potential is $V_{membr} = V_{hold} - I_{meas} \cdot R_s$. If the current-voltage relationship of the investigated current is approximately linear around the holding potential and if the driving force $V_{hold} - V_{rev}$ is known, one can correct this error by scaling the corrected current by the factor:

$$(V_{hold} - V_{rev}) \,/\, (V_{hold} - I_{meas} \cdot R_s - V_{rev})$$

.

Secondly, the membrane current across R_{in} is not constant, but will vary with the effective membrane voltage: $I_{in} \approx (V_{membr} - V_{rest}) \,/ R_{in}$. To separate the synaptic current from the membrane current flowing across the input resistance R_{in}, the additional term

$$(V_{hold} - I_{meas} \cdot R_s - V_{rest}) \,/ R_{in}$$

needs to be subtracted. Its contribution is often small (e.g. for 100 pA amplitude, $R_s = 10$ MΩ and $R_{in} = 200$ MΩ, 100 pA · 10 MΩ/ 200 MΩ = 5 pA = 5%).

The complete correction formula then denotes:

$$I_{corr} = \left(I_{meas} + C_m \cdot R_s \cdot \frac{dI}{dt} - \frac{(V_{hold} - I_{meas} \cdot R_s - V_{rest})}{R_{in}} \right) \cdot \frac{(V_{hold} - V_{rev})}{(V_{hold} - I_{meas} \cdot R_s - V_{rev})}$$

.

Since the current derivative amplifies noise, appropriate low-pass filters need to be applied, which cause an overestimate of synaptic kinetics. As an alternative smoothing approach which preserves kinetics over a large range of amplitudes, the rising phase can be fitted with a sigmoidal function of the form $y = A/\left(1 + B \cdot exp\left(-\lambda \cdot (x - \delta)\right)\right) + C$, and the derivative of the noisy current substituted by the derivative of the fitted function. This approach is

only suitable for the quantification of amplitude or (to a lesser extent) risetime, but not decay, and has been applied for the posthoc R_s correction of IPSC amplitudes shown in Fig. 27.

6 APPENDIX II

SERIES RESISTANCE CORRECTION FOR DENDRITIC INHIBITORY SYNAPTIC CURRENTS

IPSC amplitudes of unitary dendritic inhibitory synaptic connections were measured with varying series resistances. I observed that, under conditions where g_{syn} was presumably stable (independent of R_s), the product between peak IPSC amplitude and series resistance $I_{peak} \times R_s$ was as well stable (i. e. not correlated with R_s, Fig. 27). Here, I derive an equivalent circuit model which can explain this observation.

First, let us assume a single compartment voltage-clamp circuit, consisting of a cell's input resistance R_{in}, its membrane capacitance C_m and a synaptic conductance $g_{syn} = \frac{1}{R_{syn}}$ in parallel, and the series resistance R_s in series. This simplified one-compartmental model assumption is also underlying the on- or offline correction procedures for series resistance changes which are traditionally performed by adding the derivative of the measured current multiplied with the membrane time-constant.

In this model, the current measured across the series resistance I_{meas} equals the sum of I_{syn}, the synaptic current, I_{cap}, the capacitive current charging the membrane, and I_m, the current across the membrane:

$$I_{meas} = I_{syn} + I_{cap} + I_m \tag{1}$$

Let V_m denote the membrane voltage, V_{hold} the holding potential, V_{rest} the resting membrane potential, and V_{rev} the synaptic reversal potential. Then we can write:

$$\begin{aligned} I_{meas} &= (V_{hold} - V_m) / R_s \\ I_{syn} &= (V_m - V_{rev}) / R_{syn} \\ I_{cap} &= C_m \cdot \frac{dV_m}{dt} \\ I_m &= (V_m - V_{rest}) / R_{in} \end{aligned} \tag{2}$$

and substitute in Eq. (8) to receive

$$(V_{hold} - V_m) / R_s = (V_m - V_{rev}) / R_{syn} + C_m \cdot \frac{dV_m}{dt} + (V_m - V_{rest}) / R_{in}$$

as a differential equation of V_m. For instantaneous changes, e.g. of V_{hold} or R_{syn}, the analytical solution of this differential equation is an exponential function $V_m(t) = a \cdot exp(-b \cdot t) + c$, where c is the new steady state membrane potential

$$c = \frac{V_{rest}/R_{in} + V_{rev}/R_{syn} + V_{hold}/R_s}{\frac{1}{R_{in}} + \frac{1}{R_{syn}} + \frac{1}{R_s}}$$

$1/b$ is the membrane charging time-constant

$$1/b = C_m \cdot \frac{1}{\left(\frac{1}{R_{in}} + \frac{1}{R_{syn}} + \frac{1}{R_s}\right)}$$

and a is the difference between the old ($V_{ss} = \frac{V_{rest}/R_{in}+V_{hold}/R_s}{1/R_{in}+1/R_s}$) and the new steady state membrane potential

$$a = V_{ss} - c.$$

Please note that the membrane charging time-constant (i.e. the time-constant by which the membrane charges in an non-ideally voltage-clamped cell) is not equal to the membrane time-constant, traditionally defined as the time-constant by which the membran charges in response to a current-step in current-clamp mode. Let us now assume that we have an instantaneous change in $g_{syn} = \frac{1}{R_{syn}}$, e.g. corresponding to the opening of synaptic $GABA_A$ receptors upon transmitter binding, which occurs supposedly very fast in comparison to our membrane charging time-constants. The measured current I_{meas} will then follow the change in membrane potential according to Eq. (9).

In a realistic cell model, due to dendritic filtering the measured current will, together with the somatic membrane voltage, reach its maximum later than the membrane voltage at the synapse. In our simplified model, we treat the cell as a single compartment, so the compound membrane charging time-constant will determine how fast the synapse can recharge the membrane as a whole. We will discuss later what happens if the synapses are electrically more isolated from the soma.

Let T denote the time at which the peak membrane voltage is reached, corresponding to the time when the synaptic conductance shuts off, respectively to the open-time of the channels. We can now write the peak membrane voltage as

$$a \cdot exp\left(-b \cdot T\right) + c$$

and the measured peak current, after subtracting the baseline current, as

$$\begin{aligned} I_{peak} &= \frac{(V_{ss} - a \cdot exp\left(-b \cdot T\right) - c)}{R_s} \\ I_{peak} &= \frac{(V_{ss} - c) \cdot (1 - exp\left(-b \cdot T\right))}{R_s} \end{aligned} \tag{3}$$

This equation can be approximated in two marginal cases:

1. If the open time T is very long in comparison to the time-constant $1/b$, we can write Eq. (10) as follows.

$$\begin{aligned} I_{peak} &= \frac{1}{R_s} \cdot (V_{ss} - c) \\ I_{peak} \cdot R_s &= \frac{\frac{V_{rest}}{R_{in}} + \frac{V_{hold}}{R_s}}{\frac{1}{R_{in}} + \frac{1}{R_s}} - \frac{\frac{V_{rest}}{R_{in}} + \frac{V_{rev}}{R_{syn}} + \frac{V_{hold}}{R_s}}{\frac{1}{R_{in}} + \frac{1}{R_{syn}} + \frac{1}{R_s}} \end{aligned}$$

$$I_{peak} \cdot R_s \cdot \left(\frac{1}{R_{in}} + \frac{1}{R_{syn}} + \frac{1}{R_s}\right) = \frac{1}{R_{syn}} \cdot \left(\frac{\frac{(V_{hold}-V_{rev})}{R_s} + \frac{(V_{rest}-V_{rev})}{R_{in}}}{\frac{1}{R_s} + \frac{1}{R_{in}}}\right)$$

$$
\begin{aligned}
I_{peak} \cdot R_s \cdot \left(\frac{1}{R_{in}} + \frac{1}{R_s}\right) &= \frac{1}{R_{syn}} \cdot \left(\frac{\frac{(V_{hold}-V_{rev})}{R_s} + \frac{(V_{rest}-V_{rev})}{R_{in}}}{\frac{1}{R_s}+\frac{1}{R_{in}}} - I_{peak} \cdot R_s\right) \\
\frac{1}{R_{syn}} &= \frac{I_{peak} \cdot R_s \cdot \left(\frac{1}{R_{in}} + \frac{1}{R_s}\right)^2}{\frac{(V_{hold}-V_{rev})}{R_s} + \frac{(V_{rest}-V_{rev})}{R_{in}} - I_{peak} \cdot R_s \cdot \left(\frac{1}{R_{in}} + \frac{1}{R_s}\right)}
\end{aligned}
$$

However, this approximation does not describe the empirically found correlation between series resistance and IPSC amplitudes of unitary dendritic inhibitory synaptic connections.

2. If the open time T is very short in comparison to the time-constant $1/b$, we can do a Taylor-Approximation of Eq. (10):

$$
\begin{aligned}
I_{peak} &= \frac{(V_{ss}-c)\cdot(b\cdot T)}{R_s} \qquad (4)\\
I_{peak} \cdot R_s &= (V_{ss}-c)\cdot b \cdot T \\
I_{peak} \cdot R_s &= \left(\frac{\frac{V_{rest}}{R_{in}} + \frac{V_{hold}}{R_s}}{\frac{1}{R_{in}}+\frac{1}{R_s}} - \frac{\frac{V_{rest}}{R_{in}} + \frac{V_{rev}}{R_{syn}} + \frac{V_{hold}}{R_s}}{\frac{1}{R_{in}}+\frac{1}{R_{syn}}+\frac{1}{R_s}}\right) \cdot \frac{T}{C_m} \cdot \left(\frac{1}{R_{in}} + \frac{1}{R_{syn}} + \frac{1}{R_s}\right) \\
I_{peak} \cdot R_s &= \frac{1}{R_{syn}} \cdot \left(\frac{\frac{(V_{hold}-V_{rev})}{R_s} + \frac{(V_{rest}-V_{rev})}{R_{in}}}{\frac{1}{R_s}+\frac{1}{R_{in}}}\right) \cdot \frac{T}{C_m} \\
\frac{1}{R_{syn}} &= I_{peak} \cdot R_s \cdot \frac{C_m}{T} \cdot \left(\frac{\frac{1}{R_s}+\frac{1}{R_{in}}}{\frac{(V_{hold}-V_{rev})}{R_s} + \frac{(V_{rest}-V_{rev})}{R_{in}}}\right) \\
\frac{1}{R_{syn}} &= I_{peak} \cdot R_s \cdot \frac{C_m}{T} \cdot \left(\frac{R_s + R_{in}}{(V_{hold}-V_{rev})\cdot R_{in} + (V_{rest}-V_{rev})\cdot R_s}\right) \\
\frac{1}{R_{syn}} &= I_{peak} \cdot R_s \cdot \frac{C_m}{T} \cdot \left((V_{hold}-V_{rev})\cdot \frac{R_{in}}{R_s+R_{in}} + (V_{rest}-V_{rev})\cdot \frac{R_s}{R_s+R_{in}}\right)^{-1}.
\end{aligned}
$$

$GABA_A$-receptor mediated IPSCs reverse close to the resting membrane potential, $V_{rev} \approx V_{rest}$, so for sufficienctly high input resistance, $R_{in} \gg R_s$, we can approximate

$$
\left((V_{hold}-V_{rev})\cdot \frac{R_{in}}{R_s+R_{in}} + (V_{rest}-V_{rev})\cdot \frac{R_s}{R_s+R_{in}}\right) = (V_{hold}-V_{rev}) \qquad (5)
$$

and

$$
\frac{1}{R_{syn}} = \frac{I_{peak}\cdot R_s}{(V_{hold}-V_{rev})} \cdot \frac{C_m}{T} \qquad (6)
$$

$$
\frac{1}{R_{syn}} \propto I_{peak} \cdot R_s \qquad (7)
$$

Indeed, the correlation (7) matches the empirically found relationship between series resistance and IPSC amplitudes of unitary dendritic inhibitory synaptic connections for stable synaptic conductances well. Please note that the membrane charging time-constant $1/b$ and the goodness of approximation (7) depend on R_s and R_{in}: the larger R_s and R_{in}, the larger the membrane charging time-constant, and the better the Taylor approximation (4) as well

as the approximation (6), which ultimately leads to equation (7).

For synapses with dendritic location, the effective input resistance at synapses with dendritic location is higher than the somatically measured input resistance. Likewise, the effective series resistance is the sum of axial and access resistance and therefore also larger than the somatically measured R_s. Therefore accuracy of the approximation (7) increases if effective resistances are considered. On the other hand, the somatically measured series resistance will underestimate the effective series resistance (i.e. the sum of series and axial resistance), and for very distal synapses Eq. (7) will no longer hold if somatically measured resistances are considered. Taking into account that the contribution of a synaptic input to the compound IPSC measured at the soma also decreases with distance and R_{ax}, the empirically found relationship could therefore reflect that the somatically measured IPSC is largely dominated by synaptic responses from the more proximal dendritic contacts.

The simplified model circuit disregards several important factors, like cell geometry or capacitive currents across the membrane. I therefore tested whether the approximation is also appropriate under more realistic circumstances, by employing a multi-compartmental model of a CA1 pyramidal cell (Poirazi et al., 2003a) in the NEURON simulation environment to study the relationship between somatically measured IPSC-amplitude and series resistance. The simulations indicated that several factors influence whether the product of simulated IPSC amplitudes and series resistances is approximately constant, most of all the synapse distribution and the synapse kinetics. As predicted, the approximation was most adequate for very short kinetics, dendritic synapses and dominated by the most proximal synapses. Therefore, the empirically found relationship between IPSC amplitudes and series resistance cannot be generalized across different cell types and synapse types. Moreover, $I_{peak} \times R_s$ as a measure of synaptic conductance cannot be compared between cells.

7 APPENDIX III

This appendix has been adapted from the Supplemental Material of: Müllner FE, Wierenga CJ, Bonhoeffer T (2015) *Precision of inhibition: Dendritic inhibition by individual GABAergic synapses on hippocampal pyramidal cells is confined in space and time*, Neuron 87:576–89.

A SIMPLE MODEL OF CA^{2+} INHIBITION

If an inhibitory conductance g_i opens in addition to an inward current I, the resulting membrane potential change ΔV can in a passive circuit be described by

$$\Delta V_{inh} = \frac{I - g_i \cdot (V_{rest} - E_i)}{g_{leak} + g_i},$$

where E_i is the inhibitory reversal potential, g_{leak} is the leak conductance and V_{rest} the resting membrane potential. The term $g_i \cdot (V_{rest} - E_i)$ in the numerator will cause a hyperpolarization if $E_i < V_{rest}$. The addend g_i in the denominator reduces the depolarization $\Delta V = \frac{I}{g_{leak}}$ by the factor

$$g_{leak} / \left(g_{leak} + g_i\right) = 1 - g_i / \left(g_{leak} + g_i\right),$$

whereby

$$\rho = g_i / \left(g_{leak} + g_i\right) \tag{8}$$

is called the *shunt-level*. So we can write

$$\Delta V_{inh} = (1 - \rho) \cdot \Delta V - \rho \cdot \delta,$$

with inhibitory driving force $\delta = (V_{rest} - E_i)$.

In my experiments, I measure dendritic Ca^{2+}-transients which are depending on voltage-gated calcium channels (VGCCs, see Christie et al., 1995, Pérez-Garci et al., 2013). Only if the backpropagating spike depolarizes the membrane beyond a threshold, the Ca^{2+}-transient is initiated. We can therefore write changes in Ca^{2+}-concentration as a thresholded function of membrane potential:

$$\Delta Ca^{2+}\left(\Delta V\right) = f\left(max\left(\Delta V - \theta, 0\right)\right), \; f(0) = 0, \tag{9}$$

which equals 0 below the voltage-threshold θ, and follows the unknown, but presumably monotonous, function f above threshold. In Fig. 34, I show integrated $\int Ca^{2+}$ for improved signal-to-noise ratio, but since $\int Ca^{2+}$ and ΔCa^{2+} are highly correlated, I do not make a distinction in the following. Likewise, ΔV has in reality a complex time-dependent waveform, which I disregard in this simplified model. Inversely, we can then write ΔV as a function of calcium-concentration:

$$\Delta V = f^{-1}\left(\Delta Ca^{2+}\right) + \theta$$

for concentration changes > 0. Accordingly, the change in calcium resulting from a depolarization of size ΔV_{inh} can be written as

$$\begin{aligned}
\Delta Ca^{2+}_{inh} &= f\left(max\left(\Delta V_{inh} - \theta, 0\right)\right) \\
&= f\left(max\left((1-\rho)\cdot\Delta V - \theta - \rho\cdot\delta, 0\right)\right) \\
&= f\left(max\left((1-\rho)\cdot\left(f^{-1}\left(\Delta Ca^{2+}\right)+\theta\right) - \theta - \rho\cdot\delta, 0\right)\right) \\
&= f\left(max\left((1-\rho)\cdot f^{-1}\left(\Delta Ca^{2+}\right) - \rho\cdot\left(\theta+\delta\right), 0\right)\right).
\end{aligned}$$

The hyperpolarization therefore acts on the Ca^{2+}-transient by adding the driving force δ to the threshold θ, while the shunting inhibition acts by scaling down the depolarization. In first approximation, we express f as a power function:

$$\Delta Ca^{2+} = max\left(\kappa\cdot\left(\Delta V - \theta\right), 0\right)^{\beta}, \text{ with } \beta > 0 \text{ and } \kappa \neq 0.$$

Then we can derive for the Ca^{2+}-inhibition:

$$\begin{aligned}
1 - \frac{\Delta Ca^{2+}_{inh}}{\Delta Ca^{2+}_{ctrl}} &= 1 - \frac{max\left(\kappa\cdot\left(\left(1-\rho\right)\cdot\left(\Delta Ca^{2+}_{ctrl}\right)^{\frac{1}{\beta}}/\kappa - \rho\cdot\left(\theta+\delta\right)\right), 0\right)^{\beta}}{\Delta Ca^{2+}_{ctrl}} \\
&= 1 - \frac{max\left(\left(1-\rho\right)\cdot\left(\Delta Ca^{2+}_{ctrl}\right)^{\frac{1}{\beta}} - \rho\cdot\left(\kappa\cdot\theta + \kappa\cdot\delta\right), 0\right)^{\beta}}{\Delta Ca^{2+}_{ctrl}}, \qquad (10)
\end{aligned}$$

which is a right-shifted reciprocal function as shown in Fig. 4B. For simplicity we define $\alpha = \kappa\cdot\theta + \kappa\cdot\delta$. If we assume a linear relationship ($\beta = 1$), this simplifies to:

$$\begin{aligned}
1 - \Delta Ca^{2+}_{inh}/\Delta Ca^{2+}_{ctrl} &= 1 - \frac{max\left(\left(1-\rho\right)\cdot\Delta Ca^{2+}_{ctrl} - \rho\cdot\alpha, 0\right)}{\Delta Ca^{2+}_{ctrl}} \\
&= min\left(\rho + \rho\cdot\alpha/\Delta Ca^{2+}_{ctrl}, 1\right) \\
&= min\left(\rho\cdot\left(1 + \alpha/\Delta Ca^{2+}_{ctrl}\right), 1\right) \qquad (11)
\end{aligned}$$

Assuming that the inhibitory conductance g_i is correlated with the contact area A (also see Fig. 32 A), I substituted the shunt-level $\rho = g_i/\left(g_i + g_{leak}\right)$ by $\rho = A/\left(A+\gamma\right)$ for fitting equation (10) and (11) to our data. The free parameter γ can therefore be interpreted as a correlate of the leak conductance g_{leak}. While the linear approximation (11) describes the data well, a better fit is achieved (4% less sum of squared errors) using equation (10) with $\kappa\cdot\theta + \kappa\cdot\delta = \alpha = 0.006$, $\gamma = 24.7$, and $\beta = 0.55$ (i.e. a slightly concave Ca^{2+} V-relationship). In conclusion, the strong Ca^{2+} inhibition for small Ca^{2+} can be explained by inhibition of a voltage-gated calcium-mechanism with a steep onset, which behaves fairly linear within our experimental setting. We know that backpropagating action-potential evoked Ca^{2+} transients depend on VGCCs (Christie et al., 1995, Pérez-Garci et al., 2013). Given the fast kinetics of the Ca^{2+} transients (20-80% risetime of 8.9 ms for triple APs and <2 ms for single APs), the relationship we see in Fig. 4 is presumably the signature of the activation of fast T-type or low-voltage-activated L-type channels like $Ca_v1.3$.

8 APPENDIX IV

THE MECHANISM OF CA^{2+} INHIBITION

Let us consider the situation when an excitatory conductance g_e with reversal potential E_e opens at location e simultaneously with an inhibitory conductance g_i with reversal potential E_i opening at location i. In equilibrium, the membrane voltages V_i^* at location i and V_e^* at location e will be determined by the two coupled equations

$$\begin{aligned} V_i^* &= K_{ii} \cdot (E_i - V_i^*) \cdot g_i + K_{ie} \cdot (E_e - V_e^*) \cdot g_e \\ V_e^* &= K_{ie} \cdot (E_i - V_i^*) \cdot g_i + K_{ee} \cdot (E_e - V_e^*) \cdot g_e \end{aligned}$$

By substitution we obtain:

$$\begin{aligned} V_i^* \cdot (1 + K_{ii} \cdot g_i) &= K_{ii} \cdot E_i \cdot g_i + K_{ie} \cdot (E_e - V_e^*) \cdot g_e \\ V_i^* &= \frac{K_{ii} \cdot E_i \cdot g_i + K_{ie} \cdot (E_e - V_e^*) \cdot g_e}{(1 + K_{ii} \cdot g_i)} \\ V_e^* \cdot (1 + K_{ee} \cdot g_e) &= K_{ie} \cdot \left(E_i - \frac{K_{ii} \cdot E_i \cdot g_i + K_{ie} \cdot (E_e - V_e^*) \cdot g_e}{(1 + K_{ii} \cdot g_i)} \right) \cdot g_i + K_{ee} \cdot E_e \cdot g_e \\ V_e^* \cdot \left(1 + K_{ee} \cdot g_e - \frac{K_{ie}^2 \cdot g_e \cdot g_i}{(1 + K_{ii} \cdot g_i)} \right) &= K_{ie} \cdot \left(\frac{E_i - K_{ie} \cdot E_e \cdot g_e}{(1 + K_{ii} \cdot g_i)} \right) \cdot g_i + K_{ee} \cdot E_e \cdot g_e \\ V_e^* &= \frac{K_{ie} \cdot \left(\frac{E_i - K_{ie} \cdot E_e \cdot g_e}{(1 + K_{ii} \cdot g_i)} \right) \cdot g_i + K_{ee} \cdot E_e \cdot g_e}{\left(1 + K_{ee} \cdot g_e - \frac{K_{ie}^2 \cdot g_e \cdot g_i}{(1 + K_{ii} \cdot g_i)} \right)} \end{aligned}$$

With $V_e = \frac{K_{ee} \cdot E_e \cdot g_e}{(1 + K_{ee} \cdot g_e)}$ being the membrane voltage at location e in the absence of inhibitory conductance, we can calculate the voltage change $\frac{\Delta V_e}{V_e} = \frac{V_e - V_e^*}{V_e}$ at location e that is induced by the conductance g_i:

$$\begin{aligned} \frac{\Delta V_e}{V_e} &= 1 - \frac{\frac{K_{ie} \cdot E_i \cdot g_i}{(1 + K_{ii} \cdot g_i)} - \frac{K_{ie}^2 \cdot E_e \cdot g_e \cdot g_i}{(1 + K_{ii} \cdot g_i)} + K_{ee} \cdot E_e \cdot g_e}{1 + K_{ee} \cdot g_e - \frac{K_{ie}^2 \cdot g_e \cdot g_i}{(1 + K_{ii} \cdot g_i)}} \cdot \frac{(1 + K_{ee} \cdot g_e)}{K_{ee} \cdot E_e \cdot g_e} \\ \frac{\Delta V_e}{V_e} &= \frac{-\frac{K_{ie}^2 \cdot g_e \cdot g_i}{(1 + K_{ii} \cdot g_i)} - \frac{K_{ie} \cdot E_i \cdot g_i}{(1 + K_{ii} \cdot g_i)} \cdot \frac{(1 + K_{ee} \cdot g_e)}{K_{ee} \cdot E_e \cdot g_e} + \frac{K_{ie}^2 \cdot E_e \cdot g_e \cdot g_i}{(1 + K_{ii} \cdot g_i)} \cdot \frac{(1 + K_{ee} \cdot g_e)}{K_{ee} \cdot E_e \cdot g_e}}{1 + K_{ee} \cdot g_e - \frac{K_{ie}^2 \cdot g_e \cdot g_i}{(1 + K_{ii} \cdot g_i)}} \\ \frac{\Delta V_e}{V_e} &= \frac{\frac{K_{ie}^2 \cdot g_e \cdot g_i}{(1 + K_{ii} \cdot g_i)} \cdot \frac{1}{K_{ee} \cdot g_e} - \frac{K_{ie} \cdot E_i \cdot g_i}{(1 + K_{ii} \cdot g_i)} \cdot \frac{(1 + K_{ee} \cdot g_e)}{K_{ee} \cdot E_e \cdot g_e}}{1 + K_{ee} \cdot g_e - \frac{K_{ie}^2 \cdot g_e \cdot g_i}{(1 + K_{ii} \cdot g_i)}} \\ \frac{\Delta V_e}{V_e} &= \frac{g_i}{(1 + K_{ii} \cdot g_i)} \cdot \frac{\frac{K_{ie}^2}{K_{ee}} - K_{ie} \cdot E_i \cdot \frac{(1 + K_{ee} \cdot g_e)}{K_{ee} \cdot E_e \cdot g_e}}{1 + K_{ee} \cdot g_e - \frac{K_{ie}^2 \cdot g_e \cdot g_i}{(1 + K_{ii} \cdot g_i)}} \end{aligned}$$

With the "shunted" local input resistance $K^*_{ee} = K_{ee} - \frac{K^2_{ie} \cdot g_i}{(1+K_{ii} \cdot g_i)}$ in the presence of inhibitory conductance g_i at location i (Koch et al., 1990, their equation 11), we obtain:

$$\begin{aligned} \frac{\Delta V_e}{V_e} &= \frac{K_{ii} \cdot g_i}{(1 + K_{ii} \cdot g_i)} \cdot \frac{1}{1 + g_e \cdot K^*_{ee}} \cdot \left(\frac{K^2_{ie}}{K_{ee} \cdot K_{ii}} - \frac{K_{ie} \cdot E_i}{K_{ii} \cdot E_e} \cdot \frac{(1 + K_{ee} \cdot g_e)}{K_{ee} \cdot g_e} \right) \\ \frac{\Delta V_e}{V_e} &= \frac{K_{ii} \cdot g_i}{(1 + K_{ii} \cdot g_i)} \cdot \frac{K^2_{ie}}{K_{ee} \cdot K_{ii}} \cdot \frac{1}{1 + g_e \cdot K^*_{ee}} \cdot \left(1 - \frac{K_{ee} \cdot E_i}{K_{ie} \cdot E_e} \cdot \frac{(1 + K_{ee} \cdot g_e)}{K_{ee} \cdot g_e} \right) \end{aligned}$$

This can be further simplified by

$$SL_i = \frac{K_{ii} \cdot g_i}{(1 + K_{ii} \cdot g_i)}$$

denoting the inhibitory shunt level induced by g_i at location i,

$$SL_e = SL_i \cdot \frac{K^2_{ie}}{K_{ee} \cdot K_{ii}}$$

denoting the inhibitory shunt level induced by g_i at location e, and by defining equivalently an "excitation-induced shunt level"

$$ESL_e = \frac{K_{ee} \cdot g_e}{(1 + K_{ee} \cdot g_e)}$$

induced by g_e at location e:

$$\frac{\Delta V_e}{V_e} = SL_e \cdot \frac{1}{1 + g_e \cdot K^*_{ee}} \cdot \left(1 - \frac{K_{ee}}{K_{ie}} \cdot \frac{E_i}{E_e} \cdot \frac{1}{ESL_e} \right). \tag{12}$$

Subtracting the change in potential that would be induced by g_i with if $g_e = 0$ and $E_i < 0$, the "hyperpolarization-corrected" change in membrane potential can be written as:

$$\frac{\Delta V_e}{V_e} = SL_e \cdot \frac{1}{1 + g_e \cdot K^*_{ee}} + \frac{K_{ee}}{K_{ie}} \cdot \frac{E_i}{E_e} \cdot \frac{SL_e}{ESL_e} \cdot \frac{g_e \cdot K^*_{ee}}{(1 + g_e \cdot K^*_{ee})}.$$

Finally, assuming that the reversal potential of inhibition E_i is at rest, we can simplify to obtain:

$$\frac{\Delta V_e}{V_e} = SL_e \cdot \frac{1}{1 + g_e \cdot K^*_{ee}} \tag{13}$$

In other words, the effective relative reduction $\frac{\Delta V_e}{V_e}$ of excitatory depolarization which is induced by the inhibitory conductance g_i is not only determined by the shunt level SL_e at location e, but additionally by the excitatory conductance g_e itself. If excitatory conductance g_e gets large enough to compete with the local input resistance K^*_{ee}, inhibition is effectively reduced and can even be overcome if $g_e \gg \frac{1}{K^*_{ee}}$. Please note that K^*_{ee} itself depends on g_i, and the necessary amount of excitation g_e needed to compete with inhibition increases with g_i, creating a true "tug-of-war" situation.

If the inhibitory conductance does not reverse at resting membrane potential, the relative reduction $\frac{\Delta V_e}{V_e}$ is strengthened by the factor $\left(1 - \frac{K_{ee}}{K_{ie}} \cdot \frac{E_i}{E_e} \cdot \frac{1}{ESL_e}\right)$, which gets larger

1. the larger $|E_i|$ is in comparison to E_e,
2. the larger the local input resistance K_{ee} is in comparison to the transfer resistance K_{ie}, and
3. the smaller the excitation-induced shunt-level ESL_e.

It is also interesting to note what happens to the depolarization V_i at the location i of inhibition. Due to symmetry, we can write the relative drop in depolarization at i as

$$\frac{\Delta V_i}{V_i} = 1 - \frac{\frac{K_{ie} \cdot E_e \cdot g_e}{(1+K_{ee} \cdot g_e)} - \frac{K_{ie}^2 \cdot E_i \cdot g_i \cdot g_e}{(1+K_{ee} \cdot g_e)} + K_{ii} \cdot E_i \cdot g_i}{1 + K_{ii} \cdot g_i - \frac{K_{ie}^2 \cdot g_i \cdot g_e}{(1+K_{ee} \cdot g_e)}} \cdot \frac{(1 + K_{ee} \cdot g_e)}{K_{ie} \cdot E_e \cdot g_e}$$

which for $E_i = 0$ simplifies to

$$\frac{\Delta V_i}{V_i} = 1 - \frac{1}{1 + K_{ii} \cdot g_i - \frac{K_{ie}^2 \cdot g_i \cdot g_e}{1+K_{ee} \cdot g_e}}.$$

This equation has two interesting marginal cases:

For $K_{ie} \to 0$,

$$\frac{\Delta V_i}{V_i} \to 1 - \frac{1}{1 + K_{ii} \cdot g_i}. \tag{14}$$

For $e \to i$,

$$\begin{aligned} \frac{\Delta V_i}{V_i} &\to 1 - \frac{1}{1 + K_{ii} \cdot g_i - \frac{K_{ii}^2 \cdot g_i \cdot g_e}{1+K_{ii} \cdot g_e}} \\ \frac{\Delta V_i}{V_i} &\to 1 - \frac{1 + K_{ii} \cdot g_e}{1 + K_{ii} \cdot (g_i + g_e)} \end{aligned} \tag{15}$$

This means that for proximal inhibition of very distal events, the inhibition level will be constant (eqn. 14), while for close-by inhibition of events, excitation can overcome inhibition, resulting in the above described tug-of-war situation (eqn. 13, which equals eqn. 15 for $i = e$). The phenomenon that proximal inhibition has a constant effect on (distal) excitation, whereas distal inhibition can be locally overridden by excitation, has been early recognized by Vu and Krasne, 1992 when performing simulations and measurements of EPSP-IPSP interactions in the crayfish lateral giant neuron.

BIBLIOGRAPHY

Abraham NM, Egger V, Shimshek DR, Renden R, Fukunaga I, Sprengel R, Seeburg PH, Klugmann M, Margrie TW, Schaefer AT, Kuner T (2010) Synaptic inhibition in the olfactory bulb accelerates odor discrimination in mice. *Neuron* 65:399–411.

Acsády L, Görcs TJ, Freund TF (1996) Different populations of vasoactive intestinal polypeptide-immunoreactive interneurons are specialized to control pyramidal cells or interneurons in the hippocampus. *Neuroscience* 73:317–34.

Adesnik H, Bruns W, Taniguchi H, Huang ZJ, Scanziani M (2012) A neural circuit for spatial summation in visual cortex. *Nature* 490:226–231.

Aihara T, Abiru Y, Yamazaki Y, Watanabe H, Fukushima Y, Tsukada M (2007) The relation between spike-timing dependent plasticity and Ca2+ dynamics in the hippocampal CA1 network. *Neuroscience* 145:80–87.

Andrews-Zwilling Y, Gillespie AK, Kravitz AV, Nelson AB, Devidze N, Lo I, Yoon SY, Bien-Ly N, Ring K, Zwilling D, Potter GB, Rubenstein JLR, Kreitzer AC, Huang Y (2012) Hilar GABAergic interneuron activity controls spatial learning and memory retrieval. *PloS one* 7:e40555.

Anwar H, Roome CJ, Nedelescu H, Chen W, Kuhn B, De Schutter E (2014) Dendritic diameters affect the spatial variability of intracellular calcium dynamics in computer models. *Front Cell Neurosci* 8:168.

Araya R, Jiang J, Eisenthal KB, Yuste R (2006) The spine neck filters membrane potentials. *PNAS* 103:17961–6.

Ascoli GA, Alonso-Nanclares L, Anderson SA, Barrionuevo G, Benavides-Piccione R, Burkhalter A, Buzsáki G, Cauli B, Defelipe J, Fairén A, Feldmeyer D, Fishell G, Fregnac Y, Freund TF, Gardner D, Gardner EP, Goldberg JH, Helmstaedter M, Hestrin S, Karube F, Kisvarday ZF, Lambolez B, Lewis DA, Marin O, Markram H, Munoz A, Packer A, Petersen CCH, Rockland KS, Rossier J, Rudy B, Somogyi P, Staiger JF, Tamás G, Thomson AM, Toledo-Rodriguez M, Wang Y, West DC, Yuste R (2008) Petilla terminology: nomenclature of features of GABAergic interneurons of the cerebral cortex. *Nat Rev Neurosci* 9:557–568.

Atallah BV, Bruns W, Carandini M, Scanziani M (2012) Parvalbumin-expressing interneurons linearly transform cortical responses to visual stimuli. *Neuron* 73:159–170.

Bar-Ilan L, Gidon A, Segev I (2012) The role of dendritic inhibition in shaping the plasticity of excitatory synapses. *Front Neural Circuits* 6:118.

Baroncelli L, Braschi C, Spolidoro M, Begenisic T, Maffei L, Sale A (2011) Brain plasticity and disease: a matter of inhibition. *Neural Plast* 2011:286073.

Bartos M, Vida I, Frotscher M, Geiger JRP, Jonas P (2001) Rapid signaling at inhibitory synapses in a dentate gyrus interneuron network. *J Neurosci* 21:2687–2698.

Battaglia D, Karagiannis A, Gallopin T, Gutch HW, Cauli B (2013) Beyond the frontiers of neuronal types. *Front Neural Circuits* 7:13.

Beaulieu C, Kisvarday Z, Somogyi P, Cynader M, Cowey A (1992) Quantitative distribution of GABA-immunopositive and -immunonegative neurons and synapses in the monkey striate cortex (area 17). *Cereb Cortex* 2:295–309.

Ben-Ari Y, Gaiarsa JL, Tyzio R, Khazipov R (2007) Gaba: a pioneer transmitter that excites immature neurons and generates primitive oscillations. *Physiol Rev* 87:1215–84.

Bi GQ, Poo MM (1998) Synaptic modifications in cultured hippocampal neurons: dependence on spike timing, synaptic strength, and postsynaptic cell type. *J Neurosci* 18:10464–72.

Bishop D, Nikic I, Brinkoetter M, Knecht S, Potz S, Kerschensteiner M, Misgeld T (2011) Near-infrared branding efficiently correlates light and electron microscopy. *Nat Methods* 8:568–70.

Blackman AV, Abrahamsson T, Costa RP, Lalanne T, Sjöström PJ (2013) Target-cell-specific short-term plasticity in local circuits. *Front Synaptic Neurosci* 5:11.

Bouhours B, Trigo FF, Marty A (2011) Somatic depolarization enhances GABA release in cerebellar interneurons via a calcium/protein kinase C pathway. *J Neurosci* 31:5804–15.

Bourne JN, Harris KM (2011) Coordination of size and number of excitatory and inhibitory synapses results in a balanced structural plasticity along mature hippocampal CA1 dendrites during LTP. *Hippocampus* 21:354–73.

Branco T, Häusser M (2010) The single dendritic branch as a fundamental functional unit in the nervous system. *Curr Opin Neurobiol* 20:494–502.

Breton JD, Stuart GJ (2012) Somatic and dendritic GABA(B) receptors regulate neuronal excitability via different mechanisms. *J Neurophysiol* 108:2810–8.

Brickley SG, Mody I (2012) Extrasynaptic GABA(A) receptors: their function in the CNS and implications for disease. *Neuron* 73:23–34.

Brown TH, Fricke RA, Perkel DH (1981) Passive electrical constants in three classes of hippocampal neurons. *J Neurophysiol* 46:812–27.

Burger RM, Fukui I, Ohmori H, Rubel EW (2011) Inhibition in the balance: binaurally coupled inhibitory feedback in sound localization circuitry. *J Neurophysiol* 106:4–14.

Butt SJB, Fuccillo M, Nery S, Noctor S, Kriegstein A, Corbin JG, Fishell G (2005) The temporal and spatial origins of cortical interneurons predict their physiological subtype. *Neuron* 48:591–604.

Buzsáki G, Penttonen M, Nadasdy Z, Bragin A (1996) Pattern and inhibition-dependent invasion of pyramidal cell dendrites by fast spikes in the hippocampus in vivo. *PNAS* 93:9921–9925.

Caeser M, Bonhoeffer T, Bolz J (1989) Cellular organization and development of slice cultures from rat visual cortex. *Exp Brain Res* 77:234–44.

Caporale N, Dan Y (2008) Spike timing-dependent plasticity: a Hebbian learning rule. *Annu Rev Neurosci* 31:25–46.

Cardin JA, Carlen M, Meletis K, Knoblich U, Zhang F, Deisseroth K, Tsai LH, Moore CI (2009) Driving fast-spiking cells induces gamma rhythm and controls sensory responses. *Nature* 459:663–7.

Cardin JA (2012) Dissecting local circuits in vivo: integrated optogenetic and electrophysiology approaches for exploring inhibitory regulation of cortical activity. *J Physiol* 106:104–111.

Carnevale NT, Hines ML (2006) The NEURON Book. *(Cambridge, UK: Cambridge University Press)* .

Chalifoux JR, Carter AG (2010) Gabab receptors modulate nmda receptor calcium signals in dendritic spines. *Neuron* 66:101–13.

Chalifoux JR, Carter AG (2011) GABAB receptor modulation of voltage-sensitive calcium channels in spines and dendrites. *J Neurosci* 31:4221–32.

Chamberland S, Topolnik L (2012) Inhibitory control of hippocampal inhibitory neurons. *Front Neurosci* 6:165.

Chen JL, Lin WC, Cha JW, So PT, Kubota Y, Nedivi E (2011) Structural basis for the role of inhibition in facilitating adult brain plasticity. *Nat Neurosci* 14:587–94.

Chen JL, Villa KL, Cha JW, So PT, Kubota Y, Nedivi E (2012) Clustered dynamics of inhibitory synapses and dendritic spines in the adult neocortex. *Neuron* 74:361–73.

Chiu CQ, Lur G, Morse TM, Carnevale NT, Ellis-Davies GC, Higley MJ (2013) Compartmentalization of GABAergic inhibition by dendritic spines. *Science* 340:759–62.

Christie BR, Eliot LS, Ito K, Miyakawa H, Johnston D (1995) Different Ca2+ channels in soma and dendrites of hippocampal pyramidal neurons mediate spike-induced Ca2+ influx. *J Neurophysiol* 73:2553–7.

Chvanov M, Belan P, Teslenko V, Mel'nik I (1998) Glutamate-induced suppression of inhibitory synaptic transmission in cultivated hippocampal neurons. *Neurophysiology* 30:279–284.

Ciceri G, Dehorter N, Sols I, Huang ZJ, Maravall M, Marin O (2013) Lineage-specific laminar organization of cortical GABAergic interneurons. *Nat Neurosci* 16:1199–1210.

Cichon J, Gan WB (2015) Branch-specific dendritic Ca(2+) spikes cause persistent synaptic plasticity. *Nature* 520:180–5.

Cobb SR, Buhl EH, Halasy K, Paulsen O, Somogyi P (1995) Synchronization of neuronal activity in hippocampus by individual GABAergic interneurons. *Nature* 378:75–8.

Coghlan S, Horder J, Inkster B, Mendez MA, Murphy DG, Nutt DJ (2012) GABA system dysfunction in autism and related disorders: from synapse to symptoms. *Neurosci Biobehav Rev* 36:2044–55.

Colgan LA, Yasuda R (2014) Plasticity of dendritic spines: subcompartmentalization of signaling. *Annu Rev Physiol* 76:365–385.

Couey JJ, Meredith RM, Spijker S, Poorthuis RB, Smit AB, Brussaard AB, Mansvelder HD (2007) Distributed network actions by nicotine increase the threshold for spike-timing-dependent plasticity in prefrontal cortex. *Neuron* 54:73–87.

Cummings JA, Mulkey RM, Nicoll RA, Malenka RC (1996) Ca2+ signaling requirements for long-term depression in the hippocampus. *Neuron* 16:825–833.

Cutsuridis V (2011) GABA inhibition modulates NMDA-R mediated spike timing dependent plasticity (STDP) in a biophysical model. *Neural Netw* 24:29–42.

Cutsuridis V, Hasselmo M (2012) GABAergic contributions to gating, timing, and phase precession of hippocampal neuronal activity during theta oscillations. *Hippocampus* 22:1597–1621.

De Simoni A, Griesinger CB, Edwards FA (2003) Development of rat CA1 neurones in acute versus organotypic slices: role of experience in synaptic morphology and activity. *J Physiol* 550:135–147.

DeFelipe J, López-Cruz PL, Benavides-Piccione R, Bielza C, Larrañaga P, Anderson S, Burkhalter A, Cauli B, Fairén A, Feldmeyer D, Fishell G, Fitzpatrick D, Freund TF, González-Burgos G, Hestrin S, Hill S, Hof PR, Huang J, Jones EG, Kawaguchi Y, Kisvarday Z, Kubota Y, Lewis DA, Marin O, Markram H, McBain CJ, Meyer HS, Monyer H, Nelson SB, Rockland K, Rossier J, Rubenstein JLR, Rudy B, Scanziani M, Shepherd GM, Sherwood CC, Staiger JF, Tamás G, Thomson A, Wang Y, Yuste R, Ascoli GA (2013) New insights into the classification and nomenclature of cortical GABAergic interneurons. *Nat Rev Neurosci* 14:202–216.

Dehay C, Douglas RJ, Martin KA, Nelson C (1991) Excitation by geniculocortical synapses is not 'vetoed' at the level of dendritic spines in cat visual cortex. *J Physiol* 440:723–734.

Dichter MA, Ayala GF (1987) Cellular mechanisms of epilepsy: a status report. *Science* 237:157–164.

Donato F, Chowdhury A, Lahr M, Caroni P (2015) Early- and late-born parvalbumin basket cell subpopulations exhibiting distinct regulation and roles in learning. *Neuron* 85:770–86.

Donato F, Rompani SB, Caroni P (2013) Parvalbumin-expressing basket-cell network plasticity induced by experience regulates adult learning. *Nature* 504:272–276.

Fanselow EE, Connors BW (2010) The roles of somatostatin-expressing (GIN) and fast-spiking inhibitory interneurons in UP-DOWN states of mouse neocortex. *J Neurophysiol* 104:596–606.

Farrant M, Nusser Z (2005) Variations on an inhibitory theme: phasic and tonic activation of GABA(A) receptors. *Nat Rev Neurosci* 6:215–229.

Feldman DE (2012) The spike-timing dependence of plasticity. *Neuron* 75:556–571.

Ferster D, Jagadeesh B (1992) EPSP-IPSP interactions in cat visual cortex studied with in vivo whole-cell patch recording. *J Neurosci* 12:1262–1274.

Fiala JC (2005) Reconstruct: a free editor for serial section microscopy. *J Microsc* 218:52–61.

Fino E, Araya R, Peterka DS, Salierno M, Etchenique R, Yuste R (2009) RuBi-Glutamate: Two-Photon and Visible-Light Photoactivation of Neurons and Dendritic spines. *Front Neural Circuits* 3:2.

Frazier CJ, Rollins YD, Breese CR, Leonard S, Freedman R, Dunwiddie TV (1998) Acetylcholine activates an alpha-bungarotoxin-sensitive nicotinic current in rat hippocampal interneurons, but not pyramidal cells. *J Neurosci* 18:1187–1195.

Freund TF, Buzsáki G (1996) Interneurons of the hippocampus. *Hippocampus* 6:347–470.

Freund TF, Gulyás AI, Acsády L, Gorcs T, Tóth K (1990) Serotonergic control of the hippocampus via local inhibitory interneurons. *PNAS* 87:8501–8505.

Freund TF, Katona I (2007) Perisomatic inhibition. *Neuron* 56:33–42.

Froemke RC, Poo MM, Dan Y (2005) Spike-timing-dependent synaptic plasticity depends on dendritic location. *Nature* 434:221–225.

Gähwiler BH (1981) Organotypic monolayer cultures of nervous tissue. *J Neurosci Meth* 4:329–342.

Gähwiler BH, Capogna M, Debanne D, McKinney RA, Thompson SM (1997) Organotypic slice cultures: a technique has come of age. *Trends Neurosci* 20:471–477.

Gasparini S, Losonczy A, Chen X, Johnston D, Magee JC (2007) Associative pairing enhances action potential back-propagation in radial oblique branches of CA1 pyramidal neurons. *J Physiol* 580:787–800.

Gentet LJ, Kremer Y, Taniguchi H, Huang ZJ, Staiger JF, Petersen CC (2012) Unique functional properties of somatostatin-expressing gabaergic neurons in mouse barrel cortex. *Nat Neurosci* 15:607–12.

Gidon A, Segev I (2012) Principles governing the operation of synaptic inhibition in dendrites. *Neuron* 75:330–41.

Gómez González JF, Mel BW, Poirazi P (2011) Distinguishing Linear vs. Non-Linear Integration in CA1 Radial Oblique Dendrites: It's about Time. *Front Comput Neurosci* 5:44.

Haider B, Häusser M, Carandini M (2013) Inhibition dominates sensory responses in the awake cortex. *Nature* 493:97–100.

Hao J, Wang XD, Dan Y, Poo MM, Zhang XH (2009) An arithmetic rule for spatial summation of excitatory and inhibitory inputs in pyramidal neurons. *PNAS* 106:21906–11.

Harnett MT, Makara JK, Spruston N, Kath WL, Magee JC (2012) Synaptic amplification by dendritic spines enhances input cooperativity. *Nature* 491:599–602.

Harvey CD, Svoboda K (2007) Locally dynamic synaptic learning rules in pyramidal neuron dendrites. *Nature* 450:1195–1200.

Hayama T, Noguchi J, Watanabe S, Takahashi N, Hayashi-Takagi A, Ellis-Davies GC, Matsuzaki M, Kasai H (2013) GABA promotes the competitive selection of dendritic spines by controlling local Ca2+ signaling. *Nat Neurosci* 16:1409–16.

Hebb D (1949) *The organization of behavior: A neuropsychological theory.* John Wiley and Sons, Inc., New York.

Hensch TK (2005) Critical period plasticity in local cortical circuits. *Nat Rev Neurosci* 6:877–888.

Herman MA, Jahr CE (2007) Extracellular glutamate concentration in hippocampal slice. *J Neurosci* 27:9736–9741.

Holt GR, Koch C (1997) Shunting inhibition does not have a divisive effect on firing rates. *Neural Comput* 9:1001–1013.

Howard A, Tamas G, Soltesz I (2005) Lighting the chandelier: new vistas for axo-axonic cells. *Trends Neurosci* 28:310–6.

Isaacson JS, Scanziani M (2011) How inhibition shapes cortical activity. *Neuron* 72:231–243.

Jack JJB, Noble D, Tsien RW (1975) *Electric current flow in excitable cells.* Clarendon Press, Oxford.

Jadi M, Polsky A, Schiller J, Mel BW (2012) Location-dependent effects of inhibition on local spiking in pyramidal neuron dendrites. *PLoS Comput Biol* 8:e1002550.

Jedlicka P, Deller T, Gutkin BS, Backus KH (2011) Activity-dependent intracellular chloride accumulation and diffusion controls GABA(A) receptor-mediated synaptic transmission. *Hippocampus* 21:885–98.

Ji D, Lape R, Dani JA (2001) Timing and location of nicotinic activity enhances or depresses hippocampal synaptic plasticity. *Neuron* 31:131–141.

Jones EG, Powell TP (1969) Morphological variations in the dendritic spines of the neocortex. *J Cell Sci* 5:509–29.

Kanemoto Y, Matsuzaki M, Morita S, Hayama T, Noguchi J, Senda N, Momotake A, Arai T, Kasai H (2011) Spatial distributions of GABA receptors and local inhibition of Ca2+ transients studied with GABA uncaging in the dendrites of CA1 pyramidal neurons. *PLoS One* 6:e22652.

Kantevari S, Matsuzaki M, Kanemoto Y, Kasai H, Ellis-Davies GCR (2010) Two-color, two-photon uncaging of glutamate and GABA. *Nat Methods* 7:123–125.

Katona I, Sperlágh B, Sík A, Käfalvi A, Vizi ES, Mackie K, Freund TF (1999) Presynaptically located CB1 cannabinoid receptors regulate GABA release from axon terminals of specific hippocampal interneurons. *J Neurosci* 19:4544–4558.

Kim HG, Beierlein M, Connors BW (1995) Inhibitory control of excitable dendrites in neocortex. *J Neurophysiol* 74:1810–4.

Klausberger T (2009) GABAergic interneurons targeting dendrites of pyramidal cells in the CA1 area of the hippocampus. *Eur J Neurosci* 30:947–57.

Klonoff DC (2005) Pyruvate therapy for severe hypoglycemia. *Diabetes Technol Ther* 7:583–6.

Knott GW, Holtmaat A, Trachtenberg JT, Svoboda K, Welker E (2009) A protocol for preparing GFP-labeled neurons previously imaged in vivo and in slice preparations for light and electron microscopic analysis. *Nat Protoc* 4:1145–56.

Kobayashi T, Ebihara S, Ishii K, Kobayashi T, Nishijima M, Endo S, Takaku A, Sakagami H, Kondo H, Tashiro F, Miyazaki Ji, Obata K, Tamura S, Yanagawa Y (2003) Structural and functional characterization of mouse glutamate decarboxylase 67 gene promoter. *Biochim Biophys* 1628:156–168.

Koch C, Douglas R, Wehmeier U (1990) Visibility of synaptically induced conductance changes: theory and simulations of anatomically characterized cortical pyramidal cells. *J Neurosci* 10:1728–1744.

Koch C, Poggio T, Torre V (1982) Retinal ganglion cells: a functional interpretation of dendritic morphology. *PNAS* 298:227–263.

Koch C, Poggio T, Torre V (1983) Nonlinear interactions in a dendritic tree: localization, timing, and role in information processing. *PNAS* 80:2799–802.

Koch C (1998) *Biophysics of Computation: Information Processing in Single Neurons (Computational Neuroscience)* Oxford University Press, 1 edition.

Kubota Y, Hatada S, Kondo S, Karube F, Kawaguchi Y (2007) Neocortical inhibitory terminals innervate dendritic spines targeted by thalamocortical afferents. *J Neurosci* 27:1139–1150.

Kuhlman SJ, Olivas ND, Tring E, Ikrar T, Xu X, Trachtenberg JT (2013) A disinhibitory microcircuit initiates critical-period plasticity in the visual cortex. *Nature* 501:543–546.

Kwon HB, Sabatini BL (2011) Glutamate induces de novo growth of functional spines in developing cortex. *Nature* 474:100–104.

Larkum ME, Zhu JJ, Sakmann B (1999) A new cellular mechanism for coupling inputs arriving at different cortical layers. *Nature* 398:338–41.

Ledri M, Sorensen AT, Erdelyi F, Szabo G, Kokaia M (2011) Tuning afferent synapses of hippocampal interneurons by neuropeptide Y. *Hippocampus* 21:198–211.

Lee SH, Kwan AC, Zhang S, Phoumthipphavong V, Flannery JG, Masmanidis SC, Taniguchi H, Huang ZJ, Zhang F, Boyden ES, Deisseroth K, Dan Y (2012) Activation of specific interneurons improves V1 feature selectivity and visual perception. *Nature* 488:379–383.

Letzkus JJ, Wolff SBE, Meyer EMM, Tovote P, Courtin J, Herry C, Lüthi A (2011) A disinhibitory microcircuit for associative fear learning in the auditory cortex. *Nature* 480:331–335.

Levelt CN, Hübener M (2012) Critical-period plasticity in the visual cortex. *Annu Rev Neurosci* 35:309–330.

Lewis DA, Hashimoto T, Volk DW (2005) Cortical inhibitory neurons and schizophrenia. *Nat Rev Neurosci* 6:312–24.

Liu G (2004) Local structural balance and functional interaction of excitatory and inhibitory synapses in hippocampal dendrites. *Nat Neurosci* 7:373–9.

London M, Häusser M (2005) Dendritic computation. *Annu Rev Neurosci* 28:503–532.

López-Bendito G, Sturgess K, Erdélyi F, Szabó G, Molnár Z, Paulsen O (2004) Preferential origin and layer destination of GAD65-GFP cortical interneurons. *Cereb Cortex* 14:1122–33.

Losonczy A, Makara JK, Magee JC (2008) Compartmentalized dendritic plasticity and input feature storage in neurons. *Nature* 452:436–41.

Lovett-Barron M, Turi GF, Kaifosh P, Lee PH, Bolze F, Sun XH, Nicoud JF, Zemelman BV, Sternson SM, Losonczy A (2012) Regulation of neuronal input transformations by tunable dendritic inhibition. *Nat Neurosci* 15:423–30, S1–3.

Lowe G (2002) Inhibition of backpropagating action potentials in mitral cell secondary dendrites. *J Neurophysiol* 88:64–85.

Makinae K, Kobayashi T, Kobayashi T, Shinkawa H, Sakagami H, Kondo H, Tashiro F, Miyazaki J, Obata K, Tamura S, Yanagawa Y (2000) Structure of the mouse glutamate decarboxylase 65 gene and its promoter: preferential expression of its promoter in the GABAergic neurons of transgenic mice. *J Neurochem* 75:1429–1437.

Mann EO, Paulsen O (2007) Role of GABAergic inhibition in hippocampal network oscillations. *Trends Neurosci* 30:343–9.

Markram H, Toledo-Rodriguez M, Wang Y, Gupta A, Silberberg G, Wu C (2004) Interneurons of the neocortical inhibitory system. *Nat Rev Neurosci* 5:793–807.

Marlin JJ, Carter AG (2014) GABA-A receptor inhibition of local calcium signaling in spines and dendrites. *J Neurosci* 34:15898–911.

Matsuzaki M, Honkura N, Ellis-Davies GCR, Kasai H (2004) Structural basis of long-term potentiation in single dendritic spines. *Nature* 429:761–766.

McAllister AK (2000) Biolistic transfection of neurons. *Science's STKE* 2000:pl1.

Megías M, Emri Z, Freund TF, Gulyás AI (2001) Total number and distribution of inhibitory and excitatory synapses on hippocampal CA1 pyramidal cells. *Neuroscience* 102:527–40.

Meredith RM, Floyer-Lea AM, Paulsen O (2003) Maturation of long-term potentiation induction rules in rodent hippocampus: role of GABAergic inhibition. *J Neurosci* 23:11142–6.

Miles R, Tóth K, Gulyás AI, Hájos N, Freund TF (1996) Differences between somatic and dendritic inhibition in the hippocampus. *Neuron* 16:815–23.

Miyoshi G, Hjerling-Leffler J, Karayannis T, Sousa VH, Butt SJ, Battiste J, Johnson JE, Machold RP, Fishell G (2010) Genetic fate mapping reveals that the caudal ganglionic eminence produces a large and diverse population of superficial cortical interneurons. *J Neurosci* 30:1582–94.

Müller C, Beck H, Coulter D, Remy S (2012) Inhibitory control of linear and supralinear dendritic excitation in CA1 pyramidal neurons. *Neuron* 75:851–64.

Muller D, Buchs PA, Stoppini L (1993) Time course of synaptic development in hippocampal organotypic cultures. *Brain Res Dev Brain Res* 71:93–100.

Müllner FE, Wierenga CJ, Bonhoeffer T (2015) Precision of Inhibition: dendritic inhibition by individual GABAergic synapses on hippocampal pyramidal cells is confined in space and time. *Neuron* 87:576–89.

Murayama M, Pérez-Garci E, Nevian T, Bock T, Senn W, Larkum ME (2009) Dendritic encoding of sensory stimuli controlled by deep cortical interneurons. *Nature* 457:1137–41.

Murnick JG, Dubé G, Krupa B, Liu G (2002) High-resolution iontophoresis for single-synapse stimulation. *J Neurosci Meth* 116:65–75.

Naundorf B, Wolf F, Volgushev M (2006) Unique features of action potential initiation in cortical neurons. *Nature* 440:1060–1063.

Nevian T, Sakmann B (2006) Spine Ca2+ signaling in spike-timing-dependent plasticity. *J Neurosci* 26:11001–13.

Niell CM (2015) Cell types, circuits, and receptive fields in the mouse visual cortex. *Annu Rev Neurosci* 38:413–431.

Nishiyama M, Togashi K, Aihara T, Hong K (2010) GABAergic activities control spike timing- and frequency-dependent long-term depression at hippocampal excitatory synapses. *Front Synaptic Neurosci* 2:22.

Oliva AAJ, Jiang M, Lam T, Smith KL, Swann JW (2000) Novel hippocampal interneuronal subtypes identified using transgenic mice that express green fluorescent protein in GABAergic interneurons. *J Neurosci* 20:3354–3368.

Olsen RW, Sieghart W (2009) GABA A receptors: subtypes provide diversity of function and pharmacology. *Neuropharmacol* 56:141–148.

Oron D, Papagiakoumou E, Anselmi F, Emiliani V (2012) Two-photon optogenetics. *Prog Brain Res* 196:119–143.

Paille V, Fino E, Du K, Morera-Herreras T, Perez S, Kotaleski JH, Venance L (2013) GABAergic circuits control spike-timing-dependent plasticity. *J Neurosci* 33:9353–9363.

Palmer LM, Stuart GJ (2009) Membrane potential changes in dendritic spines during action potentials and synaptic input. *J Neurosci* 29:6897–903.

Park S, Kwag J (2012) Dendritic-targeting interneuron controls spike timing of hippocampal CA1 pyramidal neuron via activation of I(h). *Neurosci Lett* 523:9–14.

Paulsen O, Moser EI (1998) A model of hippocampal memory encoding and retrieval: GABAergic control of synaptic plasticity. *Trends Neurosci* 21:273–278.

Pérez-Garci E, Gassmann M, Bettler B, Larkum ME (2006) The GABAB1b isoform mediates long-lasting inhibition of dendritic Ca2+ spikes in layer 5 somatosensory pyramidal neurons. *Neuron* 50:603–16.

Pérez-Garci E, Larkum ME, Nevian T (2013) Inhibition of dendritic Ca2+ spikes by GABAB receptors in cortical pyramidal neurons is mediated by a direct Gi/o-beta-subunit interaction with Cav1 channels. *J Physiol* 591:1599–612.

Pfeffer CK, Xue M, He M, Huang ZJ, Scanziani M (2013) Inhibition of inhibition in visual cortex: the logic of connections between molecularly distinct interneurons. *Nat Neurosci* 16:1068–1076.

Poirazi P, Brannon T, Mel BW (2003a) Arithmetic of subthreshold synaptic summation in a model CA1 pyramidal cell. *Neuron* 37:977–87.

Poirazi P, Brannon T, Mel BW (2003b) Pyramidal neuron as two-layer neural network. *Neuron* 37:989–99.

Popovic MA, Gao X, Carnevale NT, Zecevic D (2014) Cortical dendritic spine heads are not electrically isolated by the spine neck from membrane potential signals in parent dendrites. *Cereb Cortex* 24:385–95.

Pouille F, Scanziani M (2001) Enforcement of temporal fidelity in pyramidal cells by somatic feed-forward inhibition. *Science* 293:1159–1163.

Pouille F, Scanziani M (2004) Routing of spike series by dynamic circuits in the hippocampus. *Nature* 429:717–723.

Qian N, Sejnowski TJ (1990) When is an inhibitory synapse effective? *PNAS* 87:8145–9.

Qian N, Sejnowski T (1989) An electro-diffusion model for computing membrane potentials and ionic concentrations in branching dendrites, spines and axons. *Biological Cybernetics* 62:1–15.

Rall W, Rinzel J (1973) Branch input resistance and steady attenuation for input to one branch of a dendritic neuron model. *Biophys J* 13:648–87.

Rinke I, Artmann J, Stein V (2010) ClC-2 voltage-gated channels constitute part of the background conductance and assist chloride extrusion. *J Neurosci* 30:4776–4786.

Rinzel J, Rall W (1974) Transient response in a dendritic neuron model for current injected at one branch. *Biophys J* 14:759–90.

Royer S, Zemelman BV, Losonczy A, Kim J, Chance F, Magee JC, Buzsáki G (2012) Control of timing, rate and bursts of hippocampal place cells by dendritic and somatic inhibition. *Nat Neurosci* 15:769–75.

Sabatini BL, Svoboda K (2000) Analysis of calcium channels in single spines using optical fluctuation analysis. *Nature* 408:589–93.

Scheuss V, Bonhoeffer T (2014) Function of dendritic spines on hippocampal inhibitory neurons. *Cereb Cortex* 24:3142–53.

Schoenenberger P, Scharer YPZ, Oertner TG (2011) Channelrhodopsin as a tool to investigate synaptic transmission and plasticity. *Exp Physiol* 96:34–39.

Segev I, Parnas I (1983) Synaptic integration mechanisms. Theoretical and experimental investigation of temporal postsynaptic interactions between excitatory and inhibitory inputs. *Biophys J* 41:41–50.

Seybold BA, Stanco A, Cho KKA, Potter GB, Kim C, Sohal VS, Rubenstein JLR, Schreiner CE (2012) Chronic reduction in inhibition reduces receptive field size in mouse auditory cortex. *PNAS* 109:13829–13834.

Shouval HZ, Bear MF, Cooper LN (2002) A unified model of NMDA receptor-dependent bidirectional synaptic plasticity. *PNAS* 99:10831–10836.

Sivyer B, Williams SR (2013) Direction selectivity is computed by active dendritic integration in retinal ganglion cells. *Nat Neurosci* 16:1848–1856.

Sjöström PJ, Nelson SB (2002) Spike timing, calcium signals and synaptic plasticity. *Curr Opin Neurobiol* 12:305–314.

Somogyi P, Klausberger T (2005) Defined types of cortical interneurone structure space and spike timing in the hippocampus. *J Physiol* 562:9–26.

Sparta DR, Hovelso N, Mason AO, Kantak PA, Ung RL, Decot HK, Stuber GD (2014) Activation of prefrontal cortical parvalbumin interneurons facilitates extinction of reward-seeking behavior. *J Neurosci* 34:3699–3705.

Stanley EM, Fadel JR, Mott DD (2012) Interneuron loss reduces dendritic inhibition and GABA release in hippocampus of aged rats. *Neurobiol Aging* 33:431.e1–13.

Stokes CC, Isaacson JS (2010) From dendrite to soma: dynamic routing of inhibition by complementary interneuron microcircuits in olfactory cortex. *Neuron* 67:452–65.

Stokes CC, Teeter CM, Isaacson JS (2014) Single dendrite-targeting interneurons generate branch-specific inhibition. *Front Neural Circuits* 8:139.

Stoppini L, Buchs PA, Muller D (1991) A simple method for organotypic cultures of nervous tissue. *J Neurosci Meth* 37:173–82.

Streit P, Thompson SM, Gähwiler BH (1989) Anatomical and Physiological Properties of GABAergic Neurotransmission in Organotypic Slice Cultures of Rat Hippocampus. *Eur J Neurosci* 1:603–615.

Stuart GJ, Häusser M (2001) Dendritic coincidence detection of EPSPs and action potentials. *Nat Neurosci* 4:63–71.

Svoboda K, Tank DW, Denk W (1996) Direct measurement of coupling between dendritic spines and shafts. *Science* 272:716–9.

Tamás G, Szabadics J, Lörincz A, Somogyi P (2004) Input and frequency-specific entrainment of postsynaptic firing by IPSPs of perisomatic or dendritic origin. *Eur J Neurosci* 20:2681–2690.

Tanaka JI, Horiike Y, Matsuzaki M, Miyazaki T, Ellis-Davies GCR, Kasai H (2008) Protein synthesis and neurotrophin-dependent structural plasticity of single dendritic spines. *Science* 319:1683–1687.

Taniguchi H (2014) Genetic dissection of GABAergic neural circuits in mouse neocortex. *Front Cell Neurosci* 8:8.

Tønnesen J, Katona G, Rózsa B, Nägerl UV (2014) Spine neck plasticity regulates compartmentalization of synapses. *Nat Neurosci* 17:678–85.

Traynelis SF (1998) Software-based correction of single compartment series resistance errors. *J Neurosci Meth* 86:25–34.

Tricoire L, Pelkey KA, Erkkila BE, Jeffries BW, Yuan X, McBain CJ (2011) A blueprint for the spatiotemporal origins of mouse hippocampal interneuron diversity. *J Neurosci* 31:10948–10970.

Trouche S, Sasaki JM, Tu T, Reijmers LG (2013) Fear extinction causes target-specific remodeling of perisomatic inhibitory synapses. *Neuron* 80:1054–1065.

Tsubokawa H, Ross WN (1996) IPSPs modulate spike backpropagation and associated [Ca2+]i changes in the dendrites of hippocampal CA1 pyramidal neurons. *J Neurophysiol* 76:2896–906.

Tsukada M, Aihara T, Kobayashi Y, Shimazaki H (2005) Spatial analysis of spike-timing-dependent LTP and LTD in the CA1 area of hippocampal slices using optical imaging. *Hippocampus* 15:104–9.

Tyan L, Chamberland S, Magnin E, Camire O, Francavilla R, David LS, Deisseroth K, Topolnik L (2014) Dendritic inhibition provided by interneuron-specific cells controls the firing rate and timing of the hippocampal feedback inhibitory circuitry. *J Neurosci* 34:4534–4547.

van Versendaal D, Rajendran R, Saiepour MH, Klooster J, Smit-Rigter L, Sommeijer JP, De Zeeuw CI, Hofer SB, Heimel JA, Levelt CN (2012) Elimination of inhibitory synapses is a major component of adult ocular dominance plasticity. *Neuron* 74:374–83.

Vu ET, Krasne FB (1992) Evidence for a computational distinction between proximal and distal neuronal inhibition. *Science* 255:1710–2.

Waters J, Schaefer A, Sakmann B (2005) Backpropagating action potentials in neurones: measurement, mechanisms and potential functions. *Prog Biophys Mol Biol* 87:145–170.

Wierenga CJ, Becker N, Bonhoeffer T (2008) GABAergic synapses are formed without the involvement of dendritic protrusions. *Nat Neurosci* 11:1044–52.

Wierenga CJ, Müllner FE, Rinke I, Keck T, Stein V, Bonhoeffer T (2010) Molecular and electrophysiological characterization of GFP-expressing CA1 interneurons in GAD65-GFP mice. *PLoS One* 5:e15915.

Wigström H, Gustafsson B (1983) Facilitated induction of hippocampal long-lasting potentiation during blockade of inhibition. *Nature* 301:603–4.

Willadt S, Nenniger M, Vogt KE (2013) Hippocampal feedforward inhibition focuses excitatory synaptic signals into distinct dendritic compartments. *PloS one* 8:e80984.

Wilson NR, Runyan CA, Wang FL, Sur M (2012) Division and subtraction by distinct cortical inhibitory networks in vivo. *Nature* 488:343–348.

Wolff SBE, Grundemann J, Tovote P, Krabbe S, Jacobson GA, Muller C, Herry C, Ehrlich I, Friedrich RW, Letzkus JJ, Lüthi A (2014) Amygdala interneuron subtypes control fear learning through disinhibition. *Nature* 509:453–458.

Wonders CP, Anderson SA (2006) The origin and specification of cortical interneurons. *Nat Rev Neurosci* 7:687–696.

Wu X, Huang L, Wu Z, Zhang C, Jiang D, Bai Y, Wang Y, Chen G (2013) Homeostatic competition between phasic and tonic inhibition. *J Biol Chem* 288:25053–25065.

Xiong W, Chen WR (2002) Dynamic gating of spike propagation in the mitral cell lateral dendrites. *Neuron* 34:115–126.

Xu C, Zhao Mx, Poo MM, Zhang Xh (2008) GABA(B) receptor activation mediates frequency-dependent plasticity of developing GABAergic synapses. *Nat Neurosci* 11:1410–1418.

Yang Y, Wang Xb, Frerking M, Zhou Q (2008) Spine expansion and stabilization associated with long-term potentiation. *J Neurosci* 28:5740–5751.

Yasuda R, Nimchinsky EA, Scheuss V, Pologruto TA, Oertner TG, Sabatini BL, Svoboda K (2004) Imaging calcium concentration dynamics in small neuronal compartments. *Science's STKE* 2004:pl5.

Yizhar O, Fenno LE, Prigge M, Schneider F, Davidson TJ, O'Shea DJ, Sohal VS, Goshen I, Finkelstein J, Paz JT, Stehfest K, Fudim R, Ramakrishnan C, Huguenard JR, Hegemann P, Deisseroth K (2011) Neocortical excitation/inhibition balance in information processing and social dysfunction. *Nature* 477:171–178.

Yonehara K, Balint K, Noda M, Nagel G, Bamberg E, Roska B (2011) Spatially asymmetric reorganization of inhibition establishes a motion-sensitive circuit. *Nature* 469:407–410.

Zhang YP, Oertner TG (2007) Optical induction of synaptic plasticity using a light-sensitive channel. *Nat Methods* 4:139–141.

Zhou M, Liang F, Xiong XR, Li L, Li H, Xiao Z, Tao HW, Zhang LI (2014) Scaling down of balanced excitation and inhibition by active behavioral states in auditory cortex. *Nat Neurosci* 17:841–850.

Zhou M, Tao HW, Zhang LI (2012) Generation of intensity selectivity by differential synaptic tuning: fast-saturating excitation but slow-saturating inhibition. *J Neurosci* 32:18068–18078.

Zito K, Scheuss V, Knott G, Hill T, Svoboda K (2009) Rapid functional maturation of nascent dendritic spines. *Neuron* 61:247–258.

LIST OF SCIENTIFIC PUBLICATIONS

Müllner FE*, Wierenga CJ, Bonhoeffer T. *Precision of inhibition: Dendritic inhibition by individual GABAergic synapses on hippocampal pyramidal cells is confined in space and time.* Neuron 2015 Aug 5; 87(3):576-89. *corresponding author

Wierenga CJ, **Müllner FE**, Rinke I, Keck T, Stein V, Bonhoeffer T. *Molecular and electrophysiological characterization of GFP-expressing CA1 interneurons in GAD65-GFP mice.* PLoS One 2010 Dec 31; 5(12):e15915.

Müllner FE, Syed S, Selvin PR, Sigworth FJ. *Improved Hidden Markov Models for molecular motors, part 1: basic theory.* Biophysical Journal 2010 Dec 1; 99(11):3684-95.

Syed S, **Müllner FE**, Selvin PR, Sigworth FJ. *Improved Hidden Markov Models for molecular motors, part 2: extensions and application to experimental data.* Biophysical Journal 2010 Dec 1; 99(11):3696-703.

Eidesstattliche Erklärung

Ich versichere hiermit an Eides statt, dass die vorgelegte Dissertation von mir selbständig und ohne unerlaubte Hilfe angefertigt ist.

München, 15. Mai 2016 Fiona E. Müllner

Erklärung

Hiermit erkläre ich, dass die Dissertation nicht ganz oder in wesentlichen Teilen einer anderen Prüfungskommission vorgelegt worden ist und dass ich mich anderweitig einer Doktorprüfung ohne Erfolg nicht unterzogen habe.

München, 15. Mai 2016 Fiona E. Müllner